UCLouvain

epl

École polytechnique de Louvain

Modeling of fragments relocation during depressurization of a nuclear fuel rod

Author: **Guillaume Mévisse**
Supervisors: **Vincent Legat, Jonathan Lambrechts**
Readers: **Sandra Soares Frazao, Michel Henry**
Academic year 2023–2024
Master [120] in Mechanical Engineering

Abstract

A two-dimensional numerical simulation of fuel fragment relocation during a Loss of Coolant Accident (LOCA) was conducted. The Migflow software is utilized to model the problem as a granular flow, solved using CFD-DEM, providing a more accurate representation of the interactions between the fluid and the fragments. An algorithm is presented to generate an initial configuration of particles that matches experimental results, and some examples of this algorithm are provided. A new model that includes a numerical computation of the pressure in the cladding and an estimation of the fluid's compressibility is introduced. This model is compared to more traditional models and is used to demonstrate results based on parameters such as break size and pressure gradient. These findings suggest that using an accurate model in CFD-DEM simulation enables a more precise analysis of the relocation problem and opens up possible improvements such as considering compressibility effects or using a three-dimensional representation.

Acknowledgement

I would like to express my deepest appreciation to the entire Migflow team with whom I had the opportunity to work. I would like to thank Vincent Legat, Jonathan Lambrechts, Nathan Coppin, Simon Yans, and Michel Henry for their always caring help, advice, answers, and invaluable suggestions for this work.
I would also like to thank Frédéric Dubois from LMGC, Montpellier, and Adrien Nusslé from CEA IRESNE for their help in answering my questions and providing suggestions about fuel fragmentation and relocation.
Finally, I want to express my gratitude to my family and friends who supported me throughout this work, especially my parents for their feedback and help.

AI usage

In this master's thesis, AI tools were used to enhance the overall quality of the work. Specifically, Copilot was employed for code writing, Grammarly for grammar correction and improved phrasing, and ChatGPT for various purposes. Additionally, tools such as Scite.ai and Scispace were used for literature research.

Contents

List of Symbols[1]

Symbol	Definition	Units
Δt	Time-step	[s]
$\boldsymbol{n}$	Normal vector to the point of contact between two grains	[1]
$\boldsymbol{t}$	Tangential vector to the point of contact between two grains	[1]
d	Distance between the surfaces of two grains	[m]
R_n	Normal component of the reaction force in the local frame	[N]
R_t	Tangential component of the reaction force in the local frame in 2D	[N]
$\boldsymbol{w}$	Vector of the relative velocity between two grains	[m/s]
w_n	Normal component of the relative velocity between two grains	[m/s]
w_t	Tangential component of the relative velocity between two grains	[m/s]
$\boldsymbol{p}$	Vector of the impulse in the local frame	[N.s]
P_n	Normal component of the impulse in the local frame	[N.s]
P_t	Tangential component of the impulse in the local frame	[N.s]
M	Sum of the masses of the two grains in contact	[kg]
μ_k	Kinetic friction coefficient	[1]
μ_s	Static friction coefficient	[1]
μ_f	Dry friction coefficient	[1]
$\dot{\boldsymbol{q}}_i$	Vector of the velocities of the grain i in the global frame	[m/s],[rad/s]
u_i	Horizontal velocity of grain i	[m/s]
v_i	Vertical velocity of grain i	[m/s]
ω_i	Angular velocity of grain i	[rad/s]
$\boldsymbol{H}$	Mapping from the global frame to the local frame	[/]
$\boldsymbol{H}^T$	Mapping from the local frame to the global frame	[/]
$\boldsymbol{V}^T$	Vector of the velocities in the global frame if the two grains	[m/s],[rad/s]
N_x	Horizontal component of the normal vector $\boldsymbol{n}$	[1]
N_y	Vertical component of the normal vector $\boldsymbol{n}$	[1]
T_x	Horizontal component of the tangential vector $\boldsymbol{t}$	[1]
T_y	Vertical component of the tangential vector $\boldsymbol{t}$	[1]
r_i	Radius of grain i	[m]
m_i	Mass of grain i	[kg]
I_i	Inertia of the grain i	[kg . m^2]
$\boldsymbol{s}$	Impulse of the two grains in the global frame	[N.s]
$\boldsymbol{V}^+$	Velocity vector in the global frame after the iteration	[m/s],[rad/s]
$\boldsymbol{V}^-$	Velocity vector in the global frame before the iteration	[m/s],[rad/s]
ϵ	Porosity	[1]

[1]For a two-dimensional analysis, all extensive variables such as mass or force are divided by a length unit

Symbol	Definition	Units
ϕ	Compacity	[1]
ϕ_{real}	Compacity computed with the smallest surface enclosing the particles	[1]
V_f	Total volume of fluid	[m^3]
V_p	Total volume of particles	[m^3]
V_t	Total volume	[m^3]
$\boldsymbol{f_D}$	Total volumetric drag force on the fluid	[N/m^3]
$\boldsymbol{g}$	Vector of the gravity acceleration	[m/s^2]
$\boldsymbol{u}$	Vector of the fluid velocity	[m/s]
$\boldsymbol{u_s}$	Vector of the solid velocity	[m/s]
C_{D}	Drag coefficient	[1]
C_{D_0}	Drag coefficient without the Dallavalle correction	[1]
ρ	Fluid density	[kg/m^3]
Re_i	Reynolds number associated to grain i	[1]
μ	Dynamic viscosity of the fluid	[kg/(m.s)]
ν	Kinematic viscosity of the fluid	[m^2/s]
$\boldsymbol{F_e}$	Total force due to the fluid on the grain	[N]
$\boldsymbol{F_c}$	Total contact force on the grain	[N]
V_i	Volume of the grain i	[m^3]
ρ_p	Density of the particles	[kg/m^3]
p	Pressure	N/m^2
p_0	Initial boundary pressure	[N/m^2]
$\boldsymbol{f_{D}}_i$	Volumetric drag force on the grain i	[N/m^3]
λ	Polydispersity	[1]
r_{largest}	Radius of the largest grain	[m]
r_{smallest}	Radius of the smallest grain	[m]
A_p	Total surface of the particles	[m^2]
A_t	Total surface	[m^2]
h_{ref}	Reference height	[m]
w_{ref}	Reference width	[m]
x^*	Dimensionless horizontal coordinate	[1]
y^*	Dimensionless vertical coordinate	[1]
x	Horizontal coordinate	[m]
y	Vertical coordinate	[m]
r_{part_i}	Radius of the grain i that is already in the deposit	[m]
r	Radius of the grain to be inserted	[m]
d_i	Distance between the surface of the grain to be inserted and the grain i already in the deposit	[m]
y^*_{approx}	Approximation of the dimensionless vertical coordinate	[1]
r_{theo}	Theoretical radius at this height of the grain to be inserted	[m]
r_{max}	Maximum theoretical radius at this height of the grain	[m]
r_{min}	Minimum theoretical radius at this height of the grain	[m]
r_{bottom}	Radius at the bottom of the deposit	[m]
r_{center}	Radius at the center of the deposit	[m]
r_{top}	Radius at the top of the deposit	[m]
λ_{theo}	Theoretical polydispersity	[1]
r'	Radius of the inserted particle after the increased compacity	[m]
$N_{\text{particles}}$	Number of particles in the deposit	[1]

Symbol	Definition	Units
H	Height of the cladding	[m]
L	Width of the cladding	[m]
h	Size of the breach	[m]
e	Thickness of the cladding wall	[m]
l_c	Characteristic length of the mesh elements	[m]
Δt_{fluid}	Time-step for the fluid solver	[s]
$\Delta t_{\text{particles}}$	Time-step for the particles contacts solver	[s]
t_{end}	Simulation end time	[s]
N_{nodes}	Number of nodes in the mesh	[1]
N_{elements}	Number of elements in the mesh	[1]
$\boldsymbol{x}$	Position vector	[m]
S	Surface used for averaging quantities	[m^2]
$\overline{\phi}$	Time averaging of ϕ	[1]
τ	Time constant for the exponential decay	[s]
s	Source term	[/s]
$\boldsymbol{f}$	Volumetric force on the fluid	[N/m^3]
R^*	Specific gas constant of the fluid	[J/(kg K)]
T	Temperature of the fluid	[K],[°C]
$\overline{u_x}$	Averaged horizontal fluid velocity in the break	[m/s]
R_c	Cohesion force between two grains	[N]
α	Cohesion coefficient	[N]
$\boldsymbol{p}_i^*$	Impulse in the local frame of grain i taking into account the cohesion	[N.s]
$\boldsymbol{p}_{\boldsymbol{c}i}$	Impulse in the local frame of grain i due to the cohesion force	[N.s]
g	Magnitude of the gravity acceleration	[m/s^2]
A	Multiplying constant for the cohesion coefficient	[1]

List of Figures

Introduction

Nuclear power plays a significant role in generating electricity in Western Europe, especially in Belgium and France. In 2022, 45% of Belgium's electricity was generated from nuclear power plants (FEBEG 2023). Nuclear energy is considered clean, reliable, and controllable, making it an important component of the future energy mix, which should be as carbon-free as possible. However, nuclear reactors carry inherent radiological risks, necessitating a thorough study of their behavior in the event of an accident.

Most nuclear reactors are Pressurized Water Reactor (PWR) (as a fact, all Belgian nuclear reactors are PWR). The reactor comprises 3 cooling circuits: the primary circuit contains highly pressurized liquid water (around 150 bar) heated by the fission of fissile atoms (mainly uranium dioxide). This water exchanges heat with the secondary circuit water, evaporating it. It drives a turbine and is then cooled by cold water from the tertiary circuit (El-Sefy et al. 2019).

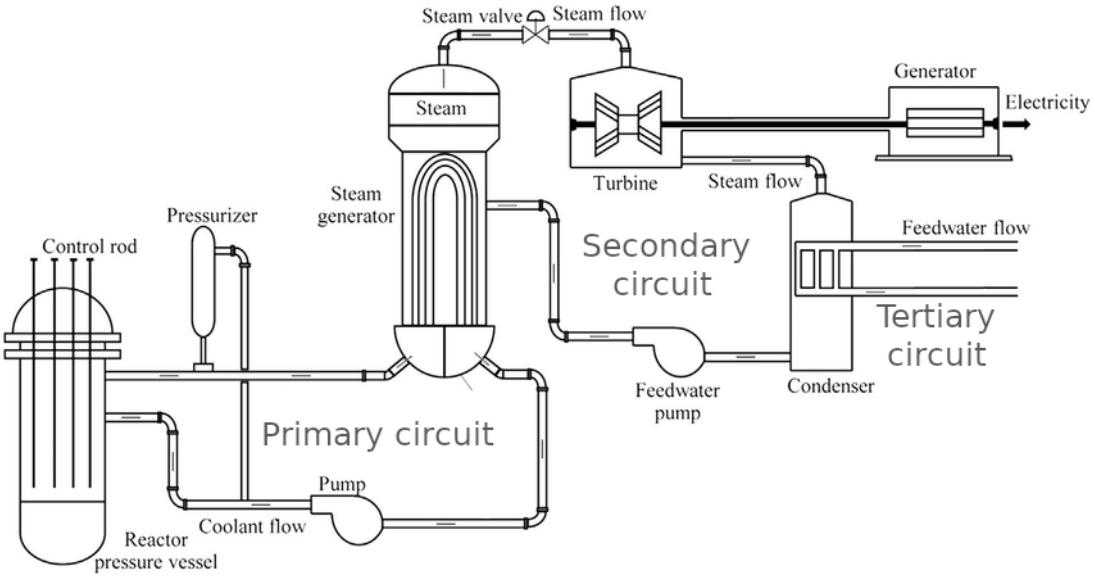

Figure 1: Schematic of a Pressurized Water Reactor

The nuclear fuel consists of 8 mm diameter and 13 mm height uranium pellets, placed in a tubular cladding of 9.5 mm outside diameter and 4 m height that confines the radioactive materials (D'Auria 2017). This is called a rod; the nuclear core generally contains 100 to 200. The pellets are pressurized at about 70 to 80 bar to prevent cladding rupture due to pressure difference. The irradiation of the rod causes the production of gaseous fission products, which affect the behavior of the materials. This effect is amplified as the temperature of the fuel increases, making the assembly more fragile.

A well-known and common accident in PWRs is a Loss Of Coolant Accident (LOCA). An example of this is the incident at Three Mile Island in 1979 (COLLIER & DAVIES

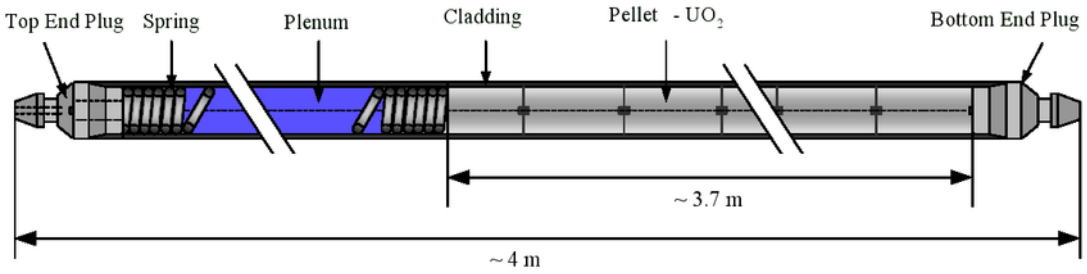

Figure 2: Schematic of a single fuel rod (Blair 2008).

1980). This occurs when an external event, such as a pipe rupture or pump failure, causes the water from the primary circuit to stop circulating in the reactor core. As a result, there is a drop in pressure outside the fuel rods and a rise in temperature in the cladding, leading to high thermomechanical stresses (Trégourès 2013).

Recent experiments have shown that there is a risk of local nuclear fuel fragmentation, where a pellet of uranium can break into very small particles (measuring just a few micrometers) during a thermal transient situation such as LOCA (Loss of Coolant Accident) (Capps et al. 2020). Additionally, thermomechanical stresses can cause the cladding to rupture, resulting in a small breach (on the order of a millimeter). If the cladding experiences a large enough breach and the fuel is finely fragmented, it could lead to fuel leakage. This fuel leakage could result in the ejection of radioactive material, posing direct and indirect safety concerns. Therefore, it is important to study the conditions that lead to this type of leakage and the subsequent relocation of radioactive particles.

This master's thesis will focus on the movement of particles after the fuel has been fragmented and the breach has been formed. There is limited experimental data on the movement of these particles, so the approach will be mostly phenomenological. The research will involve developing a simulation of how fuel particles relocate after fragmentation, taking into account various parameters such as pressure gradient, particle size, and inter-particle friction, and estimating the impact of these parameters.

The movement of particles in a fluid is referred to as an immersed granular flow. This thesis is a part of Migflow (Constant et al. 2018), a project aimed at modeling immersed granular flows. The Migflow project is free and open-source, and it is the result of collaboration between Université Catholique de Louvain and Université de Montpellier. Later on, this project and the methods utilized will be presented. The objectives of this work are to propose a model for the relocation problem and then to utilize this model to demonstrate the qualitative effects of various parameters such as the break size or the pressure.

First, a literature review on fuel relocation during LOCA is conducted. This includes presenting existing models and data for fuel pellet fragmentation and relocation, as well as the equations and methods for solving immersed granular flows, particularly those used in Migflow. Finally, the simulation objectives are clearly detailed.

The second section focuses on the new algorithm used to generate the initial particle deposit. By incorporating a score function and a compactness criterion into existing algorithms, it becomes possible to create a new algorithm that allows control over the spatial distribution of particle sizes while maintaining a stable and compact deposit. The section also presents some results obtained from the algorithm.

Thirdly, the physical, geometrical and numerical parameters of the simulation are presented. The modeling of the problem is discussed, and multiple models are proposed and compared, each including an approximation of the pressure. The impact of friction on the flow is studied.

Finally, a study is conducted to show the influence of various parameters such as the fluid properties or the size of the break. A proposal is made to model the cohesion between the fragments, and the model is used to increase the interaction between the particles and with the cladding. This cohesion is the source of new phenomena that are expected in this situation and can also be used as a way to numerically increase the interaction between the grains to better represent the flow.

Chapter 1

A first glance at the problem

This chapter provides a comprehensive overview of the current knowledge on fuel fragmentation and relocation during a loss-of-coolant accident. In recent years, there has been a significant increase in both experimental and simulation studies on this phenomenon, with tests conducted in specialized facilities and the development of advanced simulation models for both fragmentation and particle displacement. Following the rupture of the cladding, the gas pressure difference forcefully drives a flow of gas and particles outside of the cladding into the cooling circuit. This displacement of particles in a fluid is specifically termed an immersed granular flow. The methods and models utilized in this work are meticulously detailed. The chapter concludes by clearly defining the objectives of the simulation.

1.1 Fuel pellet fragmentation

During a LOCA, the particular conditions in the cladding lead to high thermomechanical stresses. Despite the neutron reactions being stopped by the deployment of control rods, there is still residual power. The temperature of the fuel rod consequently rises, increasing the rod's internal pressure and reducing the mechanical properties of the cladding. Combined with the high-pressure differential, this can lead to plastic deformation of the cladding, known as ballooning. This deformation can rupture and become a breach in the cladding, leading to depressurization of the rod.

The thermal and mechanical stresses experienced can result in the fragmentation of nuclear fuel, as documented in (M. Flanagan 2012) and (Capps et al. 2020). These fragments are typically in the micrometer range, whereas regular pellet fragmentation due to irradiation occurs in the millimeter range. When the rod depressurizes, these particles are released into the primary circuit. Although the exact impact of these particles on the primary circuit's operation is not yet fully understood, it is evident that the presence of radioactive particles within it poses a safety concern. Additionally, understanding the properties of this particle bed, including its coolability (Lindholm 2002), fuel-coolant interaction (Raynaud 2012), and other factors, is crucial.

As fragmentation not being the phenomenon studied here, only a few details will be presented. Several experimental tests were carried out, such as the EDGAR tests (Forgeron et al. 2000), a program at the Halden experimental reactor (Wiesenack et al. 2016), the SCIP program (Karlsson et al. 2017) and tests at CEA's facilities (Hanus et al. 2016). The ballooning and rupture phenomena were observed during these tests, and the parameters on which fragmentation depends were determined, such as fuel temperature, fuel burn-up, etc. (Bianco et al. 2015). SCIP program's results estimate the size of the rupture, ranging from 1 to 20 mm. The mass distribution of fragments is still unclear, as results seem

to follow different trends (1.1). It was shown that the fragmentation could be reduced by imposing hydrostatic pressure (J. A. Turnbull & Walker 2015). A model was built from these results to estimate the rupture area and dimensions of the cladding(Capps & Sweet 2023). Finally, Kim et al. (2021) developed a multiphysics fuel analysis and thermal-hydraulics code to analyze the fuel rod's anisotropic behavior during LOCA, predicting the ballooning and strain of the cladding.

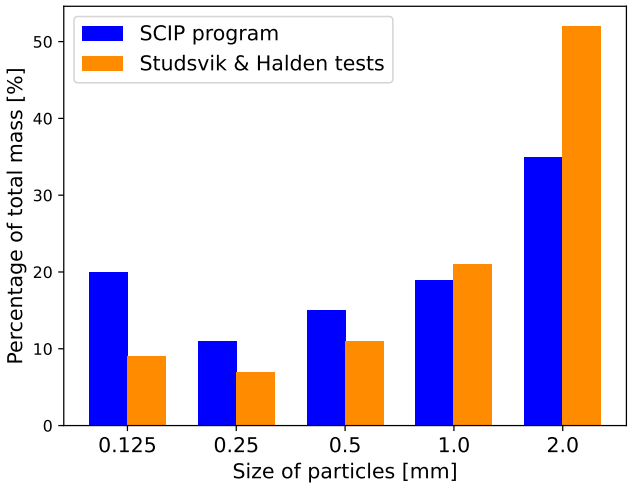

Figure 1.1: Size distribution in different tests.
Blue data comes from (Karlsson et al. 2017) and orange data comes from (Capps et al. 2020). The SCIP data shows a size distribution quite uniform for the particles smaller than 2mm while the Halden and Studsvik tests show a more increasing mass distribution with the size of the particles.

1.2 Fuel fragments relocation

Most of the previously cited studies on fuel relocation focus on relocation in the cladding, i.e. starting with intact pellets and ultimately looking at their position in the balloon. They, therefore, give a correct definition of the initial situation at the time of cracking, but practically nothing about what happens afterward. Some works also distinguish between relocation (within the cladding) and dispersal (outside the cladding).

First, the experimental programs only considered a single rod, neglecting the influence of neighboring rods. A few parameters have an obvious influence: the dispersal is impossible if the fissure size is smaller than the smallest fragments, while a fissure larger than all fragments leads to a full dispersal of them. In some cases, the fuel dispersal could cause a blockage in the coolant channel (Brankov 2017).

Govers and Verwerft used a discrete element method to study the dispersal of spherical fragments with constant radii(Govers & Verwerft 2016). This three-dimensional simulation showed the suitability of granular materials simulation for relocation and dispersal applications. Especially, it presented a compacity of 0.5 to 0.6 in the balloon, similar to experimental results(NEA 2010). However, the process is highly stochastic due to the fragmentation of the particles, the shape influencing local pressure losses, and the shape of the fragments and the break may or may not allow fragments to pass through. Furthermore, the position of the crack along the height of the rod has a strong influence as it determines the amount of gas and particles that are close to the crack and their position. For example, a crack near the bottom may result in slower gas outflow than a crack near the top(Khvostov et al. 2011).

A first estimation for the total mass dispersed was presented in (Raynaud & Porter 2014) using TRACE and FRAPCON, two reactor systems codes used to simulate reactor thermal-hydraulics behavior. These codes are however not built to simulate the local effects of the particles as they use a coarse approach. These results were presented as not generalizable and very approximate. In (Brankov 2017), a model is presented to simulate the fuel dispersal. The geometry is separated into three regions: the plenum full of gas, the fuel stack, and the cracked balloon. The fuel stack is composed of movable and immovable particles, which depend on the size of the particles. The interaction between fluid and gas is modeled with correlations, and the conservation equations are written for the fuel and the gas in each of the three volumes. Therefore, it only computes the values in each of them and does not simulate each particle and the fluid flow separately. This model was run for the multiple tests done at Halden's experimental reactor and for the SCIP program: most results were consistent, while not being able to describe precisely all phenomena. For example, the pressure in the fuel stack and plenum was shown to follow an exponential decay (see Figure 1.2) in the simulation, just as in the case of a gas leak from a tank. In the measurements, the decay was close to exponential but variations were observable, due to the particle's interactions with gas around the crack which are not modelized in this approach (Capps et al. 2021).

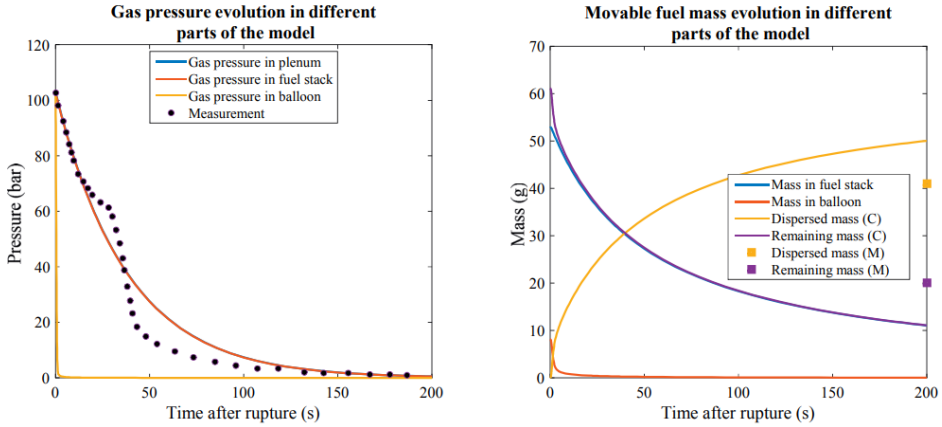

Figure 1.2: Gas pressure and mass evolution for a test case in the model of (Brankov 2017)

A final simulation was done to a full-length rod, shown in Figure 1.3. However, this simulation assumed a constant size of fuel fragment of 1mm.

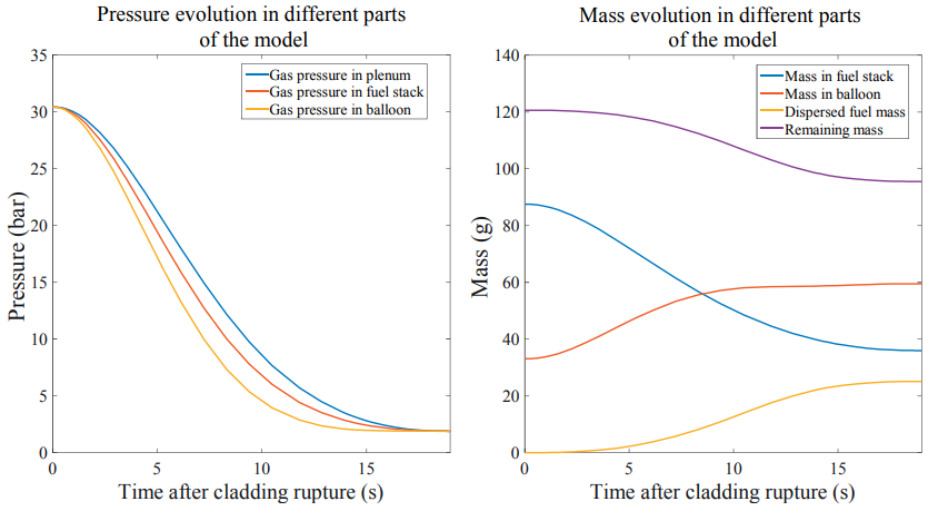

Figure 1.3: Gas pressure and mass evolution for a full rod (Brankov 2017).

1.3 Fuel fragments relocation as a granular flow problem

The conclusion to be drawn from the above developments is that it is necessary to use models more suited to describing this type of flow, where local interactions between fluid and solids are important. These flows are known as granular flows. A granular flow is defined as a collection of solid discrete bodies surrounded by a fluid. The interaction of the fluid and the grains leads to their movement. Typical granular flows include cement in civil engineering, avalanches, lava, etc. While current research on this subject is quite extensive and applies to many fields including pharmaceuticals, geology, and the environment, the use of these flows in nuclear engineering is relatively new and still developing. Solid particles are commonly used and simulated in various applications in nuclear engineering, such as Pebble Bed Reactors (PBRs) (Rycroft et al. 2006), analyzing the burn-up of fuel pebbles, and studying the formation of debris beds in severe accidents. Recently, numerical modeling has become an effective tool for investigating these systems.

In nuclear engineering, the flows are generally classified into two categories: the first corresponds to single-phase granular systems, in which the influence of the fluid on the particles is negligible, and the particles-particles and particle-wall interactions dominate. The second type comprises applications where the solid-fluid interactions are not negligible. Following the description in 1.2, the fuel relocation and dispersal fall in this category (Rui Li & Sakai 2024).

Discrete Element Method (DEM) has been proposed and validated to simulate the behavior of the particles. In this method, the particle's motion is computed based on Newton's second law of motion, while the contact forces are computed using a model such as the Voigt model. Only spherical 2D particles are considered in this work, but DEM is also applicable to non-spherical or 3D particles (Zhong et al. 2016).

To solve the contacts, Non-Smooth Contact Dynamics (NSCD) is used (Jean 1999). The grains are considered as non-overlapping solid spheres (or disks in two dimensions), unable to deform. It is an iterative method: at each time step Δt, all possible contacts are detected. A contact between two particles is possible if they are closer than some alert distance, this distance being the radius of the largest grain. An iterative process is then used: the contacts are detected and solved and the velocities are updated. Then, the contacts are detected again and solved, until the velocities have converged. Each contact is resolved in a local reference frame defined with the normal and tangential vectors noted $\boldsymbol{n}$ and $\boldsymbol{t}$. The hypothesis of non-interpenetrating grains is expressed as follows: the gap between the two particles d is larger than or equal to zero at any time t. The reaction force between two particles R_n is zero if the two particles are not contacting. This gives the Signorini condition :

$$d(t) \geq 0, R_n(t) \geq 0, R_n(t)d(t) = 0$$

If $\boldsymbol{w}^T = \begin{bmatrix} w_n & w_t \end{bmatrix}$ is the relative velocity vector in the local frame, then it is rewritten as :

$$d > 0 \Longrightarrow R_n = 0$$

$$d = 0 \Longrightarrow w_n \leq 0$$

$$w_n \leq 0 \Longrightarrow R_n = 0$$

These three lines state that if the gap between particles is non-null, the reaction force is null. If the gap is null, then the relative can't be larger than zero. If it is equal to zero, then the contact is persistent, and if it is less than zero, then the contact is vanishing. Finally, if the contact is vanishing or persistent, then the reaction force is null.

However, this condition alone only gives the reaction to satisfy the Signorini condition. An impulse $\boldsymbol{p}^T = \begin{bmatrix} P_n & P_t \end{bmatrix}$ in the local frame has to be calculated, from which the velocity is deduced using M the sum of grain masses (Moreau 1994) (Radjai & Richefeu 2009) :

$$P_n = M(w_n - \frac{d}{\Delta t})$$

Physically, this means that the velocity is corrected by an amount such that the grains do not interpenetrate at the next time-step. However, their relative velocity is still larger than zero. The contact law is activated again at the next iteration, and the relative velocity is canceled out. Therefore, it is a perfectly inelastic law, that could be discussed. In reality, the collisions are partially elastic, and part of the energy is dissipated in heat and deformations. However, this dissipation is not modeled, and an elastic law of contacts would lead to indefinitely vibrating particles. The inelastic model then allows for a better representation of the physics. For the contacts with the wall, similar equations are used considering a wall that is fixed.

Friction is taken into account when calculating tangential velocity, using Coulomb's friction law. R_t being the tangential reaction force, it gives :

$$w_t > 0 \Longrightarrow R_t = -\mu_k R_n$$
$$w_t = 0 \Longrightarrow R_t = \mu_k R_n$$
$$w_t < 0 \Longrightarrow R_t \leq \mu_s R_n$$

With μ_s the static friction coefficient and μ_k the kinetic friction coefficient. However, in granular flow, the friction coefficient usually used is the dry friction coefficient μ_f, which is around 0.3 to 0.6 for most granular media and close to the static friction coefficient. Works have studied the variation of μ_f in granular media, showing the effect it has on the rheology of the flow (Man et al. 2022). The friction is therefore computed as :

$$R_t = -\mu_f R_n$$

The tangential impulse P_t has to be determined so that the tangential velocity w_t is canceled. However, here, the impulse cannot reach an arbitrarily large value, as it is limited by the friction coefficient. The maximum tangential impulse is given by the coefficient of dry friction μ_f times the normal impulse P_n. If this value is smaller than the tangential impulse needed to cancel the tangential velocity, then the grains slide on each other. This is stated as :

$$0 = w_t + \frac{P_t}{M}$$
$$P_t \leq \mu_f P_n$$

As friction law changes the tangential velocity, it will change the linear velocity of the grains, but also their angular velocities. For the friction with the wall, the same thought process can be held, considering that the wall does not move.

The values for the friction coefficients have to be fixed. For the friction between the UO2 particles and the wall made in zirconium alloy, studies show that the static friction coefficient is dependent on temperature and irradiation, and globally increases with temperature and time under irradiation, with values going from 0.3 to 1.5 in most cases, but reaching up to 3 for long irradiation periods (Bozhko et al. 1991) (Shchavelin et al. 1986). However, these are the static friction coefficients, and they were computed with highly pressurized particles under long-time contacts, leading to high frictional forces. The effect of this coefficient will therefore be studied later.

In the global reference frame, the vector $\dot{\boldsymbol{q}}_i^T = \begin{bmatrix} u_i & v_i & \omega_i \end{bmatrix}$ describes the velocities of the grain i. The global frame velocities are then converted to the local frame using the mapping $\boldsymbol{H}$. The inverse mapping $\boldsymbol{H}^T$ is the mapping that converts the local frame velocities to the global frame. Using $\boldsymbol{V}^T = \begin{bmatrix} \dot{\boldsymbol{q}}_i^T & \dot{\boldsymbol{q}}_j^T \end{bmatrix}$ the vector of the velocities in the global frame of the two grains in contact, the relation is :

$$\boldsymbol{w} = \boldsymbol{H} \cdot \boldsymbol{V}$$

$$\boldsymbol{w} = \begin{bmatrix} N_x & N_y & 0 & N_x & -N_y & 0 \\ T_x & T_y & r_i & T_y & -T_y & r_j \end{bmatrix} \cdot \boldsymbol{V}$$

Where N_x, N_y, T_x and T_y are the x and y components of the normal and tangent vectors, and r_i, r_j the radii of the grains. It is illustrated in figure 1.4.

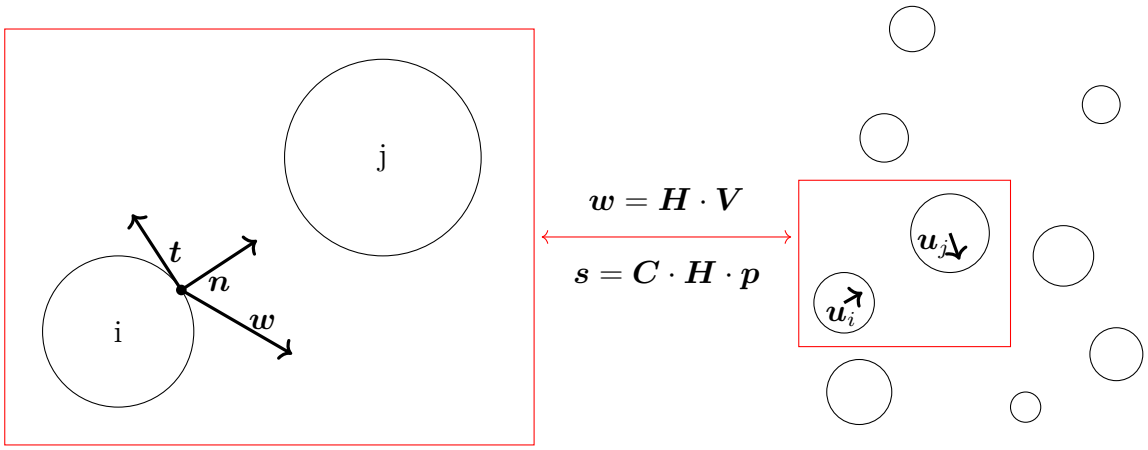

Figure 1.4: Local and global frames for the resolution of the contacts in NSCD.

Finally, the impulse in the global frame $\boldsymbol{s}^T = \begin{bmatrix} \boldsymbol{p}_i^T & \boldsymbol{p}_j^T \end{bmatrix}$ is computed, where $\boldsymbol{p}_i$ is the impulse on the grain i and I_i its inertia:

$$\boldsymbol{s} = \boldsymbol{C} \cdot \boldsymbol{H} \cdot \boldsymbol{p}$$

$$\boldsymbol{C} = \begin{bmatrix} \frac{m_j}{M} & & & & & \\ & \frac{m_i}{M} & & & & \\ & & \frac{m_i}{I_i} & \frac{-m_j}{M} & & \\ & & & \frac{m_i}{M} & & \\ & & & & \frac{m_i}{M} & \\ & & & & & \frac{m_j}{I_j} \frac{-m_i}{M} \end{bmatrix}$$

This gives the new velocity in the global frame, with $\boldsymbol{V}^+$ and $\boldsymbol{V}^-$ indicating the velocities before and after the iteration and $\boldsymbol{M}$ the mass matrix of the two grains :

$$\boldsymbol{M}(\boldsymbol{V}^+ - \boldsymbol{V}^-) = \boldsymbol{s}$$

The DEM is then coupled to Computational Fluid Dynamics (CFD) for the simulation of the grain-fluid flow. Here, two methods exist resolved or unresolved methods. In resolved methods, the solid-fluid interaction is directly modeled from the original governing equations. The spatial resolution of the CFD must therefore be sufficiently smaller than the size of the particles. It leads to high accuracy but a high computational cost. In unresolved methods, the solid-fluid interaction is modeled via theoretical or empirical correlations. The spatial resolution of the CFD can therefore be lower, leading to less precise but faster simulations. In Migflow, a semi-resolute approach is currently used. The

mesh size is close to the grain size, and the drag force on particles is represented by an empirical correlation. It has the advantage of keeping a precise enough resolution with a fast algorithm.

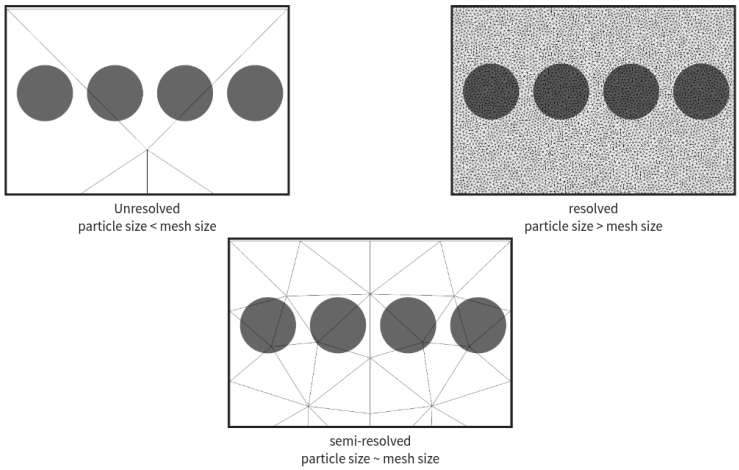

Figure 1.5: Illustration of solved, unsolved and semi-solved methods. The solved methods use a finer mesh, and the unsolved method uses global correlation to compute the interactions between the grains and the fluid.

The CFD-DEM is resolved using volume-averaged Navier-Stokes equations corrected for granular media and incompressible flows. Two new variables are defined: the porosity which is the ratio between the fluid volume to total volume $\epsilon = \frac{V_f}{V_t}$, and the compacity which is the ratio between the particle volume to total volume $\phi = \frac{V_p}{V_t}$ as shown in Figure 1.6.

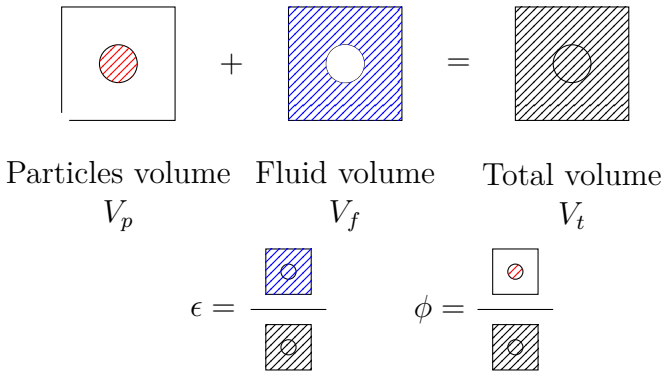

Figure 1.6: Illustration of the porosity and compacity

Using the drag force on the particles $\boldsymbol{f_D}$, the gravity vector $\boldsymbol{g}$, the fluid velocity $\boldsymbol{u}$ and the solid velocity $\boldsymbol{u_s}$, the equations read :

$$\boldsymbol{\nabla} \cdot (\phi \boldsymbol{u_s}) + \boldsymbol{\nabla} \cdot (\epsilon \boldsymbol{u}) = 0$$

$$\epsilon \rho \frac{\mathrm{D}\boldsymbol{u}}{\mathrm{d}t} = -\epsilon \boldsymbol{\nabla} p + \boldsymbol{\nabla} \cdot [2\epsilon\mu \boldsymbol{d}(\boldsymbol{u})] + \rho\epsilon \boldsymbol{g} + \boldsymbol{f_D}$$

The drag force is characterized by the drag coefficient, computed using the voidage function associated with the Dallavalle correlation (Qi et al. 2022):

$$\boldsymbol{f_D} = \mathrm{C}_D \pi r_i^2 \frac{\rho}{2} ||\boldsymbol{v}_i - \boldsymbol{u}||(\boldsymbol{v}_i - \boldsymbol{u})$$

$$\mathrm{C}_D = g(\epsilon)\mathrm{C}_{D,0}(\epsilon\mathrm{Re})$$
$$\mathrm{C}_{D,0} = \left(0.63 + \frac{4.8}{(\epsilon\mathrm{Re}_i)^{0.5}}\right)^2$$
$$g(\epsilon) = \epsilon^{-1.8}$$

with the grain Reynolds number

$$\mathrm{Re}_i = \frac{2r_i\rho}{\mu}||\boldsymbol{v}_i - \boldsymbol{u}||$$

Finally, the particles are tracked using DEM, with the contacts resolved using NSCD which gives for the grain i :

$$m_i\frac{\mathrm{d}\boldsymbol{v}_i}{\mathrm{d}t} = \boldsymbol{F}_e + \boldsymbol{F}_c$$
$$\boldsymbol{F}_e = V_i\left(\rho_p\boldsymbol{g} - \boldsymbol{\nabla}p - \boldsymbol{f_{D}}_i\right)$$

Compared to the original problem, the simulation built here has multiple shortcomings: the particles are only spherical, when in fact the fragments have complex shapes. The simulation is in two dimensions, which prevents three-dimensional effects from being represented and reduces the cylindrical cladding to a rectangle. Finally, the thermal effects and compressibility of helium are not represented, while it plays a significant part in the depressurization of the rod.

1.4 Objectives of the simulation

This thesis has multiple objectives. Firstly, it aims to create a two-dimensional model for particle relocation that produces results consistent with the limited experimental data available. This model will introduce new features, such as the spatial distribution of particle size. It will be used to estimate the impact of various phenomena on the relocation of fuel particles, using precise criteria such as expelled mass, ejection time, and more. Finally, this work will also contribute to the research of Adrien Nusslé from CEA IRESNE, who is studying this relocation phenomenon in detail.

Chapter 2

Initial fragments generation

This chapter describes the algorithm used to generate the initial deposit of circular particles. In most simulations in immersed granular flows, constant radii are used for the particles, or slightly varying radii. This is called polydispersity, and it is defined as the ratio between the radii of the largest to the smallest particles :

$$\lambda = r_{\text{largest}}/r_{\text{smallest}}$$

Depending on simulations, this value can go from 1 (uniform radii or mono-disperse particles) to 20 or even more (Polanía et al. 2022). Another parameter that defines the stack is the packing fraction, the ratio between the particle total surface A_p (for a two-dimensional problem) to the total surface of the domain A_t :

$$\phi = A_p/A_t$$

For the algorithm analysis, the variable ϕ_{real} is defined. It is the packing fraction but only considering the smallest volume enclosing the grains (further information in section 2.3). For mono-disperse particles, the reference values are $\phi = 0.55$ for random loose packing and $\phi = 0.64$ for random close packing in three dimensions (Scott 1960), even though denser packing can be generated. An increase in polydispersity leads to an increase in packing fraction, as the fine particles fill the gaps between the coarse ones.

The particles in this problem are not mono-disperse, as it would be impossible for the whole fuel pellet to break up into multiple particles of the same size. Furthermore, the size of the particles depends on their position in the pellet. Conventional deposit generation algorithms deal with polydispersity but are unable to manage the coupling between particle position and radius. These algorithms first need the particle's radius before determining its position. Therefore some modifications are presented to manage the spatial distribution of particles.

The generation area is a simple rectangular box, with height equal to h_{ref} and width w_{ref}. The origin of the reference frame is in the center of the rectangle. To simplify the equations, the variables are defined using the dimensionless domain centered:

$$x^* = 2\frac{x}{w_{\text{ref}}}$$

$$y^* = 2\frac{y}{h_{\text{ref}}}$$

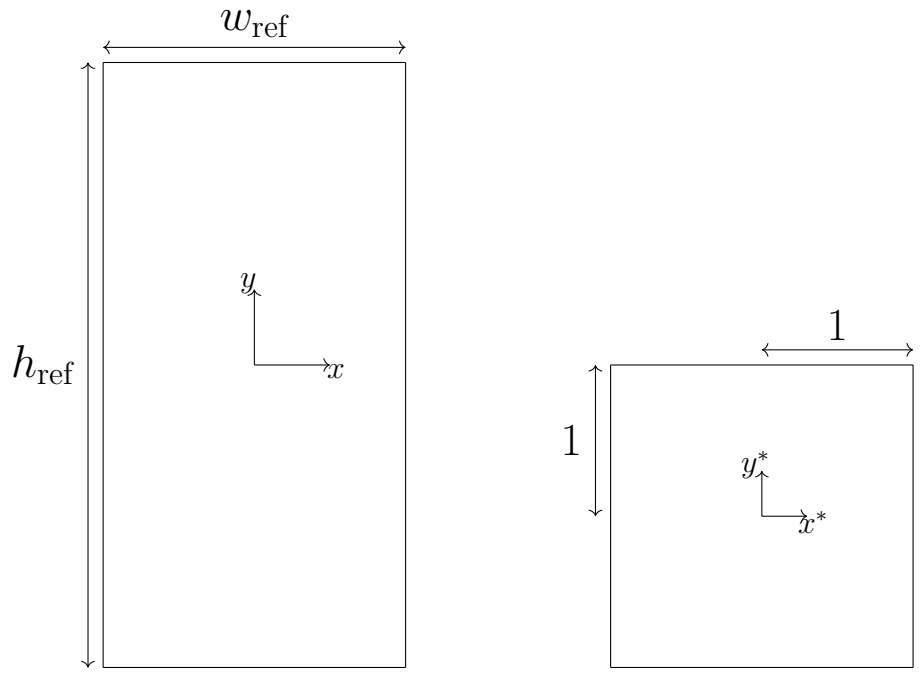

(a) Physical domain (b) Dimensionless domain

Figure 2.1: Particle generation domain

2.1 An overview of existing algorithms

The generation of such a deposit can be thought of in two ways: one purely relying on contact dynamics, and the other purely on a geometrical approach. In both cases, it is an incremental process, where a particle is added to an already-generated deposit. Here is only considered a deposit in a rectangular box, but both algorithms can be generalized for any shape.

The generation using contact dynamics is similar to what happens in a real experiment, where grains would be poured into a box. The grain is generated with a radius r and then is dropped at some point x along the width of the box. It will touch the first particle below it, and then roll towards the steepest gradient, reaching a stable point when its center of mass lies between the supporting contacts. It mimics the movement of a particle that would be randomly dropped on top of a granular bed. The main drawback of this method is its high computational cost, as the simulation of the fall of each particle is needed. It is illustrated in figure 2.2.

A faster way to solve this problem is a geometric approach with an optimization problem, which is called the potential-based method. If the radius of the i-th particles already inserted is noted r_{part_i}, then the objective is to minimize the height which is the function $f(y^*) = y^*$ of the particle of radius r inserted, such that the gap d_i between the two grains is larger or equal to zero (no interpenetration). This is written in Figure 2.3 in the case where there are n grains already inserted.

A solution to the problem is found efficiently: at first, the minimization of f requires that the new grain lies on an existing particle, such that $d_i = 0$ for at least one already existing particle. An active front that contains the particles at the top of the granular bed is therefore constructed. Some grains can be ignored as they are below other ones, and the new grain to be added can't touch them without interpenetration. From this active front of particles, a line Ψ is drawn at a distance r of all particles (and walls of the box).

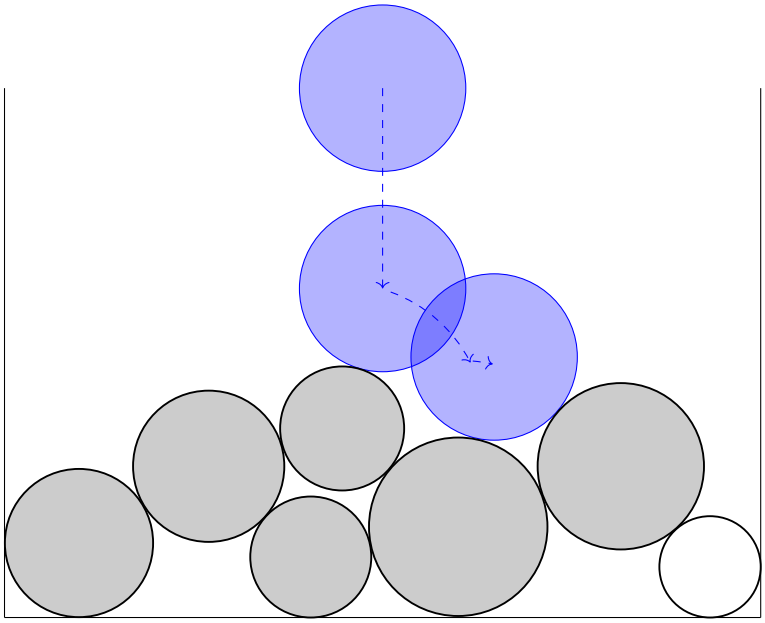

Figure 2.2: Illustration of random deposit method.
The particle falls from a random point until it reaches a stable state.

This line is only the union of every circle of radius $r + r_{\text{part}_i}$ around each particle of the front. It contains all possible points to place the new particle with the condition that g_i is zero for at least one particle. Furthermore, all possible stable points are local minimums, which are the intersections of two circular arcs with the condition that the slope of the line is negative on the left and positive on the right, as elsewhere the new particle would roll (it is not a sufficient condition). The new particle is placed at the lowest point of this line as it minimizes f, which means that the point found is necessarily a local minimum.

$$\begin{aligned} &\text{minimize} \quad f(x^*, y^*) = y^* \\ &\text{subject to} \quad \Big\{ d_i(x^*, y^*, r) \geq 0, \quad i = 1, \ldots, n \end{aligned}$$

Figure 2.3: Optimization problem to solve with the potential-based algorithm.

The local stability of a particle doesn't assure the global stability of the deposit, especially for deposits with high polydispersity. However, making it stable is possible by simulating it under gravity, particles will rearrange themselves to reach stability. This method generates deposits that are more compact than with the contact dynamics method, as it places the particle at the absolutely lowest point, while the random method places it at the locally lowest point. This generation algorithm was studied further in (Taboada et al. 2005) and (Voivret et al. 2007), and is illustrated in figure 2.4.

2.2 Suboptimal criterion for polydisperse deposit

In the case of nuclear fuel relocation, the size of the particles depends on their position (Bonnet 2021). This is because the thermomechanical stresses are concentrated around the breach, leading to a finer fragmentation in this region. This new algorithm for particle generation has to be able to take into account the spatial distribution of particles, which is not possible with the algorithms described above.

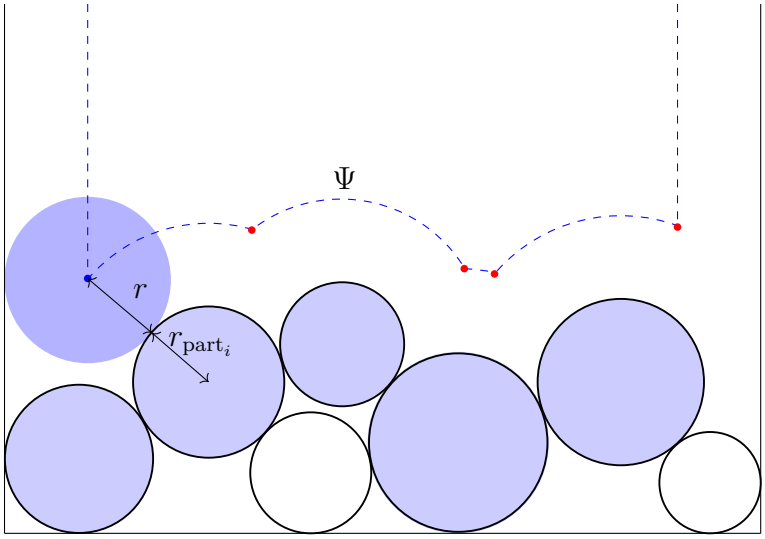

Figure 2.4: Illustration of potential-based deposit method.
Red points are all possible points and the blue point is the lowest one.
Blue particles are the active front and white particles are the ignored ones.

The original algorithm used is the potential-based method, as it is faster and the modifications are easier to implement. For the spatial distribution, it is needed to define the radius r of the particle as a function of the height, which is unknown as the optimization problem is still not resolved. An estimation of the height is therefore done: a line Ψ' is drawn, similar to the one in the original algorithm, but with a radius $r = 0$. Then the lowest point of this line is taken as an estimation y^*_{approx} of the height where the particle is inserted (see Figure 2.5).

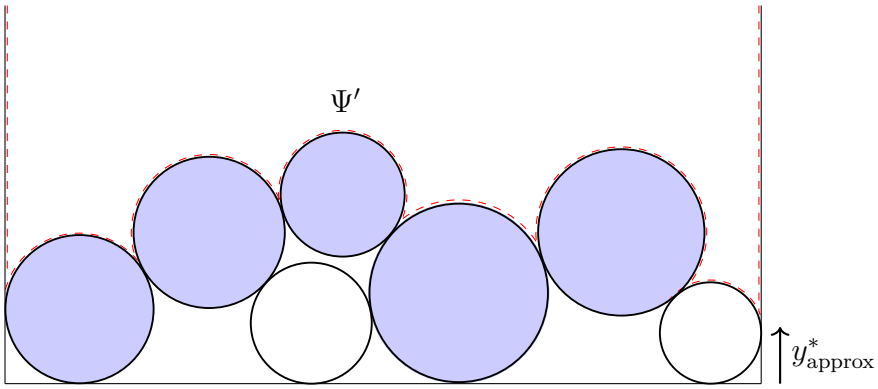

Figure 2.5: Height estimation using the lowest point of the Ψ' line.

From this height, a radius r_{theo} is computed for the particle. For example, the radius can increase linearly with the height :

$$r_{\text{theo}}(y^*_{\text{approx}}) = Ay^*_{\text{approx}} + B \text{ [mm]}$$

From this computed radius, the problem is solved with the initial algorithm using the front and the line Ψ. The optimization problem is rewritten in Figure 2.6.

The parameters A and B can be adjusted to reach the desired distribution. From the definition of y^*, the value of B is the radius at the center. For this example, it is fixed at 0.25 [mm], so $B = 0.25$ [mm]. Then, the value of A depends on the radius on top or at the bottom of the box. Considering that the radius at the bottom $r_{\text{bottom}} = 0.1$ [mm] :

$$A(-1) + B = r_{\text{bottom}}$$

$$\begin{aligned} &\text{minimize} \quad f(x^*, y^*) = y^* \\ &\text{subject to} \quad \begin{cases} d_i(x^*, y^*, r) \geq 0, & i = 1, \ldots, n \\ r = r_{\text{theo}}(y^*_{\text{approx}}) \end{cases} \end{aligned}$$

Figure 2.6: Optimization problem with a radius depending on the height of the grain.

$$A = B - r_{\text{bottom}}$$

This gives $A = 0.15$ [mm]. A first deposit is generated using this height distribution of the radii, containing 1333 particles, and shown in Figure 2.7. The generated radii perfectly fit the function defined. It has a polydispersity of 3.94, close to the theoretical $r_{\text{top}}/r_{\text{bottom}} = 4$, and a packing fraction of 0.79.

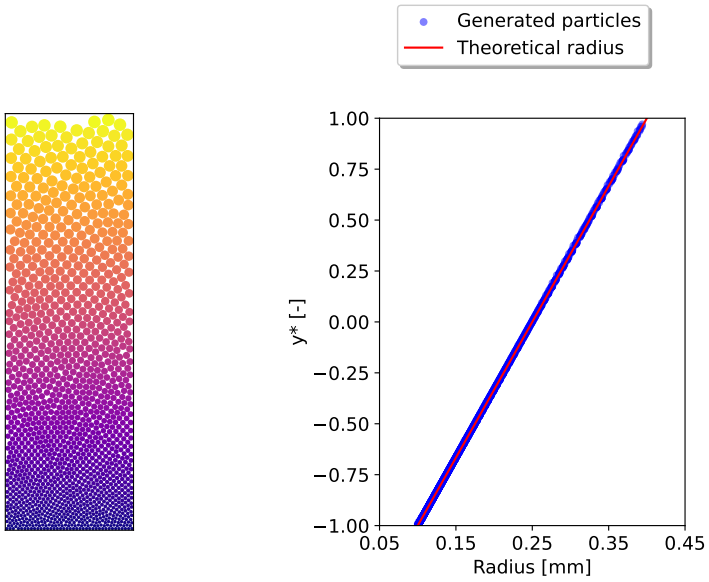

Figure 2.7: Particle generation with a linear law of radii.
The generated particles perfectly follow the distribution defined.

Next, local polydispersity is added to the particles. A maximum and minimum radius are defined as functions of r_{theo}: $r_{\max}$ and $r_{\min}$. A random radius r is computed from these two values. There are multiple parameters to choose: the functions for $r_{\max}$ and $r_{\min}$, and the probability distribution $\mathrm{P}(r_{\min}, r_{\max})$ that is used to compute r from these values. Again, the optimization problem is written in Figure 2.8. There are no limitations, but for the sake of simplicity, mostly basic cases are considered here: well-known random distributions and simple relationships, such as $r_{\max}/r_{\min} = C$ or $r_{\max} - r_{\min} = C$, with C a constant. In this example, a uniform distribution between $r_{\min}$ and $r_{\max}$ is used, and a constant ratio: $r_{\max}/r_{\min} = 4$ with $r_{\max} = r_{\text{theo}}$. The expression is:

$$r \sim U(r_{\text{theo}}/4, r_{\text{theo}})$$

The generation is shown in Figure 2.9. It contains 3170 particles, the polydispersity is $\lambda = 14.72$. It is quite close to the ratio of the maximum theoretical radius at the top to the minimum theoretical radius at the bottom :

$$\lambda_{\text{theo}} = \frac{r_{\text{theo}}(1)}{r_{\text{theo}}(-1)/4} = 16$$

$$
\begin{aligned}
&\text{minimize} \quad f(x^*, y^*) = y^* \\
&\text{subject to} \quad \begin{cases} d_i(x^*, y^*, r) \geq 0, & i = 1, \ldots, n \\ r_{\min} = r_{\min}(y^*_{\text{approx}}) \\ r_{\max} = r_{\max}(y^*_{\text{approx}}) \\ r \sim \mathrm{P}(r_{\min}, r_{\max}) \end{cases}
\end{aligned}
$$

Figure 2.8: Optimization problem with random polydispersity.

The packing fraction is $\phi = 0.82$. Despite the uniform distribution of the radii between $r_{\min}$ and $r_{\max}$, the real distribution of radii is not uniform. As $r_{\min}$ and $r_{\max}$ depend on y^*, the global distribution does not follow the local one, as shown in Figure 2.10.

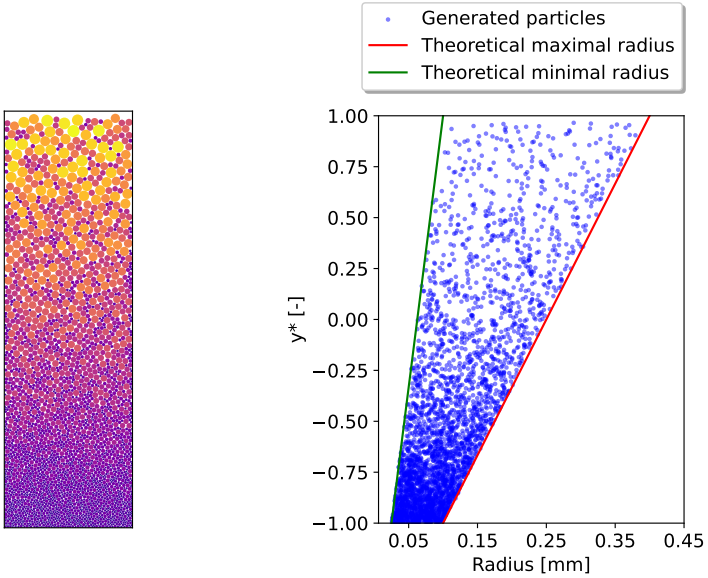

Figure 2.9: Particle generation with a linear law of radii and constant local polydispersity. The radii of particles are uniformly chosen between the maximal and minimal radius.

The last addition needed for the algorithm is to be able to modify the position of the particle along the x-axis, according to its radius. The function $f(y^*)$ that is minimized is changed to $f(x^*, y^*, r)$ such that it does not take the lowest possible point but the point that best fits the distribution. As r varies randomly, f can be defined such that the score of a big particle $r \approx r_{\max}$ is lower for x values where the distribution needs big particles, and inversely it is lower for big particles $r \approx r_{\min}$ for x values where the distribution asks for small particles. The minimization problem is written in 2.11.

The solution is still found by using the line Ψ, but now the point chosen is the one minimizing f. However, it should be noted that this solution only minimizes f with the condition that $d_i = 0$ for at least one grain, which is not necessarily the minimum of f in the $\{x^*, y^*\}$ space.

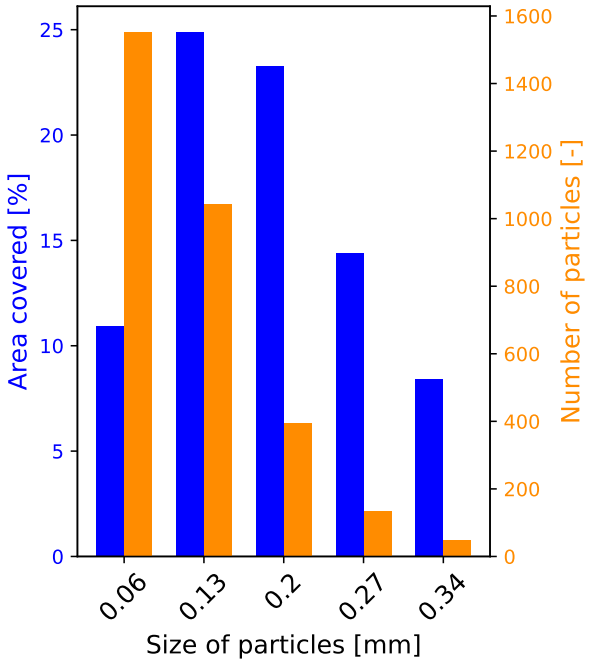

Figure 2.10: Number of particles of different sizes and the area covered as a fraction of the total area. The radii and total area covered are not uniform. Most particles are small ones while most of the area is covered by middle-sized particles.

For example, a distribution with big particles on the left and small particles on the right can be generated using this score function :

$$f(x^*, y^*, r) = C(r)x^* + D(r) + E(r)y^*$$

The values C, D, and E are set to meet a few properties: the function has to be increasing for large r so that the large particles are favored on the left, and decreasing for small r. The score function is set to be equal to 0 at $x^* = 0$ for all r so that $D(r) = 0$. The function is then set to be equal to 1 at $x^* = 1$ for $r = r_{\max}$ and -1 for $r = r_{\min}$. This gives, using $r_{\max} = 4r_{\min}$ and setting $y^* = 0$ for simplicity:

$$C(r) = \frac{r - \frac{r_{\max}+r_{\min}}{2}}{\frac{r_{\max}-r_{\min}}{2}} = \frac{r - \frac{5}{8}r_{\max}}{\frac{3}{8}r_{\max}}$$

The value of $E(r)$ is then chosen arbitrarily, here $E(r) = 25$. this choice was made after testing a few values: values close to 1 lead to deposits where there were close to no particles in the center (due to the small influence of the y^* in comparison with the x^*, while too large values created deposits where the particles did not follow the x-axis distribution as the impact of the y^* component was too large. The drawback of this method is that local polydispersity is needed to generate varying radii along the x-axis.

The final generation is presented in figure 2.12. The 2 bottom graphs show the radius of particles as a function of x^* for different heights on the left, and the score function for different radii at $y^* = 0$ on the right. It is made up of 3121 particles, the polydispersity is $\lambda = 15.19$ and the packing fraction is $\phi = 0.79$. The polydispersity is almost unchanged as the maximum and minimum sizes were not changed, the small reduction in packing fraction is due to the region with a large radius (top left) where large gaps appear between particles. As expected, the distribution of the size of particles is unchanged with respect to the distribution without the score function implementation.

$$\text{minimize} \quad f(x^*, y^*, r)$$

$$\text{subject to} \quad \begin{cases} d_i(x^*, y^*, r) \geq 0, & i = 1, \ldots, n \\ r_{\min} = r_{\min}(y^*_{\text{approx}}) \\ r_{\max} = r_{\max}(y^*_{\text{approx}}) \\ r \sim \mathrm{P}(r_{\min}, r_{\max}) \end{cases}$$

Figure 2.11: Optimization problem with x-axis distribution.

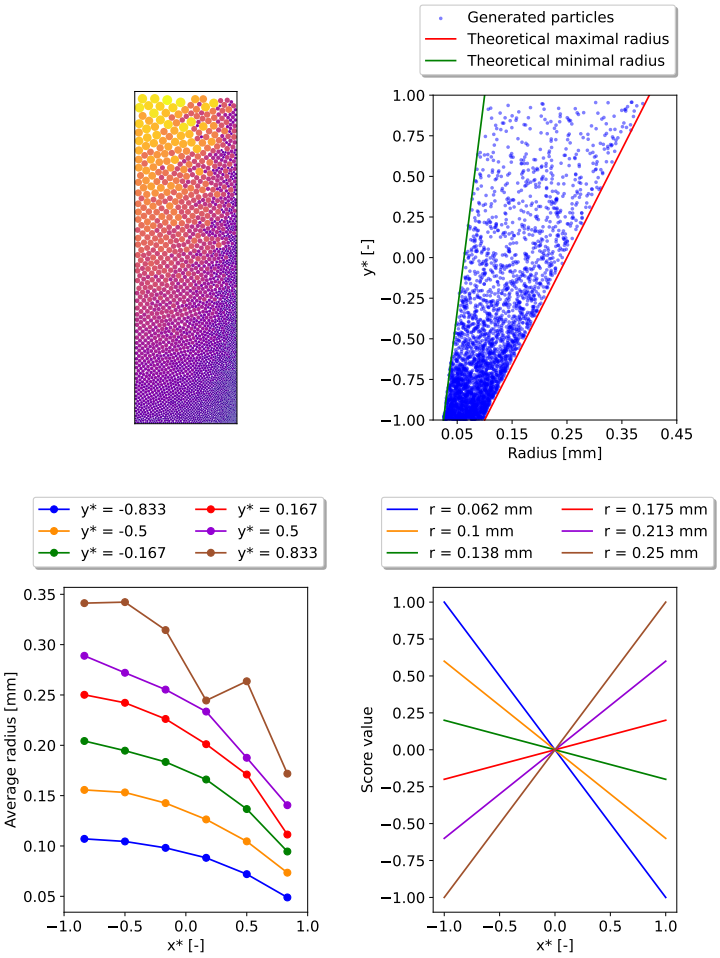

Figure 2.12: Particle generation with a linear distribution across the x-axis.
The score value is increasing for large radii and decreasing for small radii. The distribution seen in the figure on the left is not perfectly linear due to the effects of randomness and the particles close to the boundaries.

2.3 Increasing compactness and stability

Compactness of the deposit can be increased by reducing the space between particles, which is achieved by reducing particle size. However, the original radii distribution has to be preserved. A rule is defined for the size of the particle: the insertion of the particle of size r already defined is compared to the insertion of a particle of size $0.9r$. If the score function of this second particle is lower than the first one, then the smaller particle is inserted. The value of 0.9 is chosen arbitrarily: a lower one reduces the overall size of particles, deviating from the original distribution, but increases further the compactness,

and the opposite for a larger one. The optimization problem is written in 2.13. It should be noted that the values x^* and y^* depend on the radius, as the possible points of insertion are on the line which depends on the radius. This algorithm is illustrated in Figure 2.14.

$$\text{minimize} \quad f(x^*, y^*, r')$$

$$\text{subject to} \quad \begin{cases} d_i(x^*, y^*, r') =\geq 0, & i = 1, \ldots, n \\ r_{\min} = r_{\min}(y^*_{\text{approx}}) \\ r_{\max} = r_{\max}(y^*_{\text{approx}}) \\ r \sim \mathrm{P}(r_{\min}, r_{\max}) \\ r' = \begin{cases} r & \text{if } \min f(x^*, y^*, r) \leq \min f(x^*, y^*, 0.9r) \\ 0.9r & \text{else} \end{cases} \end{cases}$$

Figure 2.13: Optimization problem with the compactness algorithm.

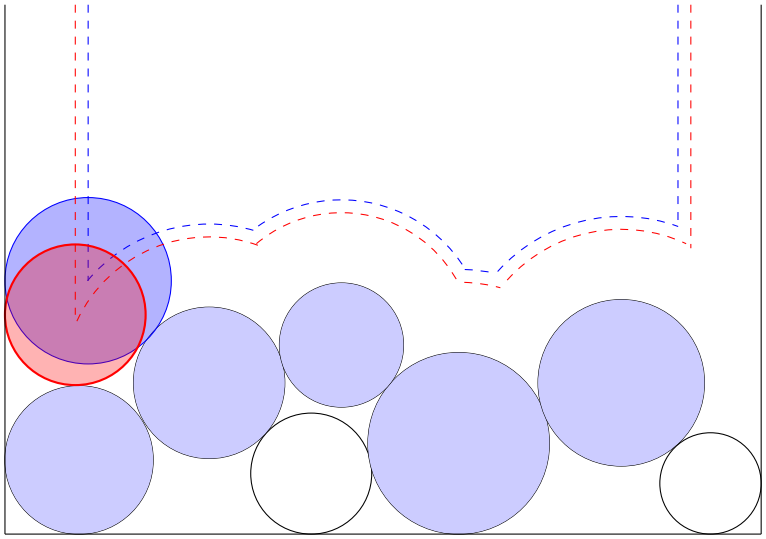

Figure 2.14: Illustration of the algorithm to increase compacity.
The red particle is inserted instead of the blue if its value of f is smaller.

The new generation is shown in Figure 2.15, it contains 3560 particles, with a polydispersity $\lambda = 16.52$ and a packing fraction $\phi = 0.81$. The distribution of particle size across the height is slightly shifted to the left as particles can be smaller than the theoretical value, and this leads to a denser generation. The polydispersity is slightly increased as the smallest radius is smaller while the largest one can stay the same. One could estimate this value using the value of $0.9r$ and the polydispersity of the generation without increased compactness: $\lambda = 16.52 \approx 15.19/0.9 = 16.88$. For the simulations ran here, the number of particles that were generated smaller than the radius computed at first ranges between half of the particles to all of them.

Finally, the stability of the deposit is reached using a contact dynamics simulation in Migflow. A dry simulation (without fluid) is run for a few tenths of a second until the deposit reaches stability. This leads to an increase in the packing fraction, however, this

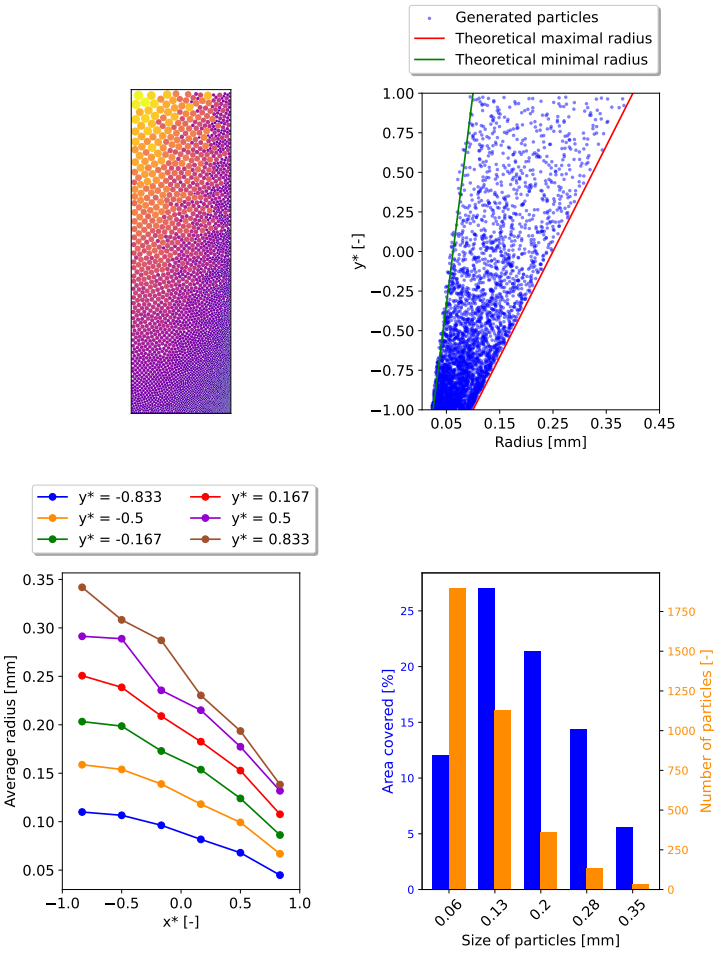

Figure 2.15: Particle generation with the compacity algorithm. The particles are globally smaller as some of them have a lower radius than from the original algorithm.

increase can't be observed by using the total area of the rectangle, as the area occupied by particles is not changed. The packing fraction is changed by the fact that the particles fall, creating a space on top of the generated deposit. Therefore, the real packing fraction ϕ_{real} is representative of this change. The results of this simulation are shown in Figure 2.16. The real packing fraction is $\phi_{\text{real}} = 0.82$. The particles are slightly moved but the global distribution is almost unchanged due to the small displacements. No friction is considered for the stabilization, but introducing it adds new stable arrangements of the grains.

A few possible improvements to the algorithm are presented in the appendix A.

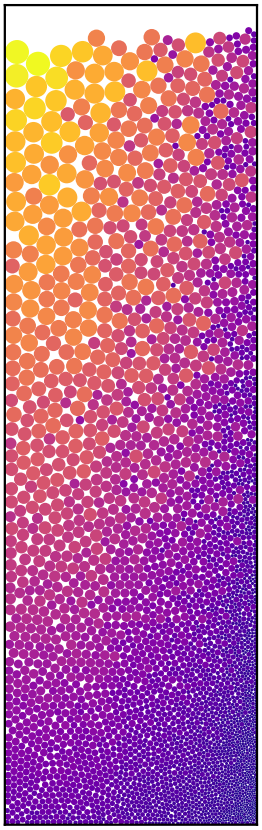

Figure 2.16: Stabilized deposit.
The particles are lower than in the non-stabilized deposit, reaching a more compact state.

2.4 Examples of possible particle generations

A few generations are detailed and compared in this section to show that the algorithm gives good results for multiple distributions. Finally, the generation required for the problem modeled in this master's thesis is described. At first, two deposits named 1a and 1b are generated, with a radius increasing linearly with y^*, without polydispersity or x-axis distribution. The first does not use the compactness algorithm and the second does. They are described in Figures 2.17 and 2.18. Then, deposit 2 is generated with a constant radius across the y-axis but polydispersity across x, it is defined in Figure 2.20. The third deposit uses a nonsymmetric profile for the radius across the height, and a constant difference between the maximum and minimum radii (see Figure 2.22). Finally, a fourth deposit described in Figure 2.24 uses a different probability distribution to change the area distribution of the particles. All the numerical values are shown in Table 2.1.

Deposit	$N_{\text{particles}}$	r_{smallest}	r_{largest}	λ	ϕ	ϕ_{real}
1a	3084	0.05mm	0.35mm	6.91	0.81	0.84
1b	3793	0.046mm	0.31mm	6.92	0.82	0.85
2	3181	0.06mm	0.2mm	3.33	0.81	0.84
3	5770	0.04mm	0.29mm	6.95	0.81	0.84
4	4584	0.06mm	0.2mm	3.33	0.81	0.84

Table 2.1: All numerical values for example deposits.

$$\text{minimize} \quad f(x^*, y^*, r) = y^*$$

$$\text{subject to} \quad \begin{cases} d_i(x^*, y^*, r) \geq 0, & i = 1, \ldots, n \\ r(y^*_{\text{approx}}) = -0.15 y^*_{\text{approx}} + 0.2 \text{ [mm]} \end{cases}$$

Figure 2.17: Optimization problem for the first deposit without compactness algorithm.

$$\text{minimize} \quad f(x^*, y^*, r') = y^*$$

$$\text{subject to} \quad \begin{cases} d_i(x^*, y^*, r') \geq 0, & i = 1, \ldots, n \\ r(y^*_{\text{approx}}) = -0.15 y^*_{\text{approx}} + 0.2 \text{ [mm]} \\ r' = \begin{cases} r & \text{if } \min f(x^*, y^*, r) \leq \min f(x^*, y^*, 0.9r) \\ 0.9r & \text{if } \min f(x^*, y^*, 0.9r) < \min f(x^*, y^*, r) \end{cases} \end{cases}$$

Figure 2.18: Optimization problem for the first deposit with compactness algorithm.

The first deposit uses a linear distribution of radii across the y-axis, with a locally mono-disperse law. The distribution across the x-axis is constant, as the maximum and minimum radii are equal. The radius at the bottom is fixed as $r_{\text{bottom}} = 0.35$ [mm] and the radius on the top as $r_{\text{top}} = 0.05$ [mm]. This deposit is generated in 2 ways: one without the compactness algorithm (1a) and one with (1b).

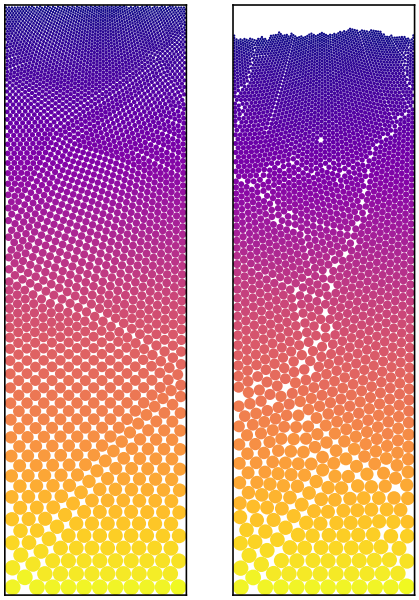

(a) Without compactness algorithm, the left figure is before stabilization.

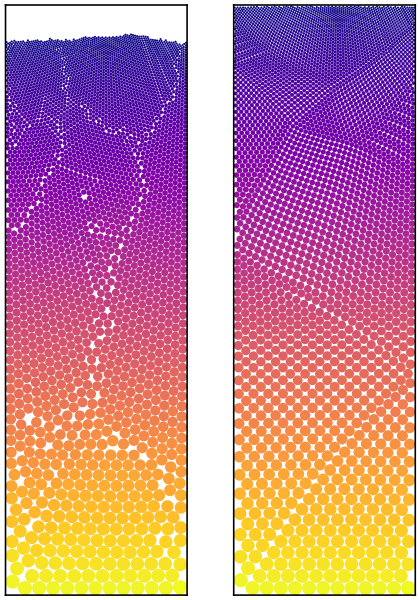

(b) With the compactness algorithm, the right figure is before stabilization.

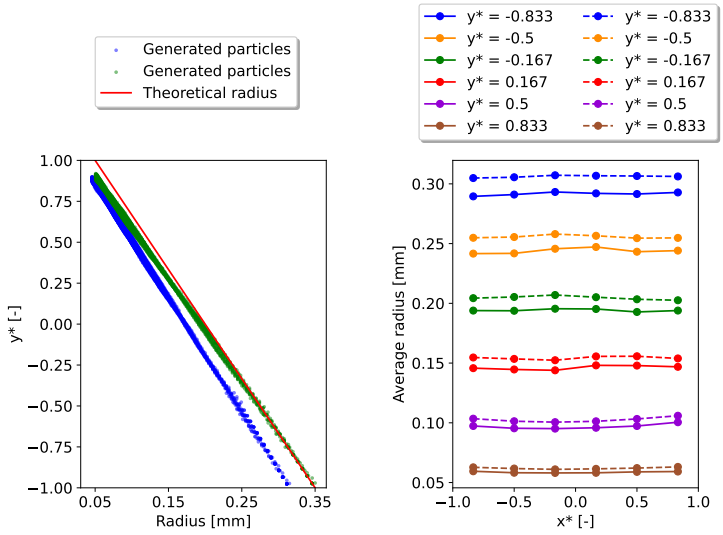

(c) Comparison between the 2 deposits.
On the left, the blue dots are for the compact algorithm, and the green ones are for the non-compact algorithm. The shift of the green dots at the top is due to the stabilization of the deposit, while the shift of the blue dots at the bottom is due to the compactness algorithm that reduces the radii in some cases. On the right, the dashed lines are for the non-compact algorithm.

Figure 2.19: Deposit 1 with and without compactness algorithm.

The generation with the compactness algorithm reaches a slightly higher packing fraction, but the values are close. However, the gains in packing fraction are not linear: increasing the packing fraction from 0.81 to 0.82 is much more difficult than increasing it from 0.5 to 0.51 for example. The influence of the increased compactness is visible on the graph of the radii as a function of the height: the blue dots are shifted to the left as the radii can be smaller. In this case, the radii are nearly always chosen smaller. For the deposit without compactness algorithm, a slight shift to the left appears at the top, due to the stabilization of the deposit: particles fall and the radii are smaller than they should be at this height. From here, all generations are run with the compactness algorithm.

A constant distribution of radii across the y-axis is used for the second deposit, with a radius of 0.2mm and a locally constant polydispersity. A parabolic distribution across the

x-axis is used, with the small particles in the center and the larger ones on the sides.

$$\text{minimize} \quad f(x^*, y^*, r') = y^*$$

$$\text{subject to} \quad \begin{cases} d_i(x^*, y^*, r') \geq 0, & i = 1, \ldots, n \\ r_{\max} = 0.2 \text{ [mm]} \\ r_{\min} = \frac{r_{\max}}{3} \text{ [mm]} \\ r \sim \mathrm{U}(r_{\min}, r_{\max}) \\ r' = \begin{cases} r & \text{if } \min f(x^*, y^*, r) \leq \min f(x^*, y^*, 0.9r) \\ 0.9r & \text{if } \min f(x^*, y^*, 0.9r) < \min f(x^*, y^*, r) \end{cases} \end{cases}$$

Figure 2.20: Optimization problem for the second deposit with constant radius across the height.

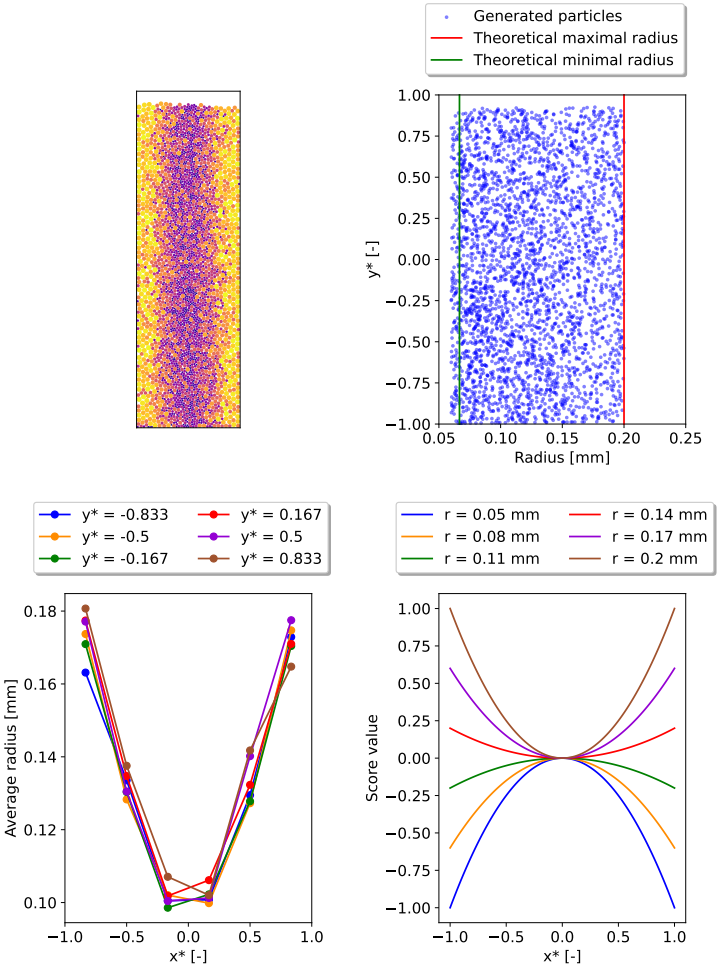

Figure 2.21: Deposit 2.
The parabolic distribution across the x-axis is clear, while the distribution across the y-axis is constant, the curves on the bottom left illustration are identical.

The deposit is shown in Figure 2.21. It shows a similar packing fraction as deposit 1a, even though the polydispersity is halved. This proves that choosing the right distribution and parameters allows for high compacity without increasing the polydispersity.

For the third deposit, a parabolic distribution of radii across the y-axis is used with big particles on the sides and a slight shift, so that the radii at the top, bottom, and center are $r_{\text{top}} = 0.3$ [mm], $r_{\text{bottom}} = 0.2$ [mm] and $r_{\text{center}} = 0.1$ [mm]. The difference between maximum and minimum radius is locally constant and big particles are placed on the right. The deposit is shown in Figure 2.23. There are more particles than the first deposits, but the packing fraction is the same. The radii are not symmetric along the y-axis, as expected.

$$\text{minimize} \quad f(x^*, y^*, r') = -\frac{(r-(r_{\max}+r_{\min})/2)}{(r_{\max}-r_{\min})/2}x^* + 25y^*$$

$$\text{subject to} \quad \begin{cases} d_i(x^*, y^*, r') \geq 0, & i = 1, \ldots, n \\ r_{\max}(y^*_{\text{approx}}) = 0.15(y^*_{\text{approx}})^2 + 0.05y^*_{\text{approx}} + 0.1 \text{ [mm]} \\ r_{\min} = r_{\max} - 0.05 \text{ [mm]} \\ r \sim \text{U}(r_{\min}, r_{\max}) \\ r' = \begin{cases} r & \text{if } \min f(x^*, y^*, r) \leq \min f(x^*, y^*, 0.95r) \\ 0.95r & \text{if } \min f(x^*, y^*, 0.95r) < \min f(x^*, y^*, r) \end{cases} \end{cases}$$

Figure 2.22: Optimization problem for the third deposit with constant radius across the height.

A fourth deposit is generated using the same parameters as deposit 2 but with a different distribution law: a variable u is defined between 0 and 1 using a uniform distribution. Then, the radius is computed as :

$$r = \frac{r_{\max} r_{\min}}{r_{\max} + u(r_{\min} - r_{\max})}$$

Physically, this distribution leads to a uniform distribution of the areas, so there are more small particles and fewer larger ones. The slightly decreasing radii distribution on the left is due to the compactness algorithm. The results are shown in Figure 2.25.

Despite an increase in the number of particles, the packing fraction stays close to the packing fraction of deposit 2. The interpretation of this result is that the larger particles of deposit 2 are replaced with multiple smallest particles in deposit 4, but the total area is the same. Therefore, more particles cover the same area, without changing the packing fraction.

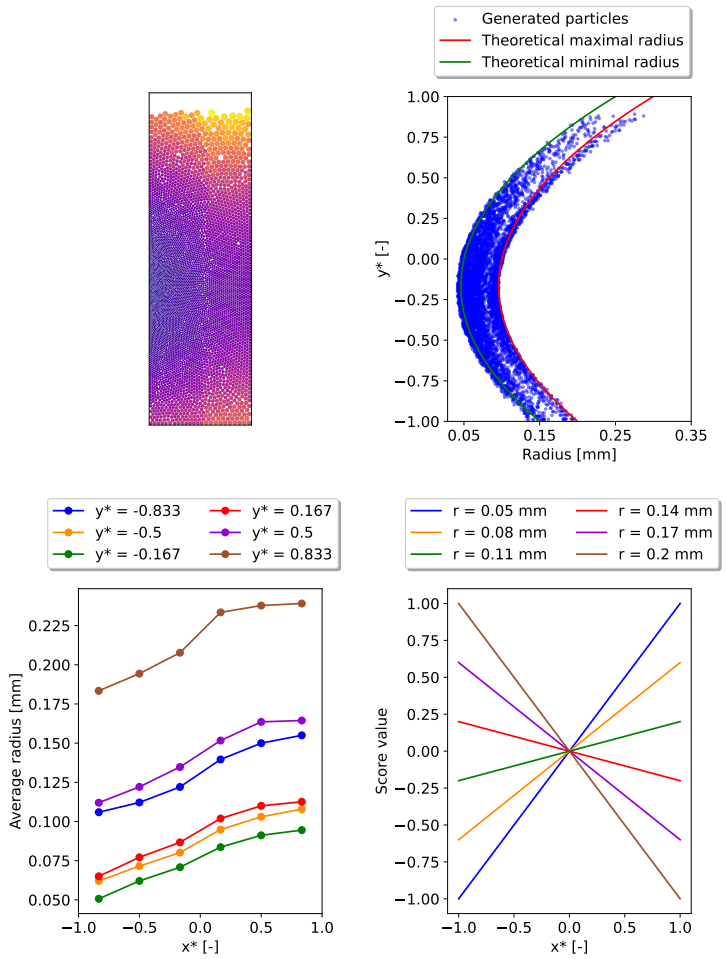

Figure 2.23: Deposit 3.
The size along the y-axis is not symmetric, as the smallest particles are slightly below the center.

$$\text{minimize} \quad f(x^*, y^*, r') = y^*$$

$$\text{subject to} \quad \begin{cases} d_i(x^*, y^*, r') \geq 0, & i = 1, \ldots, n \\ r_{\max} = 0.2 \text{ [mm]} \\ r_{\min} = \frac{r_{\max}}{3} \text{ [mm]} \\ u \sim \mathrm{U}(0, 1) \\ r = \frac{r_{\max} r_{\min}}{r_{\max} + u(r_{\min} - r_{\max})} \\ r' = \begin{cases} r & \text{if } \min f(x^*, y^*, r) \leq \min f(x^*, y^*, 0.95r) \\ 0.95r & \text{if } \min f(x^*, y^*, 0.95r) < \min f(x^*, y^*, r) \end{cases} \end{cases}$$

Figure 2.24: Optimization problem for the fourth deposit with a different probability distribution.

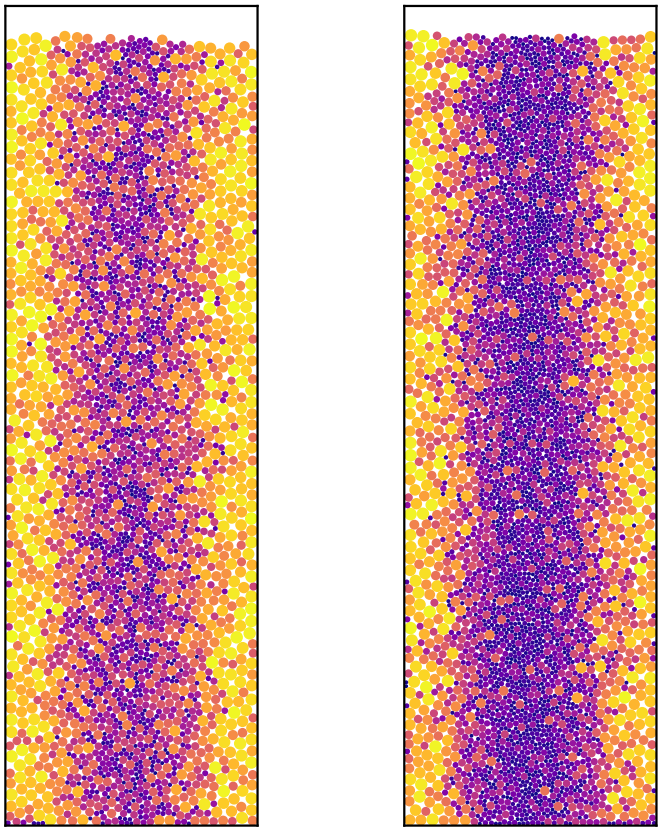

(a) Deposit 2.

(b) Deposit 4.

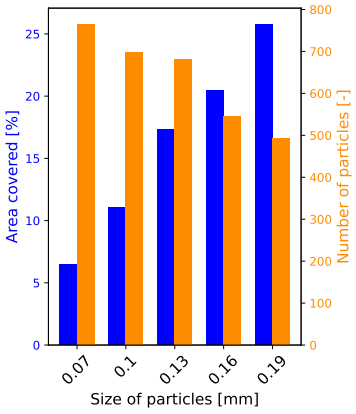

(c) In deposit 2, the number of particles for each size is quite uniform due to the distribution law chosen. The small decrease is due to the compactness algorithm that tends to reduce the size of the particles.

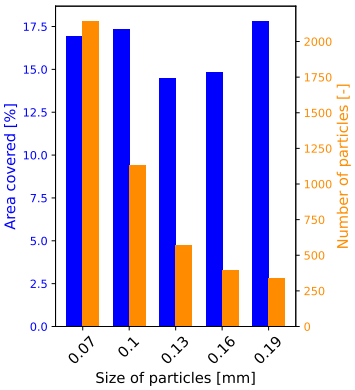

(d) In deposit 4, the total area covered for each size is uniform and the number of particles for each size is decreasing.

Figure 2.25: Comparison of deposits 2 and 4. The deposit 4 on the right contains more small particles.

2.5 Generation of 6 pellets for the simulations

The deposit generated for the simulations is based on the studies on fuel fragmentation. In (Karlsson et al. 2017) and (Capps et al. 2020), the fragment size reaches the diameter of the cladding around three pellets away from the crack, so six pellets will be generated here with a crack localized in the center ($h_{\text{ref}} = 78$ [mm], $w_{\text{ref}} = 8$ [mm]). No clear description or image of the fragmentation is given, but the data can be matched so that the deposit used is close to reality. The criteria used are the following: the mass distribution has to be close to the distributions shown in 1.1 (here, the size of particles is defined based on their radii, as the real particles are polyhedron), and the size of the particles is defined at some points of the column. These points are: the radius of particles on the top and bottom of the column is 1.5 mm with a small local polydispersity (low fragmentation), the radius of particles in the center of the column is 0.2 mm, and the particles close to the crack (on the left and right of the center of the column) have a radius of 0.05 mm (M. Flanagan 2012).

From these criteria, the equations can be determined and are found in 2.26. First, the y-axis equation is parabolic and gives a theoretical radius of 0.2 mm at $y^* = 0$ and 1.5 mm at $y^* = \pm 1$. Then, the distribution law used is the same as for the fourth deposit as it allows for a better distribution of the number of particles. The relationship between r_{theo}, $r_{\max}$ and $r_{\min}$ is more complex: the polydispersity is close to 1 at the top and bottom of the column due to low fragmentation while the polydispersity is close to 4 at the center. The score function is also parabolic as the fragmentation is considered to be axisymmetric. The particles are small on the sides and large on the center.

$$
\begin{aligned}
&\text{minimize} \quad f(x^*, y^*, r') = \frac{(r' - (r_{\max}+r_{\min})/2)}{(r_{\max}-r_{\min})/2} x^* + 25y^* \\
&\text{subject to} \quad \begin{cases}
d_i(x^*, y^*, r') \geq 0, & i = 1, \ldots, n \\
r_{\max}(y^*_{\text{approx}}) = 0.2(y^*_{\text{approx}})^2 + 1.3 \text{ [mm]} \\
r_{\min}(y^*_{\text{approx}}) = \frac{r_{\max}(y^*_{\text{approx}})}{4 - 3|y^*_{\text{approx}}|} \text{ [mm]} \\
u \sim U(0,1) \\
r = \frac{r_{\max} r_{\min}}{r_{\max} + u(r_{\min} - r_{\max})} \\
r' = \begin{cases} r & \text{if } \min f(x^*, y^*, r) \leq \min f(x^*, y^*, 0.9r) \\ 0.9r & \text{if } \min f(x^*, y^*, 0.9r) < \min f(x^*, y^*, r) \end{cases}
\end{cases}
\end{aligned}
$$

Figure 2.26: Optimization problem for the 6 pellets.

The size distribution (shown in Figure 2.27) is slightly different because of the low number of big particles (most of them are above or below the 6 generated pellets) and the most tiny particles not being generated due to their low impact on the flow and high computational cost. It consists of 4972 particles with $r_{\text{largest}} = 1.35$[mm],$r_{\text{smallest}} = 0.05$ [mm], $\lambda = 29.8$, $\phi = 0.78$, $\phi_{\text{real}} = 0.81$. The column is not filled at the top as the radius would be too large, but this is not a problem as the large particles are not the main interest here.

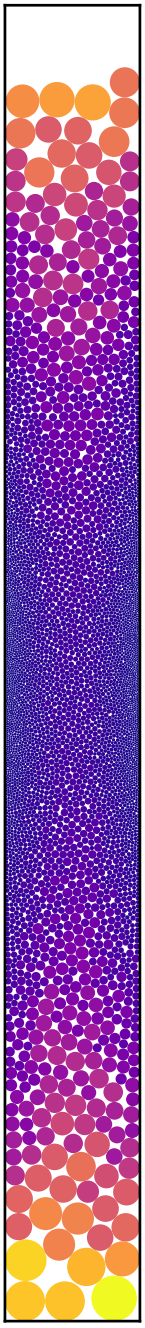

(a) Illustration of the generation.

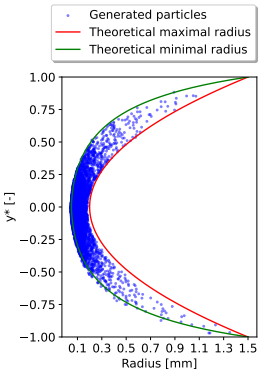

(b) The particles are generated correctly with a slight shift due to compactness and stabilization.

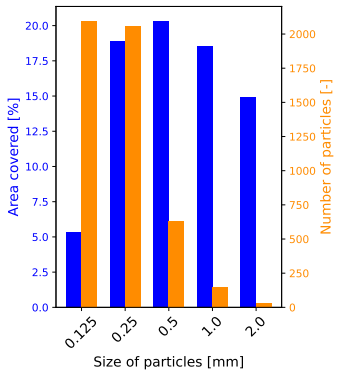

(c) The area distribution is close to the one in Figure 1.1.

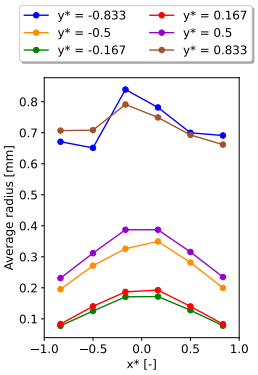

(d) The radii are smaller near the edges at $y^* = 0$ and quasi constant on top and bottom. The distribution is symmetric.

Figure 2.27: Particle generation used for the simulations.

Chapter 3

Physical and numerical modeling of the relocation problem

This chapter presents the resolution of the CFD-DEM problem. The physical, numerical, and geometrical parameters are first described, with the mesh used for the simulation. Then, the modeling of the problem is discussed: ... The model is based on the literature review, and the various options to model and estimate the physical phenomenon are compared. The results here are not quantitative: as will be seen, the models approximate the flow (especially, the fact that only six pellets instead of the whole column greatly reduces the accuracy of the results obtained), ignoring some important characteristics. The objective is therefore to show tendencies in a qualitative and phenomenological approach instead of giving exact quantitative results. Furthermore, the lack of experimental data would anyway not allow to confirm or invalidate the results.

3.1 Description of the simulation

The geometry is based on particle generation. It consists of six pellets of 13 mm in height and 8 mm in diameter in two dimensions. The crack is in the center, on the right. The length of the crack h is a physical parameter that will be studied further and is at first set to $h = 5$ [mm], and the cladding thickness $e = 0.75$ [mm] (D'Auria 2017). The ballooning effect is ignored, as the particle distribution already takes part of the phenomenon into account. A large area is simulated on the right of the crack to allow the particles to flow freely. The fluid outside of the cladding is the fluid of the primary cooling circuit, which is liquid water or water vapor in the case of a LOCA, but it is not modeled as it requires a two-phase simulation.

The simulated fluid is helium at 80 bar and 1200 °C (the influence of fission gases such as xenon is neglected) and particles are made of uranium dioxide. All the physical properties are listed in Figure 3.1. It should be noted that the properties of helium vary with the pressure and temperature, something that is not modeled here as the state considered is the initial state (Carbajo 2001) (Arp & Mccarty 1989).

The mesh is generated using GMSH and is shown in Figure 3.1. The characteristic length of the triangular elements is $l_c = 0.5$ [mm] in the cladding, which is about the size of the smallest particles. As the focus of the work is on the cladding and the crack, the large area on the right is simulated using a coarse mesh with a characteristic length 20 times larger, and the particles are deleted from the simulation once they reach a numerical limit on the right. The mesh near the crack is refined up to a size of $l_c/5 = 0.1$ [mm]. The boundary conditions are separated into multiple parts: on the left and right of the

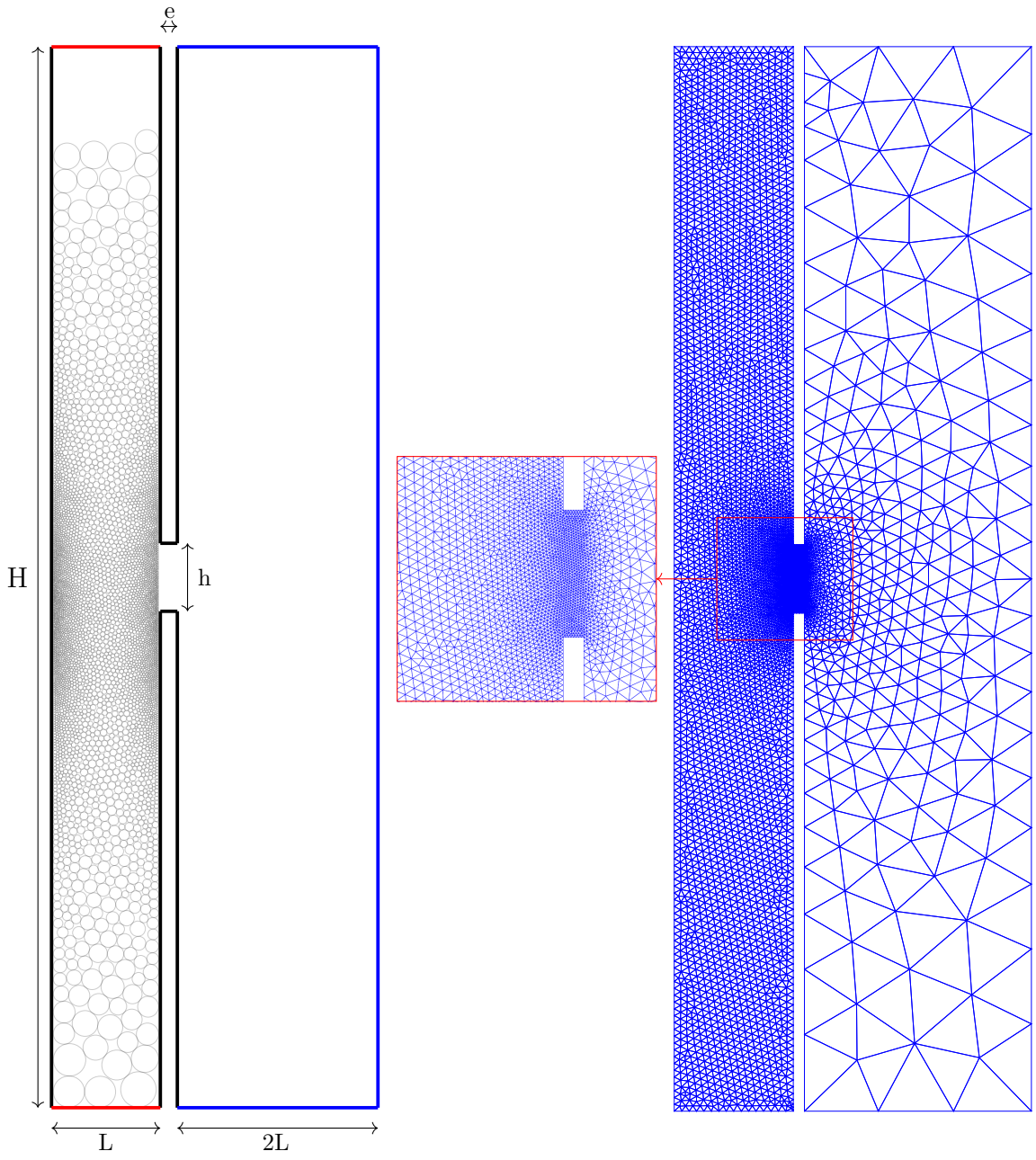

Geometrical parameters	Physical parameters	Numerical parameters
H = 7.800 10^{-2} [m]	g = 9.810 [m s^{-2}]	Δt_{fluid} = 1.000 10^{-6} [s]
h = 5.000 10^{-3} [m]	ρ = 2.602 [kg m^{-3}]	$\Delta t_{\text{particles}}$ = 2.000 10^{-7} [s]
L = 8.000 10^{-3} [m]	μ = 6.081 10^{-5} [kg m^{-1} s^{-1}]	t_{end} = 2.500 10^{-2} [s]
e = 0.750 10^{-3} [m]	ρ_p = 1.056 10^{5} [kg m^{-3}]	N_{nodes} = 5737
		N_{elements} = 11473

Figure 3.1: Geometry, mesh, and data used for the simulation.

cladding is a wall (black in the figure). On the top and bottom, the boundary conditions represent the column of pellets that are above and below the 6 simulated pellets (red). Finally, the condition on the far right (around the coarse area, blue) represents the primary coolant flow that is lost during the LOCA. The time step size and total simulated time are variable and will be detailed in each subsection, due to the high differences in velocities of the fluid and particles depending on the boundary conditions and phenomenon. At first,

the total time is $t_{\text{end}} = 2.500\ 10^{-2}$ [s] and the time step for the fluid is $\Delta t_{\text{fluid}} = 1.000\ 10^{-6}$ [s]. For the particles, a smaller time step is used, here $\Delta t_{\text{particles}} = \Delta t_{\text{fluid}}/5 = 2.000\ 10^{-7}$ [s]. For each iteration of the fluid problem, 5 iterations of the particle movement are done, which leads to good accuracy while keeping a low numerical cost.

Only two simple boundary conditions will be used. The outside boundary is considered to be representative of the primary circuit. Depending on the exact failure and time of cladding rupture, this pressure varies from 1 to 10 bar. For now, a value of 1 bar is used with an open boundary. Physically, it means that the flow at points of this boundary has imposed pressure. The wall of the cladding is a wall boundary condition, which means that the flow can't go through the boundary, the normal velocity is zero. The definitions of the boundary conditions are found in Appendix B.

The flow simulated contains intrinsic high-frequency temporal and spatial disturbances because of the fluid-grains interactions. Therefore, the quantities such as the velocity magnitude, pressure, etc. will be averaged over time and space. A quantity $q(\boldsymbol{x}, t)$ can be averaged over a surface S:

$$\overline{q(\boldsymbol{x}, t)} = \frac{\int_S q(\boldsymbol{x}, t) dS}{\int_S dS}$$

Similarly, the quantity $q(\boldsymbol{x}, t)$ can be averaged over a time Δt, which is the moving average around t :

$$\langle q(\boldsymbol{x}, t) \rangle = \frac{\int_{t-\Delta t/2}^{t+\Delta t/2} q(\boldsymbol{x}, t') dt'}{\Delta t}$$

Using these quantities for the graphs instead of $q(\boldsymbol{x}, t)$ smooth out part of the disturbances. The choice of S and Δt is arbitrary: for S, the surface chosen is physically representative of a region. Here, the regions chosen are for example: the inner surface of the cladding, each geometrical pellet, or the region of the break. For Δt, the value is chosen to smooth the temporal variations so that the graphs are easier to read, however, the variations should still appear as they are part of the flow. Here, a value of $\Delta t = 1$ [ms] will be used.

3.2 Pressure difference modeling

The main driver of the flow is the pressure gradient. At the time of the rupture, the pressure inside the cladding is the containment pressure, which is from 25 to 80 bar depending on the type of rod (Brankov 2017) (Montgomery & Bevard 2020). The outside pressure is the pressure of the primary cooling circuit after the accident, which reaches a value below 10 bar before the rupture (Hussain & Nawaz 2016). This gradient drives the flow outside of the cladding, and the particles with it. Here, only the values of 80 bar inside and 1 bar outside are used, but the impact of this gradient will be studied later. Multiple models are here proposed and compared.

In the fluid solver, it is only possible to define the pressure at the boundaries. Therefore, the pressure has to be defined on the upper and lower boundaries of the cladding. This pressure should represent the pressure of the upper and lower parts of the cladding that are not modeled. An open boundary condition is needed because physically the fluid comes from the top and bottom of the cladding and a model for the pressure imposed is now necessary.

Constant pressure

The first way to model the pressure is to consider that the whole cladding is an infinite reservoir for the time of the ejection of the particles of the six pellets, leading to a constant pressure at these boundaries. This simple model allows for a first understanding of the characteristics of the flow.

$$p(t) = p_0 = 80 \text{ [bar]}$$

Figure 3.2: Boundary pressure definition for the constant pressure model.

Decreasing pressure

A second model is based on the estimation of the evolution of the pressure at these points. Indeed, the fluid outflow decreases the pressure in the cladding. This flow is driven by the pressure difference between the inside and outside of the cladding. Therefore, the pressure should follow a profile close to a decreasing exponential. The constants are determined by imposing two conditions: the initial pressure at the boundary inside the cladding and the asymptotic pressure. To find the time constant τ, a third condition is imposed: at $t = 0.025$ [s], the pressure has a value such that 99% of the pressure change has been reached. The time of ejection of all particles is slightly less than 25 ms, this value is so that the pressure is close to the outside pressure when most particles are outside, and the pressure gradient is sufficient over time to drive most of the particles outside. However, this time scale should be larger if the whole cladding was simulated.

$$p(t) = Ae^{-\frac{t}{\tau}} + B \text{ [bar]}$$

$$B = p_1 = 1 \text{ [bar]}$$

$$A = p_0 - p_1 = 79 \text{ [bar]}$$

$$\tau = \frac{0.025}{\ln(100)} = 5.43 \text{ [ms]}$$

Figure 3.3: Boundary pressure definition for the decreasing pressure model.

Source term

The models presented before don't represent the compressibility of the fluid. In Migflow, the simulation of compressible granular media is not possible at the moment. However, a simple source term can be added to the Navier-Stokes incompressible equations right-hand side of the continuity equation. Only considering the fluid phase, it reads :

$$\boldsymbol{\nabla} \cdot \boldsymbol{u} = s(t, \boldsymbol{x})$$

$$\frac{\partial \boldsymbol{u}}{\partial t} + (\boldsymbol{u} \cdot \boldsymbol{\nabla})\boldsymbol{u} = -\frac{1}{\rho}\boldsymbol{\nabla} p + \nu \nabla^2 \boldsymbol{u} + \boldsymbol{f}$$

The continuity equation imposes the values of u at each time step. Therefore, imposing a source term $s(t, \boldsymbol{x})$ imposes the spatial profile of $\boldsymbol{u}$ through its divergence. A positive divergence physically means that more flow enters the volume around $\boldsymbol{x}$ than flow leaves it. The velocity going out of the volume is larger than the velocity going in. As the density is constant, this can be thought of as an addition of fluid: in a small volume, an outgoing net flux is due to a source of fluid in the volume. The term s is a source if $s > 0$, and a sink if $s < 0$. While it is not physical compressibility, it is a good numerical approximation.

The function $s(t, \boldsymbol{x})$ has to be determined. Multiple possibilities exist here: for example, the source term can be linked to the density by using the compressible Navier Stokes equations and isolating $\boldsymbol{\nabla} \cdot \boldsymbol{u}$:

$$s(t, \boldsymbol{x}) = -\boldsymbol{u} \cdot \boldsymbol{\nabla}\rho - \frac{\partial \rho}{\partial t}$$

However, this needs a relationship for ρ and the value of $\boldsymbol{u}$ at each step. It would lead to a complex model with a high numerical cost. They still can be estimated: the term $\boldsymbol{u}$ will converge to zero at equilibrium. The density can be linked to the pressure by the ideal gas law :

$$pV = mR^*T$$

$$p = \rho R^*T$$

As the pressure also converges to a uniform value, $\boldsymbol{\nabla}\rho$ and $\frac{\partial \rho}{\partial t}$ tends to zero at equilibrium. The same thinking as with the decreasing boundary pressure gives that $s(t, \boldsymbol{x})$ should follow a profile close to the pressure profile, a decreasing exponential. The time constant τ is the same as for the boundary pressure. The multiplying constant is arbitrary: here a value of 1000 is chosen. This value is found by using dimensional analysis: the characteristic length is $H/2 = 39$ [mm], the characteristic time is $\Delta t = 0.025$ [s], and the density changes from 2.9 to 0.1 kg/m^3 during the depressurization, so $\Delta\rho = 2.8$ [kg/m^3]. Then,

$$s(t, \boldsymbol{x}) = -\boldsymbol{u} \cdot \boldsymbol{\nabla}\rho - \frac{\partial \rho}{\partial t} \Longrightarrow \langle s(t, \boldsymbol{x}) \rangle \approx -u \underbrace{\frac{\Delta\rho}{H/2}}_{\approx 70} - \underbrace{\frac{\Delta\rho}{\Delta t}}_{\approx 100}$$

The velocity u is unknown. Fixing it as $u \approx 1$ m/s gives $\langle s(t, \boldsymbol{x}) \rangle \approx 200$, which will be the value used here. The multiplying constant A is therefore chosen so that the average of $s(t, \boldsymbol{x})$ between $t = 0$ [s] and $t = 0.025$ [s] is 200, which gives $A = 1000$. It could be noted that the value of u is larger in the results, which means the compressibility effects are larger than estimated. However, in the real case, the depressurization is much slower due to the stronger interactions between the polyhedral grains. For example, in (Bonnet 2021), the velocity of the fluid is around a few meters per second, even though the model is more approximate but takes partially into account the non-spherical grains. The source term is only non-zero inside the cladding, as the outside pressure is assumed to be constant.

The boundary pressure imposed is the decreasing pressure over time, but it could be argued that if the source term is taken, the boundary condition should be a wall condition. These 2 possibilities are arbitrarily chosen: the wall condition corresponds to the simulation of only the 6 pellets, while the open boundary corresponds to a simulation where the rest of the cladding is approximated. In this case, the open boundary is used because the wall condition would lead to a depressurization considering only the fluid inside the 6 pellets, which is a small volume and would not be able to expel a significant part of the particles.

$$p(t) = 79e^{-\frac{t}{5.43\ 10^{-3}}} + 1 \text{ [bar]}$$

$$\boldsymbol{\nabla} \cdot \boldsymbol{u} = s(t, \boldsymbol{x}) = 1000e^{-\frac{t}{5.43\ 10^{-3}}} \text{ [s}^{-1}\text{]}$$

Figure 3.4: Boundary pressure and source term for the source term model.

Pressure estimation from fluid flow

This model tries to estimate the pressure at the boundaries from the flow in the crack. To do so, the fluid pressure is expressed using the ideal gas law :

$$pV = mR^*T$$
$$dp = \frac{R^*T}{V}dm$$

The fluid mass flow dm can be derived from the average velocity in the break in the x direction $\overline{u_x}$, where the average porosity in the break $\overline{\phi}$ is used because only the fluid flow is considered here :

$$dm = -\rho\overline{u_x}A\overline{\phi}$$

With A the area of the crack. In two dimensions, the volume is the area in the cladding and the area of the break is its height :

$$dp = -\frac{R^*T}{HL}\rho\overline{u_x}h\overline{\phi}$$

This can be integrated numerically at each time step to give the boundary pressure :

$$p(0) = 80 \text{ [bar]}$$
$$p(t + \Delta t) = p(t) - \tfrac{R^*T}{HL}\rho\overline{u_x(t)}h\overline{\phi}\Delta t$$
$$\boldsymbol{\nabla} \cdot \boldsymbol{u} = s(t, \boldsymbol{x}) = 1000e^{-\frac{t}{5.43\ 10^{-3}}} \text{ [s}^{-1}\text{]}$$

Figure 3.5: Boundary pressure and source term for the model with numerical estimation of the pressure.

The source term $s(t, \boldsymbol{x})$ could also be expressed as a function of p similarly than for the third model, however, it would lead to a larger complexity and won't be done here. The value of H should be the height of the cladding as the depressurization is in the whole cladding, and the simulation of the whole column would have a larger time scale. However, for the ejection of the six pellets simulated, using $H = 3.7$ [m] gives a nearly constant pressure profile, which does not show the impact of this pressure model. Therefore, the height of the six pellets is used and the time scale is similar to 0.025 s. While this model is a more physical estimation, it still does not represent truly the compressibility of the fluid, the estimation of the pressure does not take into account the particle flow, and the area of the cladding was numerically reduced to see the effects of the model.

Models comparison

At first, some characteristics of the flow are common for all models. In Figure 3.6, the particles are shown at different time steps for the model with a constant boundary pressure. The particles are colored so that the flow is easier to see. A shear movement of particles to the right appears, and the outgoing particles come from the top and the bottom equally. A region on the left appears where the particles are trapped and don't move, it is visible after 2.5 ms and 5 ms. This is due to the fluid moving to the right, and therefore this region on the center-left has a low velocity. This is less visible with the source term, as the velocity of the fluid also increases in this region because of the non-zero divergence.

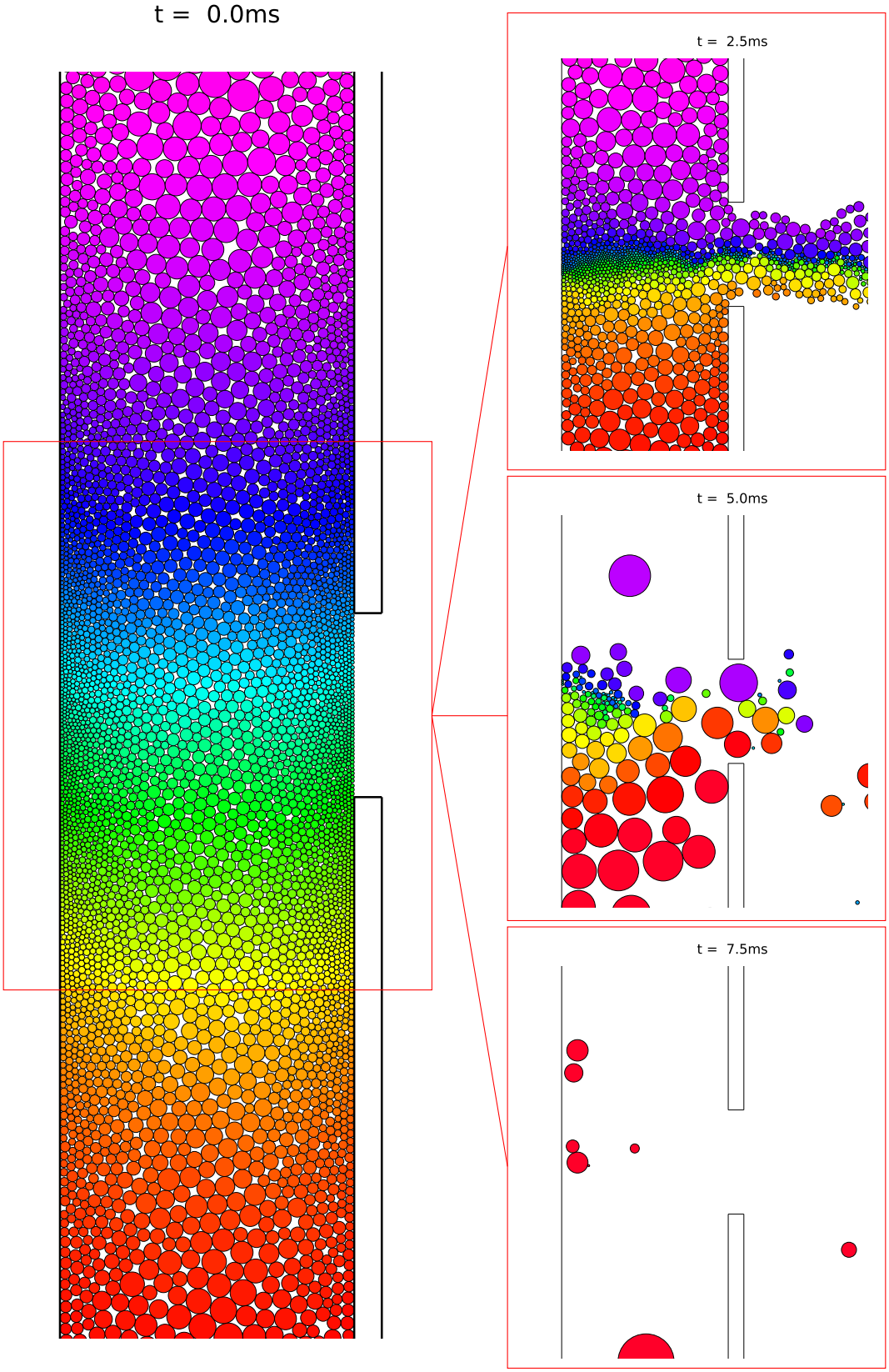

Figure 3.6: Snapshots of the middle part of the simulation with a constant boundary pressure of 80 bar. A shear movement of particles to the right is visible at 2.5 ms, and the small particles trapped on the left are still in the column after 5 ms.

The fluid flow is also comparable in some points for all models. Figure 3.7 shows snapshots of the fluid flow at different times with a constant boundary pressure, but the observations are common for all models. The fluid velocity contains high-frequency spatial variations due to the particles. As the fluid flows between the particles, it shows areas with large velocity (yellow) while other areas have a small (nearly zero) velocity because the fluid flows between the particles. The presence of particles around it can modify the flow through the crack. For example, at 7 and 10.5 ms, the flow is highly disrupted because of particles near or inside the break. Finally, a steady state is reached for the simulation with constant pressure.

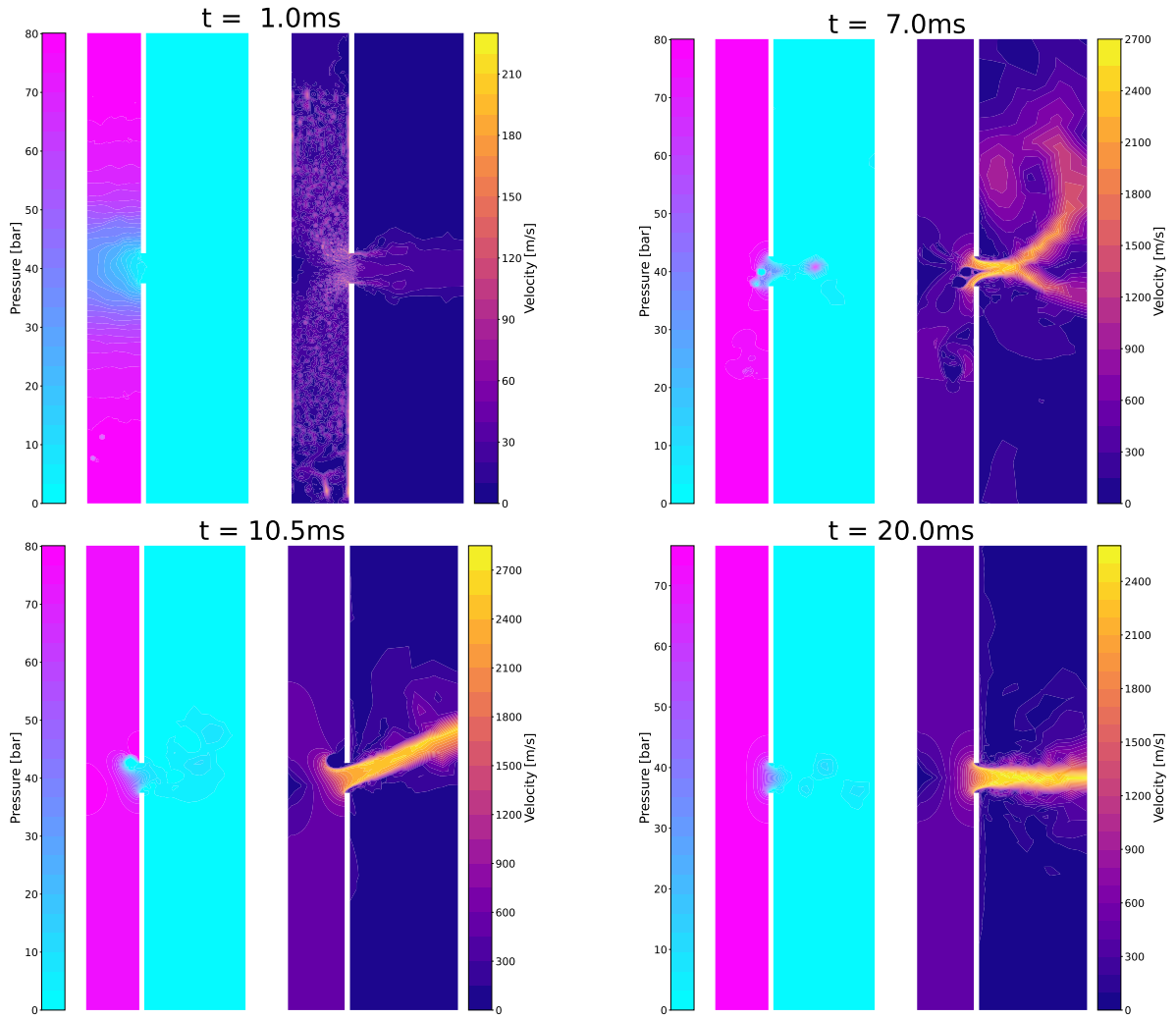

Figure 3.7: Snapshots of the fluid pressure (left) and velocity (right) fields with a constant boundary pressure. The velocity scale is variable to improve readability. The interactions between the fluid and the grains generate local variations of the fluid velocity, and a large pressure drop at early times when the column of particles is the denser.

The particle flow is illustrated in Figure 3.8, the mass flow is expressed in kg/(m s) because the problem is two-dimensional. Some differences can be observed. First, the mass flow for a constant pressure is larger but then drops as the ejection time is smaller. The two models with an imposed decreasing pressure are close, but the one with the source term has an initial flow that is larger with an earlier drop, which is due to the fluid velocity increase linked to the source term (this will be studied further in Figure 3.12). The model with a pressure estimation depending on the fluid flow has an initial mass flow similar to the others, but it is globally much lower as the pressure drops more rapidly (see Figure 3.11). The large source term leads to a separation of the particles due to the fluid expansion (see Figure 3.9) and some particles stay in the cladding, which is also visible

in the mass flow figure: low-frequency rebounds are observable in the curves because the mass flow is low when a separation between particles groups goes through the crack. It should also be noted that part of the particles are not ejected with the three models using a decreasing pressure. These particles would however be expelled if a whole column was simulated. In a case where the entire column was simulated, part of the mass and particle flow decrease would not appear, as it is partly due to the lack of particles to eject.

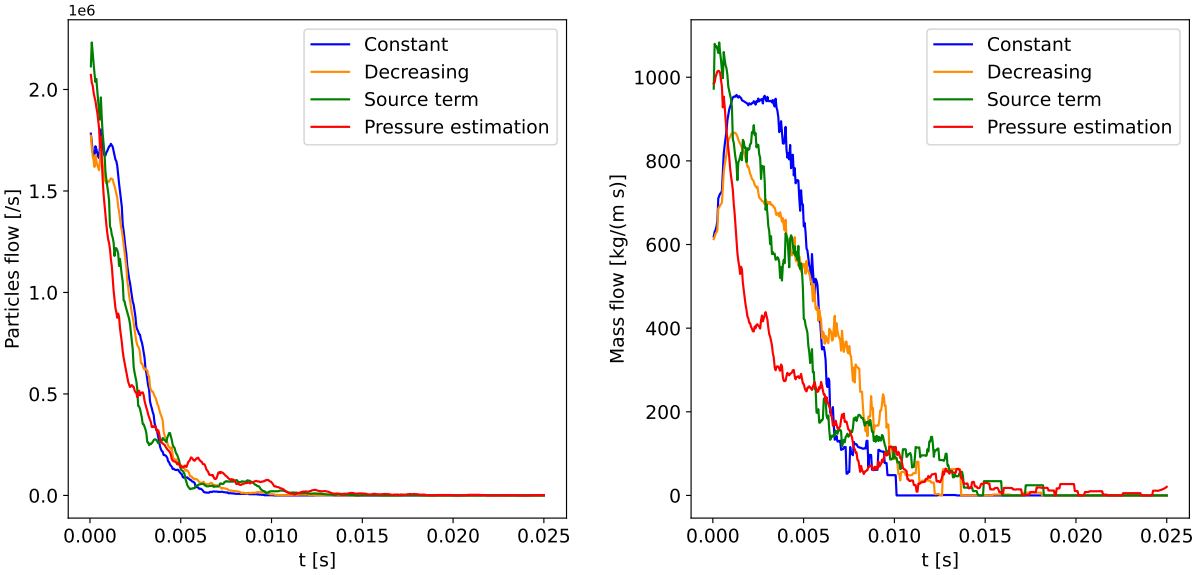

Figure 3.8: Average particle flow for the different pressure models. The mass flow is larger for the constant pressure with a smaller ejection time, and the two models with a decreasing exponential pressure are similar. The model with the numerical pressure estimation reaches a lower mass flow. The models with a source term have rebounds and low-frequency time variations of the flow.

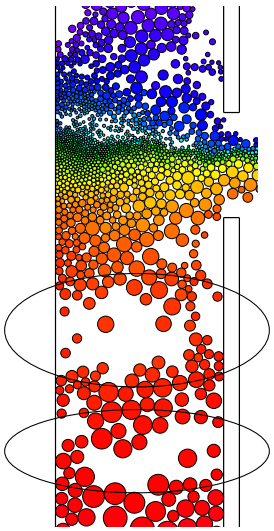

Figure 3.9: Particles separating in packs with empty regions between because of the fluid expansion.

The velocity of the particles can't be easily put into a graph, as it varies over time and space and is discontinuous, but snapshots can be shown to illustrate it. In Figure 3.10, the particles are drawn with a color gradient, from blue for the slow one to red for the fastest. The four models are compared after 0.5 ms when the particles reach their maximum velocity. This velocity is of the order of a few dozen meters per second around the breach, which is larger than in (Bonnet 2021) where a value around 1 m/s was found. The velocity in the cladding is however closer to this value. These differences are again

explained by the lower interactions between grains due to their spherical shape. The only strong difference between the models is due to the source term in the last two that largely increases the velocity after the break and pushes the grains forward.

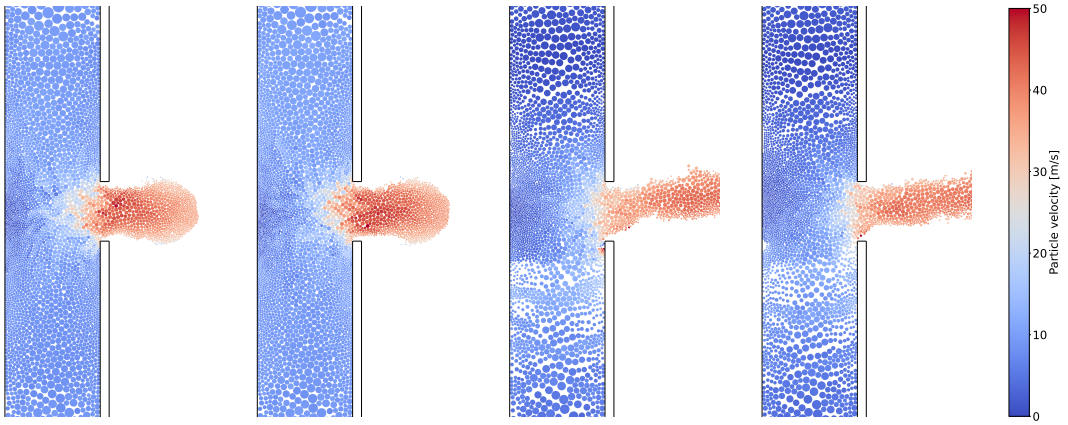

(a) Constant pressure (b) Decreasing pressure (c) Source term (d) Pressure estimation

Figure 3.10: Particle velocity for the four models at $t = 0.5$ [ms]. The results are similar, but the source term in the last 2 models increases the particle velocity after the break because the fluid velocity is larger. This also leads to particles in the cladding having a lower velocity because the source term maintains them. The low-velocity region on the left is seen with a deeper blue. The particle velocity is the largest at this time and decreases after.

While the main focus here is the particle flow, the fluid flow is still important as it drives the grains outside. The average pressure in the cladding is drawn on the left of Figure 3.11. On the right is the average pressure in the break. The pressure only increases for the constant pressure model, as part of the pressure loss is due to the particles that go out of the cladding. For the decreasing model and the source term, the pressure follows a similar curve as the boundary pressure mainly defines it. The source term model, however, begins with a larger pressure due to the positive divergence of $\boldsymbol{u}$, and also the fact that the value shown is the moving average and therefore consider the flow not only at $t = 0$ [ms]. In the two last models, the source term generates a high-pressure region at early times in the cladding, larger than 80 bar. While this is not physical, it is the numerical representation of the force applied by the fluid expansion on the grains.

The fluid velocity is highly dependent on the model. The pressure gradient drives this velocity, the models with a smaller gradient have a lower velocity. In Figure 3.12, the velocity through the break reaches a steady state with a constant boundary pressure of about 1200 m/s. This is a value way too large to have any physical meaning. For example, for a choked compressible flow which is the fastest velocity for a compressible flow, the maximum velocity of the fluid is $u^* = \sqrt{\gamma R^* T} \approx 720$ [m/s] in these conditions. Again, the models with and without source terms are similar with velocities that are still large. The pressure estimation model, finally, reaches lower fluid velocity (around 40 m/s during most of the relocation). Its profile is still decreasing until it reaches the steady state with a boundary pressure equal to the outside pressure.

The first model clearly shows results that are not interesting for this work: while the whole cladding simulation would lead to a larger time of relocation and a slower decrease of the pressure, the three last models are better in this case to show the characteristics of the flow. The two models with the imposed decreasing pressure show similar results and profiles that are close to the ones shown in Figure 1.2. The last model with the estimation of the pressure based on the flow through the break shows a pressure decreasing

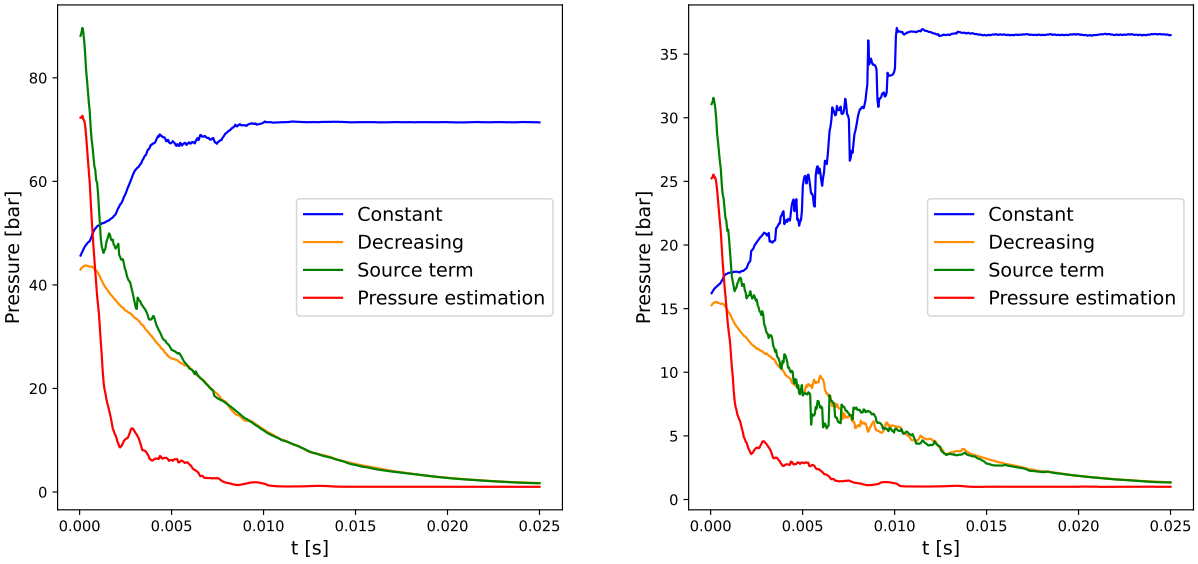

Figure 3.11: Average pressure in the cladding (left) and the break (right) for the different models. The constant pressure model reaches a steady state at the end, while the other models converge to 1 bar. The pressure estimation model drops significantly faster.

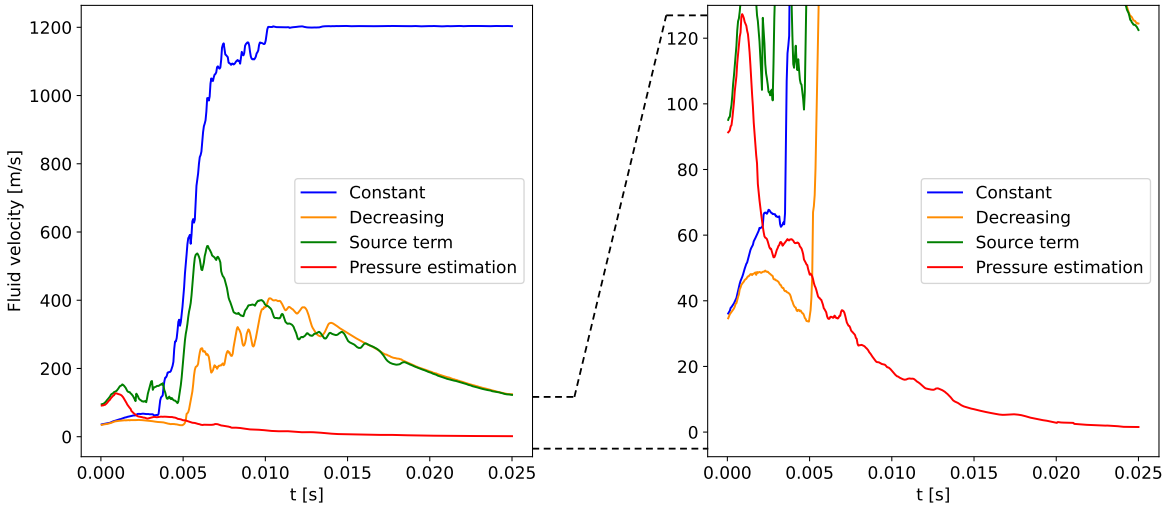

Figure 3.12: Average velocity in the break for the different models with a zoom on the pressure estimation model. The velocity profile for the model with pressure estimation is much lower because the spatial pressure drop is much lower.

faster and a much slower flow. This model however still does not perfectly represent the compressibility of the flow, and the pressure loss is only approximated. A table containing multiple criteria to compare the models is given in Table 3.1.

In summary, while some models provide interesting approximations and results, the last two models seem to capture the physics of the relocation quite well in a qualitative manner. However, they require a more detailed parametrization for both the source term and the computation of pressure evolution. None of these models accurately represent the effects of fluid compressibility, which is a significant factor in this flow. Ideally, a solver incorporating compressible granular flow would be suitable, but currently, there is none available with a DEM-CFD semi-resolved method. For the upcoming analysis, the primary model used will be the last one, with a numerical estimation of the pressure. However, some results related to other models will also be outlined.

Model	Pressure profile	Compressibility	Depressurization rate	Complexity
Constant pressure	✗	✗	✗	Low
Decreasing pressure	✓	✗	✗	Low
Source term	✓	∼	✗	Medium
Pressure estimation	✓	∼	∼	High

Table 3.1: Comparative table using criteria based on the physical phenomena included in the model and their complexity. The last model is more detailed but still approximate and more complex.

3.3 Friction between particles and with cladding

For now, friction was not considered in the simulations. Intuitively, it slows the grains because they interact together and with the wall. It should therefore lead to a decrease in the particle mass flow and an increase in the time of ejection. It was seen in Section 1.3 that the value of the friction coefficient was not determined clearly but should be at least around 0.3. Three values are therefore compared here : $\mu_f = 0$, $\mu_f = 0.3$ and $\mu_f = 0.5$.

The reduced mass flow due to friction is illustrated in Figure 3.13, where the flow is globally slower for larger friction coefficients. It can be seen that the rebound phenomenon in the particle flow observed before is amplified by the friction coefficient: it is much more visible for the curves with $\mu_f = 0.3$ and $\mu_f = 0.5$. The reason for this is that the friction leads to grains staying compact together, which means that the packs observed in Figure 3.9 are larger with large friction coefficients. The slowdown of the particle flow is much more visible without the source term because the source term separates the grains, leading to a lower friction influence.

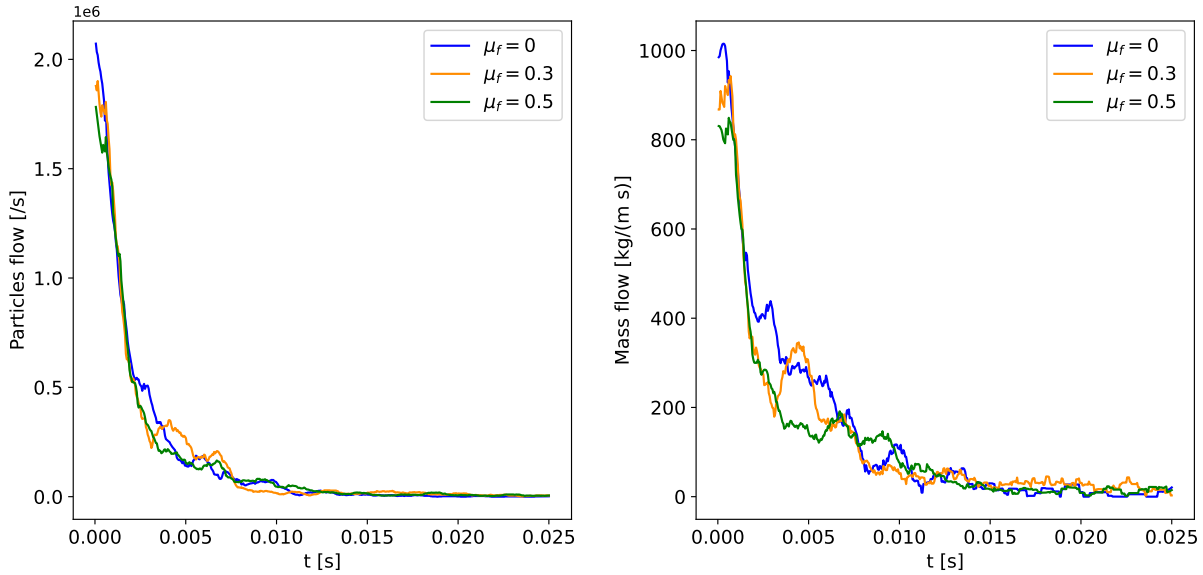

Figure 3.13: Particle and mass flow for various friction coefficients. A larger friction coefficient leads to a slower emptying. The rebounds already observed without friction are still visible.

With the models without source term, an interesting phenomenon appears, illustrated in Figure 3.14: for the coefficient $\mu_f = 0.5$, the upper part of the flow is favored: the particles in the lower part of the cladding don't move. This is due to the combination of gravity, friction, and weight of the upper part of the column, which together mitigate the effects of the pressure gradient. Therefore, the lower part stops moving for a while. Once most of the upper part has flown through the break, the lower part is free to move again. With a large coefficient such as $\mu_f = 0.5$, the time at which the upper part left

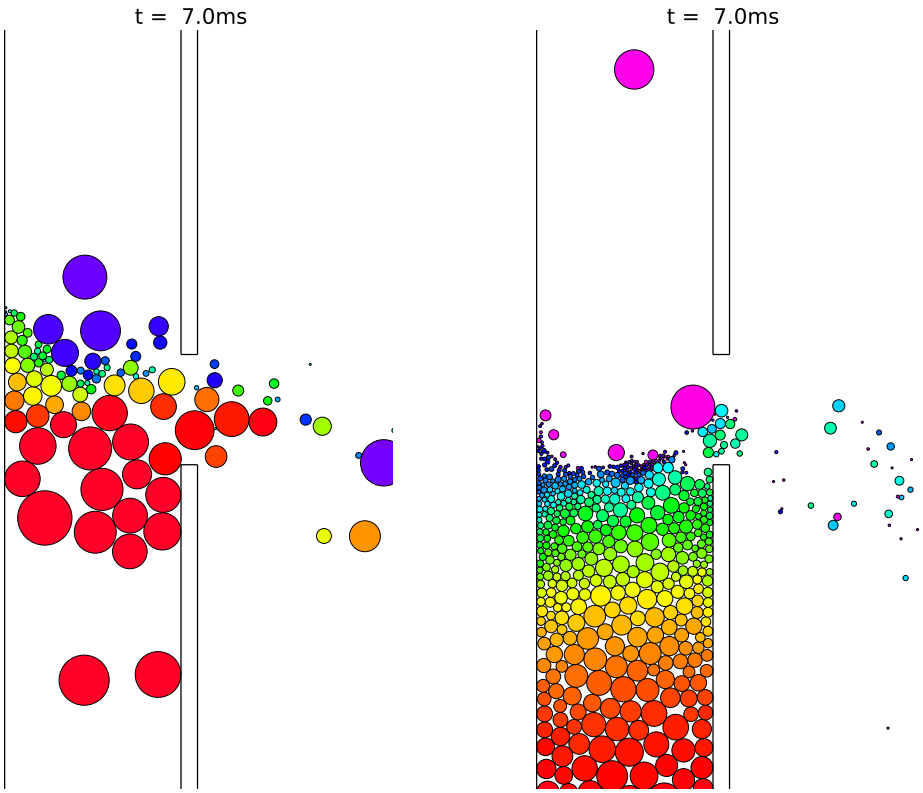

(a) Particles after 7 ms for $\mu_f = 0$. The remaining particles come from the upper and lower parts.

(b) Particles after 7 ms for $\mu_f = 0.5$. The lower part is almost unchanged from t = 0 [ms].

Figure 3.14: Illustration of the favored particles flow from the upper parts with the decreasing pressure model without source term. In the simulation with $\mu_f = 0.5$, the flow going out of the rod comes only from the upper part at first, the lower part being blocked by the effects of gravity and friction.

the cladding is large, and the pressure is therefore already low. The lower part then stays partially inside the cladding.

The fluid pressure barely changes with the friction coefficient (because the pressure gradient is imposed), and the fluid velocity is slightly lower because the drag force between particles and fluid depends on the particle velocity, and the drag slows the fluid. Here, the drag on the particles pushes them outwards, as the particle's velocity is in the same direction as the fluid velocity but with a smaller magnitude (drag accelerates the particles and slows the fluid). Therefore, a lower particle velocity induces a larger drag, reducing fluid velocity even further. This is illustrated in Figure 3.15, which shows the fluid velocity in the crack.

The friction plays an important role in the flow. It slows down both the fluid and the particles, but effects also appear locally. With some models, the flow from the upper part of the column is favored, as the combined effects of gravity, friction, and the weight and velocity of the upper particles stop the particle's flow from the lower part. For the next simulations, a value of $\mu_f = 0.3$ is used. This value is close to the lower bound found for the static friction coefficient of UO2 pellets with the zircalloy of the cladding. However, due to the high influence of the coefficient in the results, better experimental data for the estimation of this coefficient would be useful to validate the model.

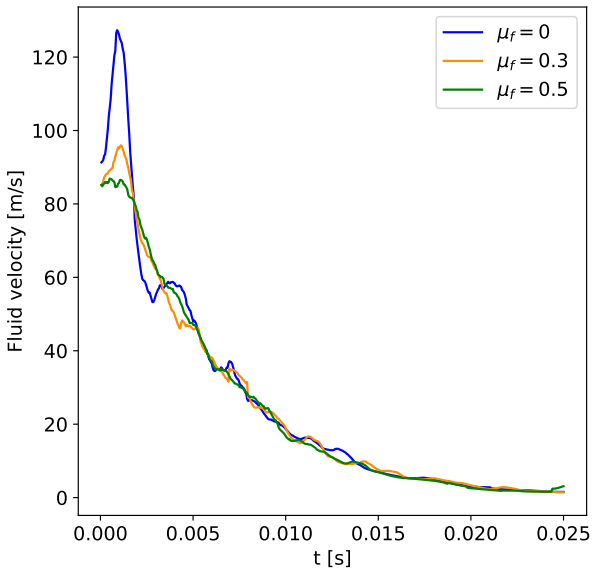

Figure 3.15: Average fluid velocity in the break for various friction coefficients. The velocity is slightly smaller for larger friction coefficients, but the effect is not impactful.

Chapter 4

Study on the impact of various parameters

In this section, the objective is to study quantitatively the impact on the particle flow of various parameters linked to depressurization, such as the pressure gradient, size of the break, properties of the fluid, etc. These parameters are studied in the possible range for the application. Finally, an exploratory work on the possibility of implementing cohesion between particles is presented.

4.1 Initial pressure gradient influence

As seen before, the pressure gradient drives the particles outward, and the initial pressures can vary from 30 to 80 bar inside the cladding and from 1 to 10 bar outside. As the gradient is the factor influencing, only the initial value inside the cladding will be modified here with values of 40, 60, and 80 bars. As the initial pressure value changes, the source term should also decrease because the density and pressure are related (see the model description). The multiplying coefficient is therefore 500 and 750.

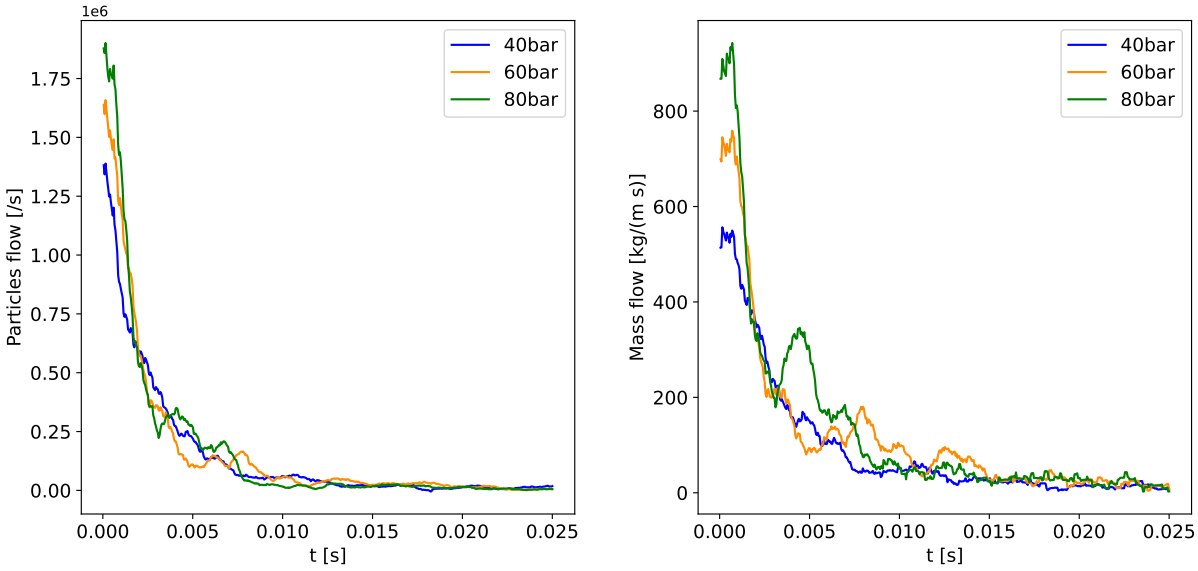

Figure 4.1: Particle and mass flow for varying initial boundary pressure. The flow is slower with a smaller pressure, and the rebounds are of less importance because the source term is also reduced.

The particle and mass flow are plotted in Figure 4.1. The effect of the pressure reduction is seen in 2 ways: first, the flow is slower because the particles are driven by the pressure

gradient. This effect is not linear: the difference between the 80 and 60 bar curves is smaller than between the 60 and 40 bar curves. The other observable difference lies in the global profile of the curves: for lower pressure, the rebounds observed before are smaller (nearly invisible for 40 bar) because the source term is much lower. The ejection time is similar for all cases.

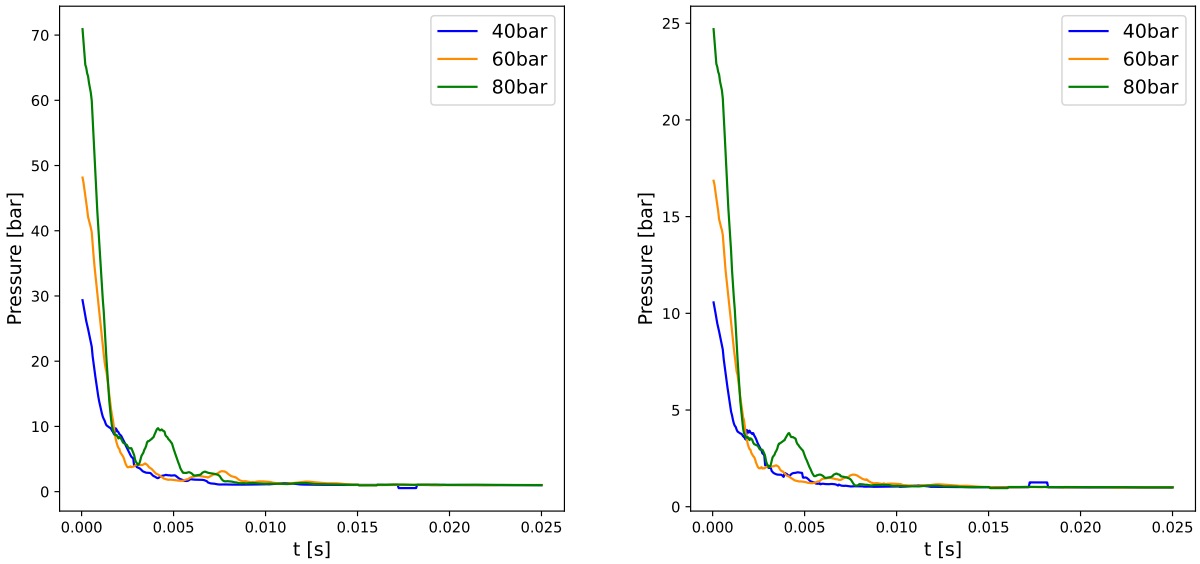

Figure 4.2: Average pressure inside the cladding (left) and inside the break (right) for the different initial pressures imposed. The pressure is lower for a lower initial value but the timescale is similar. The pressure drop between the upper and lower boundaries and the break is larger for larger initial pressure.

The pressure is shown in Figure 4.2. The profiles follow the same tendencies, with higher global pressure for higher initial boundary pressure. The pressure gradient is mainly in the column at the beginning of the three cases, indicating that the particle column generates most of the pressure loss. The fluid velocity is not shown here as it follows the same tendencies as the fluid pressure.

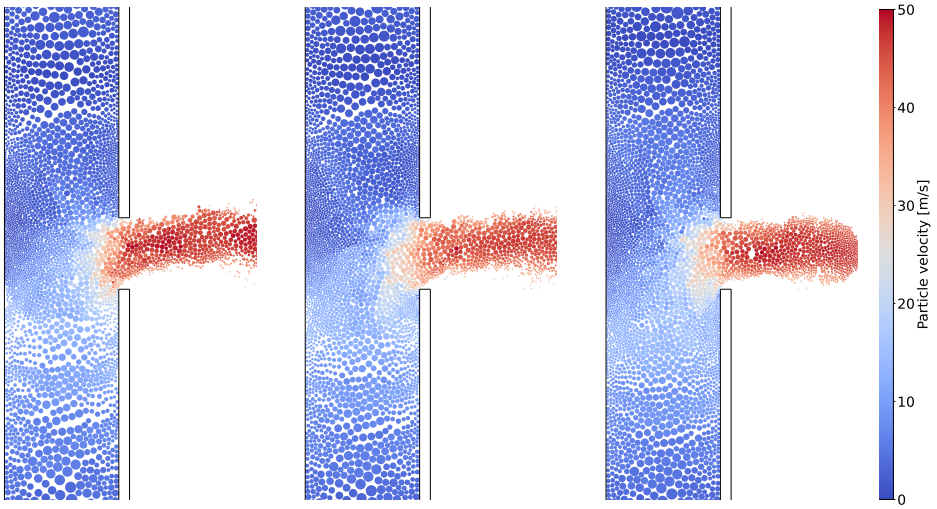

(a) $p_0 = 80$ [bar] (b) $p_0 = 60$ [bar] (c) $p_0 = 40$ [bar]

Figure 4.3: Particle velocity after 0.5 ms with the different initial pressure. The particles are faster for a larger pressure, but this effect is not very visible. The trail formed after the break is smaller for lower pressure because the source term and therefore the fluid velocity are smaller. Inside the cladding, this is shown as the fluid expansion is less visible.

As the mass flow is proportional to the pressure gradient, the particle velocity should be changed accordingly. This is illustrated in Figure 4.3, where the particles have a higher velocity for a larger initial boundary pressure. This change is however nearly invisible between the 40 and 60 bar simulations. Also, the trail outside of the break is smaller (in the 40 bar simulation, the particles on the right are more packed together). As this trail was formed with the introduction of the source term in the models, this size reduction is probably due to the lower source term.

The pressure gradient is shown to be one of the main components in the particle flow magnitude. The particle flow is nearly halved for an initial pressure of 40 bar. The effects of the source term are less visible and almost negligible for the low-pressure gradient. For the particular case of the fuel relocation, this means that lowering the cladding pressure in case of LOCA leading to a break would decrease the amount of radioactive particles emitted in the primary cooling circuit. As this pressurization is done using a spring, the possibility of a system decreasing the imposed pressure when the accident happens could be studied.

4.2 Fluid properties variations: are they significant ?

In the simulations presented before, the fluid properties are taken as constant and set to the initial state: 80 bar and 1200 °C. However, the pressure and temperature of the helium vary, and with that, its properties. The ideal model should include compressible flows, but there is currently no numerical model of compressible granular flow using coupled DEM-CFD. In this part, the influence of the variations will be estimated using multiple simulations taken at different values of pressure and temperature in the range of the physical problem. The maximal temperature is 1200 °C, the temperature inside the cladding, and the minimal temperature is the temperature of the primary cooling circuit, which is around 300 °C. Similarly, the maximal pressure is 80 bar inside the cladding and 1 bar outside.

For the UO2 particles, the density does not vary with pressure, and slightly changes with temperature (from 1089 kg/m^3 for a temperature of 200 °C to 1055 kg/m^3 for a temperature of 1200 °C, which is a change of about 3%), it will be considered constant at 10980 kg/m^3. For the helium, the density and viscosity vary a lot with pressure and temperature. For example, at atmospheric pressure, the density varies between 0.1625 kg/m^3 at 25 °C and 0.03252 kg/m^3 at 1220 °C, while the viscosity takes values from 19.93 10^{-6} Pa.s to 61.55 10^{-6} Pa.s, a large difference. Similarly, at 1200 °C and 80 bar, the density and viscosity are 2.602 kg/m^3 and 6.081 10^{-5} kg m^{-1} s^{-1}. It can be noted that the viscosity only depends on temperature, so comparing two pressures at the same temperature is the same as comparing two densities at the same viscosity. The values that are used here are defined in table 4.1 (Arp & Mccarty 1989). The kinematic viscosity $\nu = \frac{\mu}{\rho}$ is used as the representative number. The source term is modified to take into account the change in density difference between the initial and final state, but in practice, it does not change the graphs.

The particle and mass flow are shown in Figure 4.4. It shows that the simulations using a kinematic viscosity on the order of 10^{-5} have similar results, indicating that the effect of this viscosity is limited when varying little. However, the simulation with a viscosity that is about ten times larger leads to different results: the profile of the mass and particle flow are completely changed, with an initial value nearly halved. The mass flow profile

Pressure	Temperature	Density	Viscosity	Kinematic viscosity
1 [bar]	200 [°C]	0.098 [kg/m^3]	2.836 10^{-5} [kg m^{-1}s^{-1}]	2.908 10^{-4} [m^{2}s^{-1}]
80 [bar]	700 [°C]	3.816 [kg/m^3]	4.624 10^{-5} [kg m^{-1}s^{-1}]	1.212 10^{-5} [m^{2}s^{-1}]
80 [bar]	1200 [°C]	2.602 [kg/m^3]	6.081 10^{-5} [kg m^{-1}s^{-1}]	2.337 10^{-5} [m^{2}s^{-1}]
40 [bar]	1200 [°C]	1.280 [kg/m^3]	6.157 10^{-5} [kg m^{-1}s^{-1}]	4.810 10^{-5} [m^{2}s^{-1}]

Table 4.1: Different sets of properties used for comparison. The representative number is the kinematic viscosity $\nu = \frac{\mu}{\rho}$. The maximal ratio between the kinematic viscosities is about 25. It can be noted that the viscosity only depends on temperature, as seen in the two last lines.

is initially increasing for a few milliseconds and then reduces. However, the total mass expelled remains similar, as the mass flow decreases more gradually.

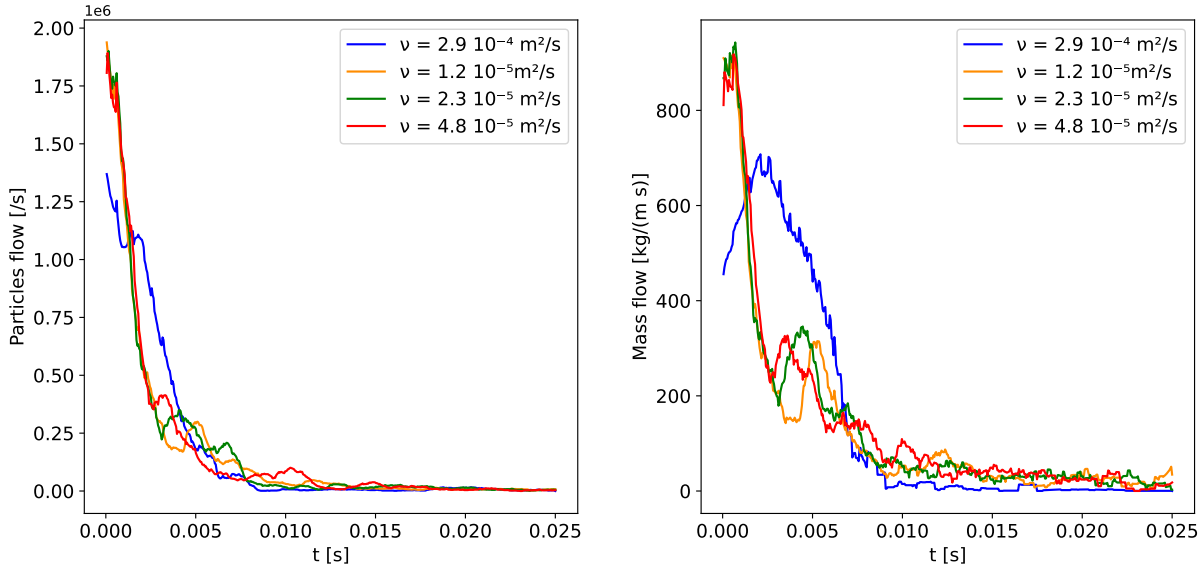

Figure 4.4: Particle and mass flow for multiple kinematic viscosities corresponding to various pressure and temperature doublets. The three values of the order of 10^{-5} are broadly similar, indicating a low influence of the properties change for these values. However, a value that is one order larger leads to very different results, with a smaller mass flow at the beginning but larger after a few milliseconds.

The pressure profile of the fluid follows the same characteristics as the mass flow, as shown in Figure 4.5. The only variation is seen with a larger kinematic viscosity, where the pressure decreases gradually. This is explained by a much lower fluid density. It also explains the particle flow profile: the pressure is larger after a few milliseconds when larger particles go through the break. This means that the heavier particles are expelled faster, leading to a high mass flow. This mass flow then decreases as the pressure drops. The simulation using the largest ν shows the limit of the model: the properties used at 1 bar and 200 °C are not representative in the early stages of the simulation, and it leads to results that are far different from the cases with fluid properties at pressure and temperature closer to the initial problem.

To conclude, this section shows that the properties of the fluid have little impact on the flow as long as the kinematic viscosity is in the same order, about 10^{-5}, which is true in most of the conditions representative of the relocation problem: pressure from 10 to 80 bar and temperature from 500 to 1200 °C. The kinematic viscosity increases with much lower pressure and temperature, leading to a different flow profile. These conditions only appear at the end of the depressurization, when the flow is much slower with a lower pressure gradient, and are therefore less meaningful.

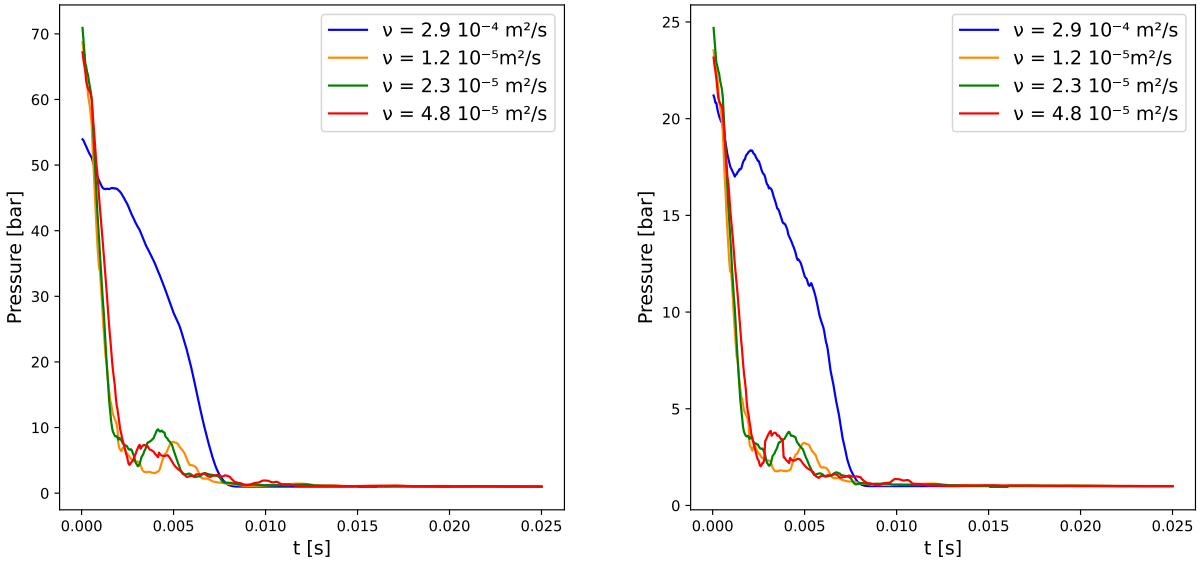

Figure 4.5: Average pressure in the cladding (left) and the break (right) for the different kinematic viscosities. Again, the simulations with a viscosity of the order of 10^{-5} are close together but the larger viscosity in blue is much more different. The pressure is initially lower but drops more slowly.

4.3 How does the break size influence the flow ?

As seen in section 1.1, the size of the break h can vary from 1 to 20 mm, while a value of 5 mm was used until now. Multiple break lengths are now compared: 1, 2.5, 5, and 10 mm. Larger lengths were not considered here, as the interaction between the particles (clogging,...) becomes negligible at these lengths, the only effect of it being a larger mass flow due to the larger length.

One of the first consequences of a smaller breach is the possible clogging of the flow. This clogging appears in three possible cases in the simulations. The first possibility, which is the simplest, is the presence of a grain larger than the breach, blocking it. This blockage is stable, as no pressure difference can unclog it. It is observed for example in the simulation with the decreasing pressure model without friction with a breach size of 1mm, as illustrated in Figure 4.6a. The other possibility of clogging is the formation of a stable arch of particles. This stability is conditional on sufficient friction. This is illustrated in figure 4.6b, with the same simulation as before but with a friction coefficient $\mu_f = 0.3$. This geometry is well-known in granular flows. For example, it appears when emptying silos and is called doing. Finally, the last possibility for the clogging is the same as before, but in this case, the particles inside the cladding are still moving when the blockage appears (because of the source term for example). This movement will destabilize the grains at the blockage and break it. This is illustrated in Figure 4.6c with the simulation using the pressure estimation and a friction coefficient $\mu_f = 0.3$.

In the real case with polyhedral instead of spherical grains, the three blockages are possible. The first with a grain larger than the break would depend on the shape of the grains and the break, and the way the grain moves: for example, a long grain could easily block a large break if the grain crosses perpendicularly. The polyhedral grains could also form arrangements similar to the arch of particles but with more complex shapes and therefore better stability. However, the need to have particles large enough proportionally to the break is always necessary.

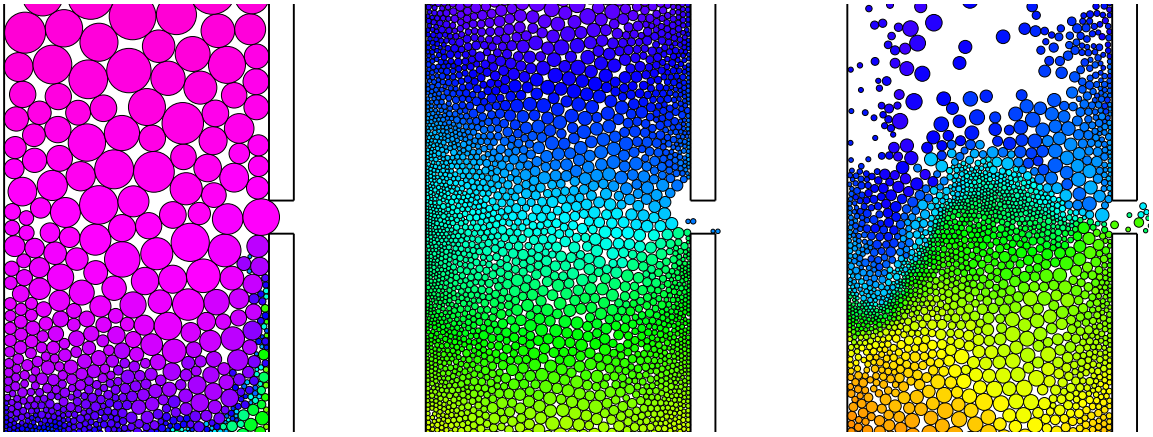

(a) A single grain blocks the flow.

(b) An arch of particles is formed which is stable provided that the friction between the particles is sufficient and that the grains around are not moving.

(c) An arch of particles is formed but is unstable because the particles around are still moving.

Figure 4.6: Comparison of the three possible cloggings.

In terms of particle flow, the size of the breach is one of the main governing parameters. As seen in Figure 4.7, the size will define the characteristics of the flow: the time of ejection, the mass flow, etc. For a size of 1 mm, the particle flow is the smallest, and it clogs at some points. This is not visible in the graph because the blockages are unstable, lasting less than a millisecond, and therefore only slightly visible with the average used (here, the value of the particle flow is smaller around 14 ms). The mass flow at the beginning increases linearly with the size of the breach, but it drops earlier. A lower mass flow is closer to a steady flow, as the emptying takes more time. For rupture larger than a few times the size of the particles, such as $h = 10$ [mm], the interactions of the particles are less visible and the column is less impacting, as the flow of small particles through the large break is closer to a free flow.

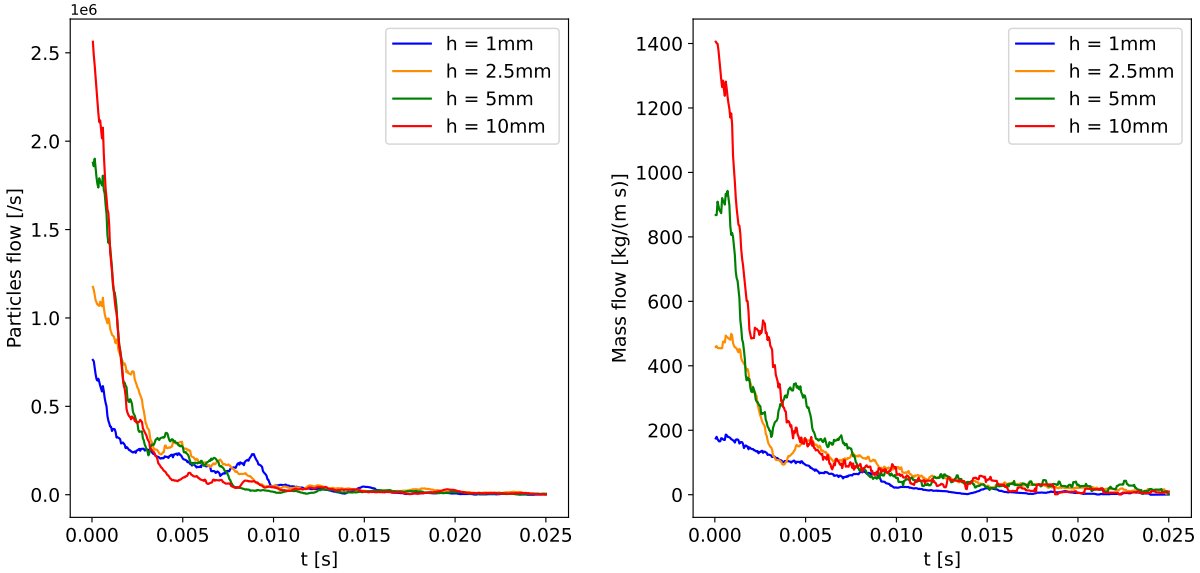

Figure 4.7: Particle and mass flow for different breach sizes. The mass flow is larger for a larger breach. For the breach with a length of 1 mm, the flow is stopped at some times due to unstable arches forming, but it is not seen here as the flow is averaged over time.

The fluid flow is also largely impacted by the size of the breach. In Figure 4.8, the pressure in the cladding and the velocity in the crack are shown. First, the pressure drop

is slower for a smaller break size, which is linked to the pressure estimation model and demonstrates its correctness from a phenomenological point of view (the other models don't consider the break size as the time constant is fixed). A large pressure is observed with the break sizes of 2.5 and 1 mm at the beginning. This is due to the fixed source term. The smaller break does not allow for a sufficient fluid flow and the pressure increases largely inside the cladding (this was already observed when comparing the models, but is exacerbated here). This is not physical but a numerical consequence of the model used for the source term and compressibility representation.

The velocity also decreases but more slowly, because the source term was not modeled through a numerical estimation but with a time constant imposed. The velocity should therefore be lower after 10 ms. It can also be noted that the fluid velocity is non-zero even when the flow is choked. In two dimensions, this is not possible and is linked to the continuous representation of the fluid in CFD-DEM, but it is true in three dimensions: a packing of spheres lets the flow go through it.

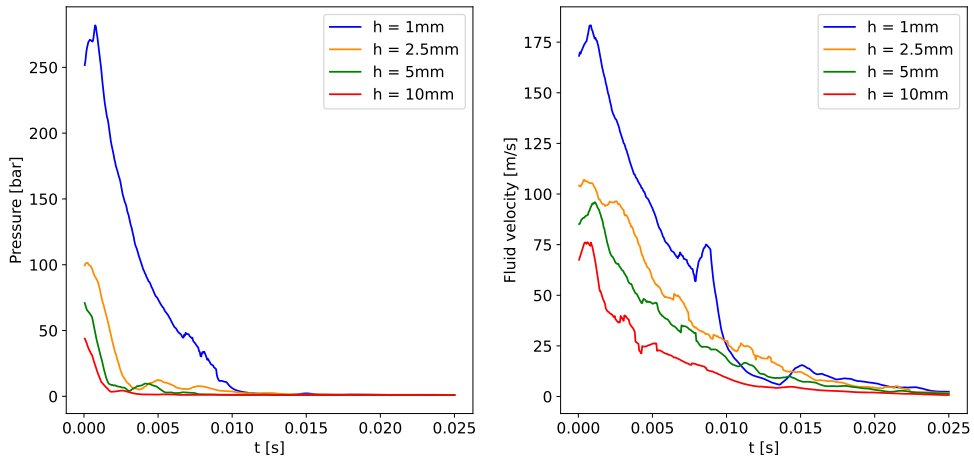

(a) Average pressure inside the cladding.

(b) Average velocity through the break.

Figure 4.8: Fluid characteristics in the crack for different breach sizes. The pressure is much larger for small breaches, which is the numerical effect of the source term and is not physical. The fluid is globally slower for a larger breach size. The variation appearing around 8ms with the 1mm breach is linked to a short-time blockage of the flow. The velocity is non-null even in the case of blockage, which is purely numerical.

The size of the breach has a large impact on both the grains and fluid flows and it is one of the main parameters. A break larger than a few times the size of the grains will lead to a flow where the grain's interactions are less impactful, while the smaller breaks lead to a slower flow, with the interactions between particles having a strong influence with possibilities of stable or unstable blockages.

4.4 Exploratory work: cohesion between particles and cladding

The cohesion force between 2 particles or between the wall and a particle is a normal force that attracts them when they are in contact, opposite to the reaction force of the contact. Cohesion forces between particles or with the cladding play an important role in the relocation of the fuel fragments. It can be understood easily: the particles initially formed a compact block before the fragmentation, and the fragments are still cohesive at the beginning. Furthermore, the complex shape of the fragments in the problem allows for cohesion between them. The cohesion of particles with the wall should lead to the apparition of aggregates around the break, and their size should depend on the cohesion force.

The cohesion force is modeled with 3 parameters: a coefficient α, a time after which the contact becomes cohesive t_c and a maximal tangential velocity that breaks the cohesion w_c. Two different sets of parameters can be used for the cohesion between particles and the cohesion between particles and walls. This gives a cohesion force R_c in [N/m] because the problem is two-dimensional :

$$R_c = \begin{cases} \alpha \text{ [N/m]} & \text{if contact time} > t_c \text{ and } w_t < w_c \\ 0 \text{ [N/m]} & \text{else} \end{cases}$$

From this force, the cohesive impulse $\boldsymbol{p_{ci}}$ on the grain i is computed and then inserted in the contacts solver. A new impulse $\boldsymbol{p}_i^*$ is computed :

$$\boldsymbol{p}_i^* = \boldsymbol{p}_i + \boldsymbol{p_{ci}}$$

Then, the contacts are solved using $\boldsymbol{p}_i^*$ instead of $\boldsymbol{p_{ci}}$. Therefore, the cohesive force appears once the contact is detected (see Section 1.3), which means that this cohesion can be non-zero even if the particles don't touch each other. This behavior is not physical but allows for a simple cohesion model while not interfering much with the results. The parameters are not experimentally determined, which is why this is an exploratory work: the objective is only to show the possible impact of the cohesion in a qualitative way.

At first, the contact duration needed is fixed as $t_c = 0$ [ms] because the grains should be cohesive at the beginning of the simulation. The tangential velocity is at first set to $w_t = 1000$ [m/s], a value much larger than the velocity of the grains such that the cohesion won't break because of this condition. For the coefficient α, the value is harder to choose. Here, the objective is to show the effect of the cohesion and the value should then be large enough. To do so, the coefficient will be expressed from the weight of the largest grain :

$$\alpha = A\rho_p \pi r_{\text{largest}}^2 g = 0.593A \text{ [N/m]}$$

With r_{largest} the radius of the largest particle and g the gravity acceleration. From this, multiple values of A are expressed. To see the effects of cohesion, the condition $A > 1$ has to be respected because the fluid force on the grains is much larger than their weight.

The first simulations shown here used multiple values of A (see Table 4.2). Large values are used to show the impact of the coefficient clearly. The cohesion is only activated with the wall, there is no cohesion between the grains. The objective here is to show the formation of aggregates around the breach and in the cladding, as shown in Figures 4.9 and 4.10. The time at which they form and their size depend on the cohesion coefficient: small values such as $A = 1$ and $A = 5$ lead to smaller deposits that form later when the

pressure gradient is lower. For large values of A, the size of the deposits is constant as the cohesion force is much larger than the forces of the fluid on the grains. Therefore, a grain is stopped by the cohesion force as soon as it detects a contact with the wall. The size of the aggregate is defined by the contact detection distance for these large values which is purely numerical.

A	α
1	0.593 [N/m]
5	2.965 [N/m]
10	5.93 [N/m]
25	14.825 [N/m]
50	29.65 [N/m]

Table 4.2: Corresponding values of A and α for the simulation with cohesion with the wall.

These aggregates correspond to the physics: in the cladding, some polyhedral grains are bonded to the cladding surface and don't move, like a dust deposit or the sediments deposited at the bottom of a river. A phenomenon of crackling appears at early times with large coefficients. This is a sign that the model is interesting and can be used for better approximation of the flow: in the actual dispersal, the polyhedral fragments should break apart similarly to this. This also leads to a different fragment flow: the fragments separate inside the cladding, while they are coming out in a single continuous stream without cohesion. This is also closer to the physical model of polyhedral fragments.

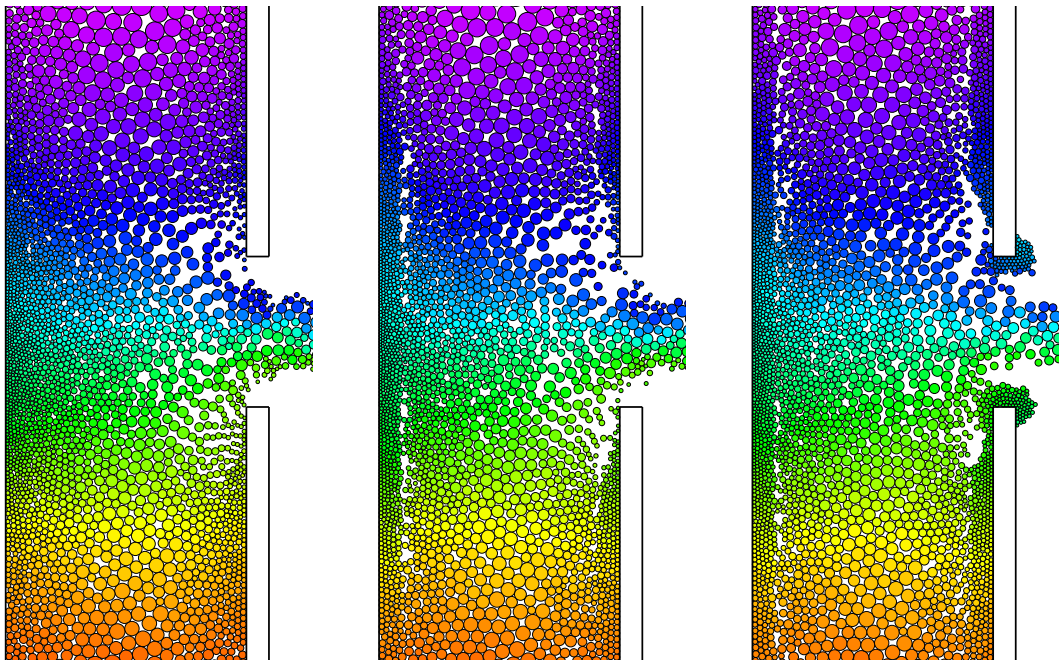

(a) $A = 1$ (b) $A = 10$ (c) $A = 50$

Figure 4.9: Comparison of the aggregate sizes around the break and on the surface of the cladding after 1 ms. With $A = 1$, the effects are almost unnoticeable, but the cases with $A = 10$ and 50 show a crackling of the assembly, which is closer to the behavior of polyhedral cohesive fragments. The fragments bonded to the inside wall of the cladding are visible in both, but the deposit formation around the breach only begins in the case with $A = 50$.

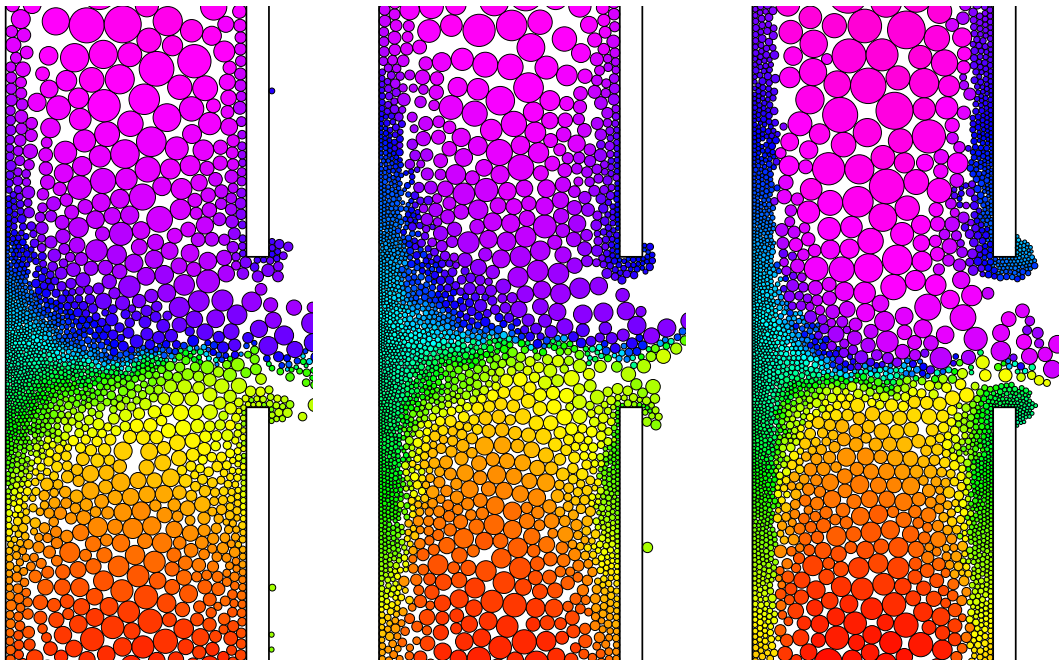

(a) $A = 1$ (b) $A = 10$ (c) $A = 50$

Figure 4.10: Comparison of the aggregate sizes around the break and on the surface of the cladding after 10 ms. The deposits on the inner surface of the cladding and around the breach are formed and stabilized. The deposit is much larger and denser for larger coefficients.

In terms of particle and mass flow, the effect of the cohesion with the wall is clear: it slows the flow because, like friction, it binds the particles together. This effect is clear between the simulations with $A = 0$ and $A = 1$, however it reduces after. The difference between $A = 5$ and $A = 25$ is smaller. The case with $A = 50$ is more extreme: the cohesion force is so large that the particles nearly can't escape the cladding. This results in a much slower flow with most of the particles staying inside the cladding after the 25 ms. The profile is closer to a linear profile, because the main driver of the flow, pressure, is less important than the cohesion force. The fluid flow is not illustrated as it is not modified so much by cohesion, and it is of less interest in the context of this exploratory work.

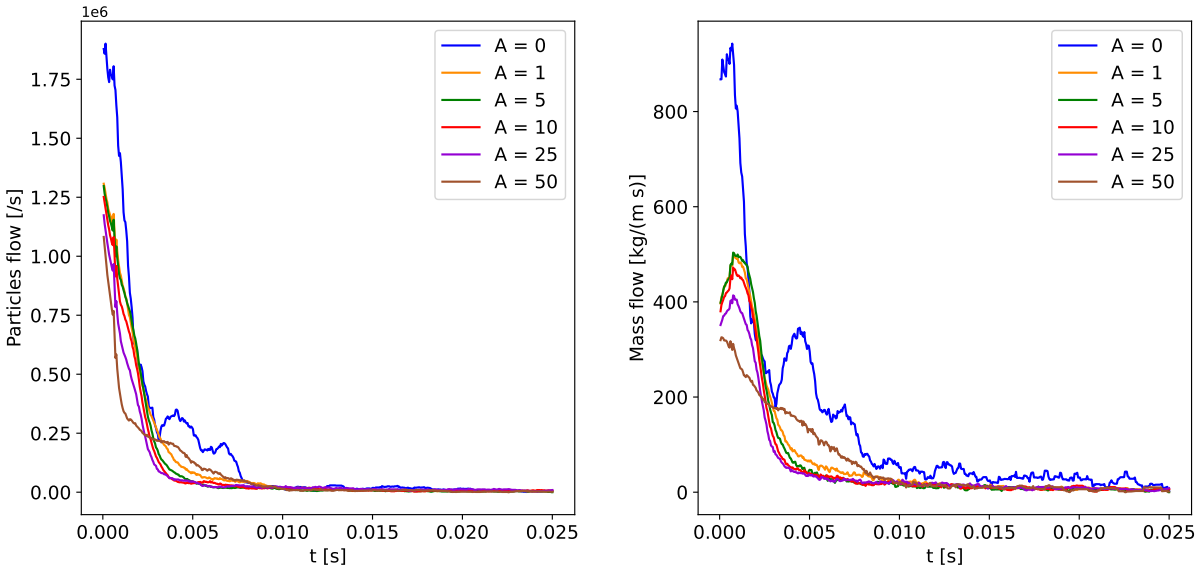

Figure 4.11: Particle and mass flow for different values of A. The flow is much slower for a non-zero cohesion coefficient, but the effect for very large values of A becomes less visible. The case with $A = 50$ shows a nearly linear profile because the pressure gradient pushing the particles is proportionally reduced.

The particle velocity is not changed much: in Figure 4.12, the grains are drawn according to their velocity after 0.5 ms which is the time at which they are the fastest. Between $A = 1$ and $A = 50$, the difference is significant, and the velocity is lower than for the case without cohesion (see Figure 4.3). The difference in mass flow is explained by the lower frequency at which the grains detach from the main mass.

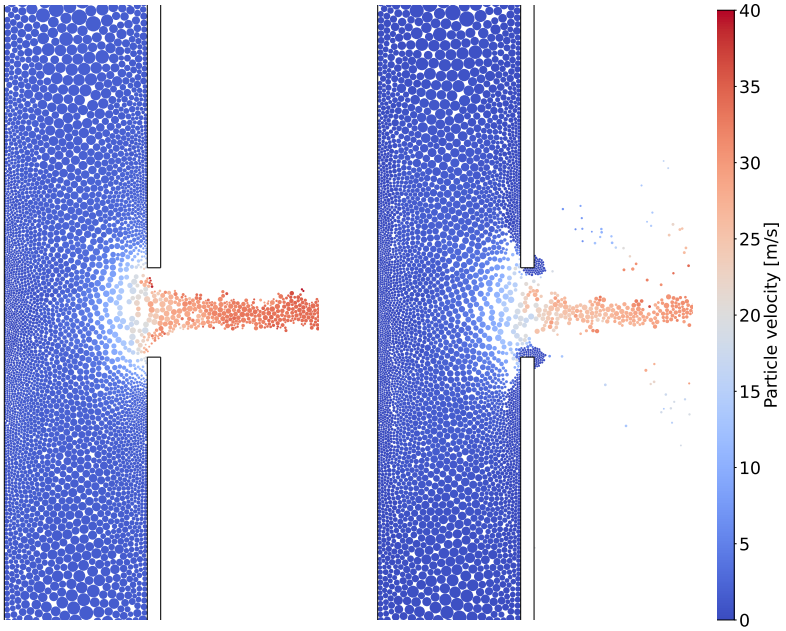

(a) $A = 1$ (b) $A = 50$

Figure 4.12: Particle velocity comparison different cohesion coefficients with the wall. The velocity is smaller with a large cohesion coefficient, and the stream of grains in the break is tighter. The combination of these two things explains the reduced mass flow.

Next, cohesion is only used between the particles and not with the cladding. In this case, the coefficient A has to be much smaller: as the particles have a lot of possible contacts together, the sum of these cohesive contacts is much larger. Here, the values chosen for A are ten times smaller than for the cohesion with the wall (see Table 4.3). The effect on the particle and mass flow is illustrated in Figure 4.13. A non-zero coefficient reduces greatly the mass flow. While the initial mass flow does not change much between $A = 0.1$ and $A = 2.5$, the difference is that the flow is stopped with larger A at some point while it keeps going with the value $A = 0.1$. It can be seen that a value ten times smaller for the coefficient leads to a similar effect on the initial mass flow than with the wall cohesion.

A	α
0.1	0.0593 [N/m]
0.5	0.2965 [N/m]
1	0.593 [N/m]
2.5	1.4825 [N/m]
5	2.965 [N/m]

Table 4.3: Corresponding values of A and α for the simulation with cohesion between the particles.

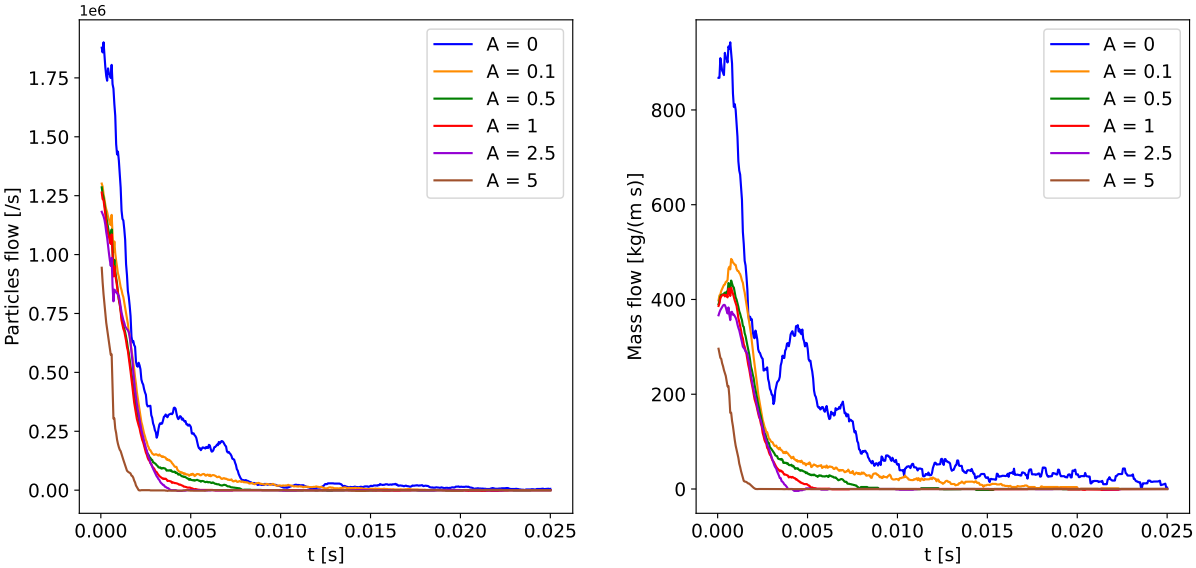

Figure 4.13: Particle and mass flow for different values of A. The flow is much slower for non-zero cohesion coefficients. The cases with $A \geq 0.5$ even lead to the flow stopping, and this flow stops earlier for a larger coefficient.

In Figure 4.14, the various behaviors of the grains are illustrated after 12 ms. With small values of A, the flow is less disturbed, and the particles on the left are attracted to the right because of their bonding with the particles flowing in the cladding and the break. For $A = 1$, the grains are flowing but their interactions disturb the relocation around the rupture, leading to a lower mass flow. The large values lead to a flow that stops after a few milliseconds because of the strong interactions between the particles. In terms of grain velocity, the cohesion reduces a bit the velocity in the rupture but not much because the cohesion with the main grain mass in the cladding is deactivated. The change in mass flow comes from the fact that as the grains are more cohesive, they detach less often from the main mass.

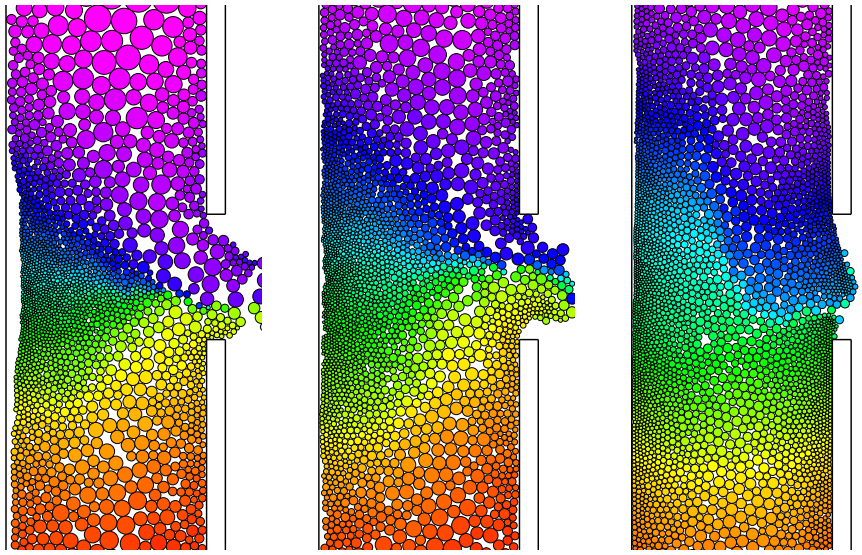

(a) $A = 0.1$ (b) $A = 1$ (c) $A = 5$

Figure 4.14: Comparison of the particle cohesion after 12 ms with multiple cohesion coefficients. With $A = 0.1$, the flow is slowed and the particles on the left are attracted to the right due to their bonding. With $A = 1$, the grains are bonded together in the break, which does not stop the flow but slows it down considerably. Finally, with $A = 5$, the flow is completely stopped as the grains are stable.

In these last three simulations, the cohesion is activated for both the particles and the wall. Three sets of cohesion forces are chosen and detailed in Table 4.4. The values are small such that the flow is not blocked but only slowed.

Simulation ID	Cohesion force with particles	Cohesion force with walls
0	0 [N/m]	0 [N/m]
1	0.0593 [N/m]	1.186 [N/m]
2	0.02965 [N/m]	2.965 [N/m]
3	0.014825 [N/m]	0.2965 [N/m]

Table 4.4: Cohesion forces used in the simulations with cohesion between particles and with the walls.

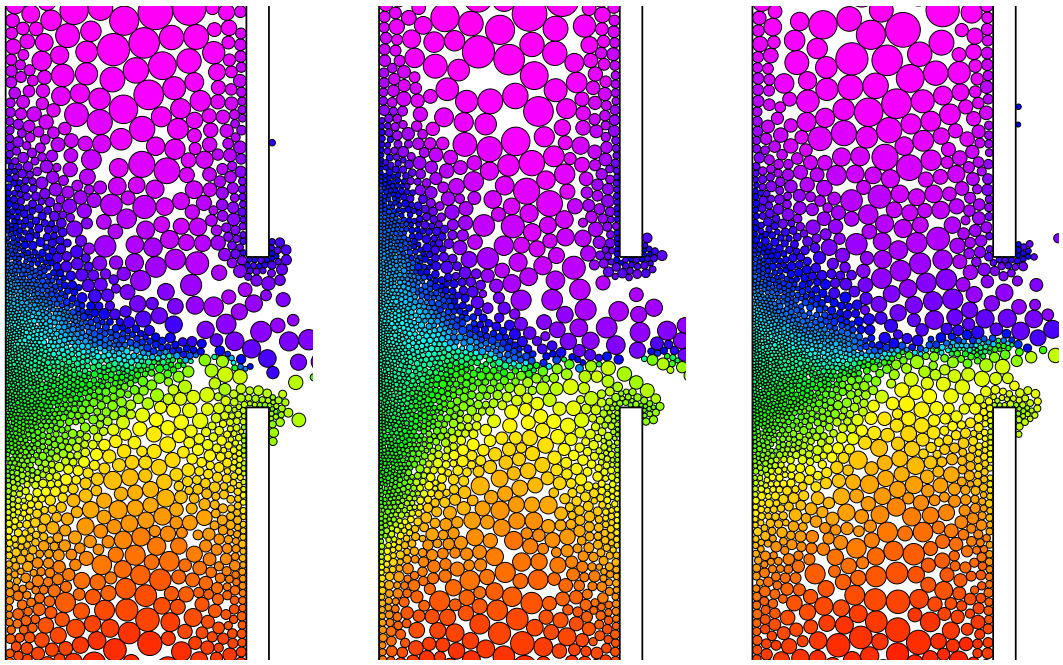

(a) ID = 1 (b) ID = 2 (c) ID = 3

Figure 4.15: Comparison of the particles inside the cladding after 10 ms for the three different cohesion parametrizations.

For all three simulations, the agglomerates around the breach and the deposits on the inner surface of the cladding appear. Their sizes and shapes are slightly different (see Figure 4.15) but globally the same. In the last simulation, the particles are closer and the flow is more continuous because the cohesion coefficients are smaller. The deposits on the inner surface of the cladding and around the breach are larger for simulations 1 and 2. The displacement of the particles is the same for the three models, as seen by the colors of the particles.

The mass flow is close for the three models as shown in Figure 4.16, the last one having a slightly larger mass flow because of the lower coefficients. It shows that the exact values of the cohesion with walls and with particles are not needed for a good modeling of the relocation, only orders of magnitude are already a good approximation. The velocity of the magnitude is the same for all three models at about 20 m/s.

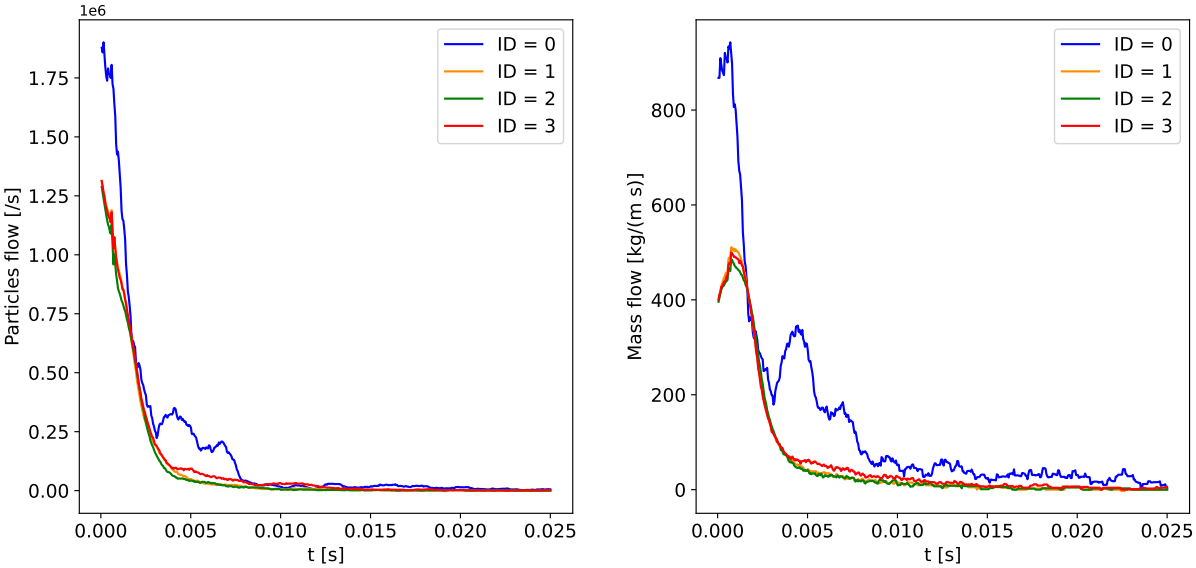

Figure 4.16: Comparison of the mass flows with the three models including cohesion with particles and walls. They are closely the same for the three models with cohesion. The last model has a slightly larger mass flow because of the lower cohesion forces.

In summary, the cohesion between the particles and the cladding significantly affects the flow through the rupture. The numerical values used here are not based on experimental or analytical data, as such data were not available. Nevertheless, the phenomenological effects are visible such as the gathering of particles around the breach and on the cladding surface. The cohesion between particles also allows for the slowing of the flow, more resembling the flow of polyhedral grains. The model could be further improved by using a more complex cohesion law, for instance, one with a spatial and time dependency of the coefficient to represent the cohesion and with a numerical model that only considers the grains actually touching each other.

Conclusion

In this work, the problem of fuel relocation and dispersal during the depressurization of a nuclear fuel rod is addressed. The goal is to develop the needed models for the basic quantitative and qualitative study of this dispersal. In the first chapter, a review of existing knowledge of this problem, in terms of pellet fragmentation and experimental and numerical modelling is conducted. Then, the treatment of this relocation as a granular flow problem is explained, and the software used for the simulations, Migflow, is presented with the numerical methods used such as DEM, Non-Smooth Contact Dynamics, and semi-resolved methods for CFD. Finally, the objectives of this work are defined.

In the second chapter, an algorithm for generating 2D particles is presented. This algorithm builds upon existing methods for creating particle deposits but introduces new features for controlling the spatial distribution of grains based on their size. It also includes a model for enhancing the compactness of the generated deposit and then stabilizing it. The text then provides several examples of potential generations to demonstrate its functionality. Finally, the algorithm is employed to produce a column of particles that align with the experimental data obtained from the literature review.

In the third part of this master's thesis, the simulation of relocation is developed. The numerical, physical, and geometrical parameters are presented, followed by the modeling of various physical phenomena such as pressure gradient and friction, along with their impact on the flow. Different methods for estimating the pressure gradient are discussed, each with its own physical significance. However, none were completely convincing, partly due to the approximate modeling of gas compressibility in the cladding and the lack of experimental data. The friction coefficient was also observed to affect particle and fluid flow significantly, slowing it down and causing local effects such as a preferred flow direction from the upper part of the cladding, leading to a rebound phenomenon in fluid and particle velocities and mass flows. Given the considerable impact of friction, a better experimental model for the friction coefficient would be beneficial for quantitative studies.

The fourth chapter presents a study on the factors affecting flow using previously proposed models. It was found that the initial pressure inside the cladding is a key factor in determining grain flow through the breach. The study also examined how variations in fluid properties due to changes in pressure and temperature impact the flow. It was observed that these variations have limited effects within most pressure and temperature ranges for this case. Additionally, different breach sizes were compared, and it was noted that clogging occurs when the breach length is close to the diameter of the particles. The study also introduced an exploratory model for the cohesion of particles with each other and with the cladding. Although this model was not based on experimental or numerical data, it showed promise in representing interactions during depressurization. The cohesion with the wall led to the formation of small particle agglomerates, particularly around the fracture zone, which is expected during rod depressurization. The cohesion between the grains also provides a better representation of the physics of the fragments. The

approximation of the polyhedron using 2D spheres reduces the interaction forces between the grains, and a well-fitted cohesion model can balance this effect.

Finally, the results presented here must be put into perspective. It shows the physics of the depressurization of the rod in a new way, including a better model for the particle flows, and effects that were not taken into account before or detailed as much (friction, fluid properties, etc.). It also proves the efficiency and accuracy of the coupled CFD-DEM method to study the fuel dispersal problem. Especially, the distribution of particle size in the column is now controllable and much closer to the experimental results. However, little experimental data exists to confirm or deny the results shown here on the particle's mass flow, pressure evolution, etc. The data from simulations presented in the second chapter, while showing a similar trend, are not sufficient to validate the model, and indicate a longer time scale which is due to the small part of the rod that is simulated, the low interaction forces between the spherical grains, etc.

This work suggests possible improvements for the depressurization model. The main directions identified are explained below. First, some parameters could be easily enhanced, but the simulations would be more computationally expensive. Adapting the model to three dimensions would improve the accuracy of the results. This is because dense packing in two and three dimensions, the shape of the hole, and the overall characteristics of granular flows are different. Generalizing the particle-generating algorithm to work in three dimensions is necessary, as it currently only functions in two dimensions. A more complex shape of the grains is needed for a precise model to represent the interactions between the fluid, grains, and cladding. However, Migflow does not implement the models required for these complex shapes, and there is no experimental data to estimate the shapes of the grains. Following these more complex shapes, the entire cladding can be simulated with greater precision.

There are potential improvements associated with experimental data and better modeling. Firstly, the cohesion between the grains and the cladding should be investigated to obtain numerical or experimental data. Another potential improvement is the use of a granular flow model that incorporates the compressibility of the fluid, although there are currently no numerical models for this, and the behavior of these flows is more complex. This also involves managing the temperature of the particles and flows. A two-phase model could be beneficial for distinguishing the helium inside the column from the water or steam outside.

Appendices

A Possible improvements to the particle generation algorithm

The compactness of the generated deposit could be increased further. To do so, the objective is to add particles between the existing particles. From an already generated deposit, one can find the largest circle possible without overlapping with existing circles. From this, a particle located at this circle center and with the circle's radius can be inserted. This is done recursively until the inserted particle is smaller than a defined radius r_{min}. The algorithm is illustrated in Figure 17. This is a geometry problem with no simple solution. The algorithm was thus not implemented, as it had major issues: high complexity and computational cost, bad adaptation to the control of particle spatial distribution, and it was not useful for the desired physical application.

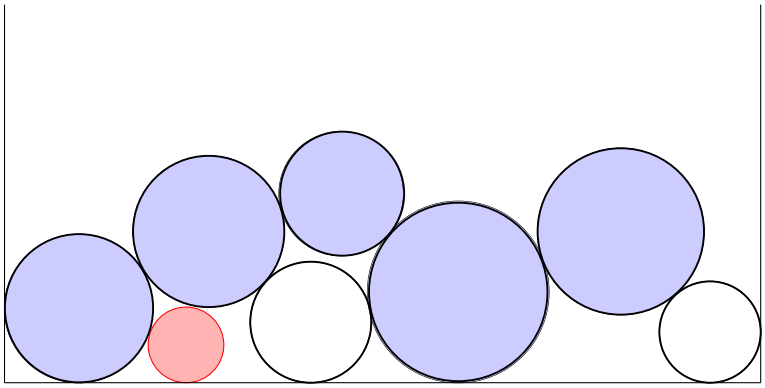

Figure 17: Illustration of the insertion of smaller particles in existing deposit. Red particle is inserted as long as $r > r_{\min}$.

The algorithm can be generalized in 3D. The most difficult part is the original potential-based algorithm, as the computation of the front of particles and possible points of insertion is more complex. However, the adaptation proposed after that is usable in 3D: the estimation of the height to generate theoretical radii and the local polydispersity. Then, the score function only needs to take into account the 3 dimensions instead of 2, meaning that it is possible to choose the spatial distribution across the width and the length of the box.

B Definition of the boundary conditions

With an open boundary condition, the fluid pressure is imposed as p^*. The gradient of this pressure is perpendicular to the boundary. Furthermore, the gradient of fluid velocity in the normal direction is zero. This is written as:‘

$$p = p^* \qquad \nabla p \cdot \boldsymbol{n} = 0$$
$$\nabla_n \boldsymbol{u} = 0 \qquad \nabla \boldsymbol{u}_n = 0$$

A wall boundary condition means that the flow can’t go through the boundary. The other conditions are the same as for open boundaries, but there is no imposed pressure :

$$\boldsymbol{u} \cdot \boldsymbol{n} = 0 \qquad \nabla p \cdot \boldsymbol{n} = 0$$
$$\nabla_n \boldsymbol{u} = 0 \qquad \nabla \boldsymbol{u}_n = 0$$

Bibliography

Arp, V. & Mccarty, R. (1989), 'Thermophysical properties of helium-4 from 0.8 to 1500 k with pressures to 2000 mpa'.

Bianco, A., Vitanza, C., Seidl, M., Wensauer, A., Faber, W. & Macián-Juan, R. (2015), 'Experimental investigation on the causes for pellet fragmentation under loca conditions', *Journal of Nuclear Materials* **465**, 260–267.

Blair, P. (2008), 'Modelling of fission gas behaviour in high burnup nuclear fuel'.

Bonnet, J. (2021), Modélisation des mécanismes de fragmentation du combustible UO2 en situation de Perte de Réfrigérant Primaire (APRP), PhD thesis.

Bozhko, Y., Bolobolichev, A., Kostochka, A. & Shchavelin, V. (1991), 'Coefficient of static friction of the uranium dioxide-zirconium alloy pair under irradiation', *Soviet Atomic Energy* **71**.

Brankov, V. V. (2017), 'Modelling of fuel fragmentation, relocation and dispersal during loss-of-coolant accident in light water reactor', p. 176.

Capps, N., Jensen, C., Cappia, F., Harp, J., Terrani, K., Woolstenhulme, N. & Wachs, D. (2021), 'A critical review of high burnup fuel fragmentation, relocation, and dispersal under loss-of-coolant accident conditions', *Journal of Nuclear Materials* **546**.

Capps, N. & Sweet, R. (2023), 'Model for determining rupture area in zircaloy cladding under loca conditions', *Nuclear Engineering and Design* **401**.

Capps, N., Yan, Y., Raftery, A., Burns, Z., Smith, T., Terrani, K., Yueh, K., Bales, M., & Linton, K. (2020), 'Integral loca fragmentation test on high-burnup fuel', *Nuclear Engineering and Design* **367**.

Carbajo, J. J. (2001), 'Thermophysical properties of mox and uo2 fuels including the effects of irradiation'.

COLLIER, J. G. & DAVIES, L. M. (1980), 'The accident at three mile island', *Heat Transfer Engineering* **1**(3), 56–67.

Constant, M., Dubois, F., Lambrechts, J. & Legat, V. (2018), 'Implementation of an unresolved stabilised FEM–DEM model to solve immersed granular flows', *Computational Particle Mechanics* .

D'Auria, F. (2017), *Thermal-Hydraulics of Water Cooled Nuclear Reactors*.

El-Sefy, M., Ezzeldin, M., El-Dakhakhni, W., Wiebe, L. & Nagasaki, S. (2019), 'System dynamics simulation of the thermal dynamic processes in nuclear power plants', *Nuclear Engineering and Technology* **51**.

FEBEG (2023), 'Statistiques électricité', `https://www.febeg.be/fr/statistiques-electricite`. Accessed: 02/04/2024.

Forgeron, T., Brachet, J.-C., Barcelo, F., Castaing, A., Hivroz, J., Mardon, J. & Bernaudat, C. (2000), 'Experiment and modeling of advanced fuel rod cladding behavior under loca conditions: Alpha-beta phase transformation kinetics and edgar methodology', *ASTM Special Technical Publication* pp. 256–278.

Govers, K. & Verwerft, M. (2016), 'Discrete element method study of fuel relocation and dispersal during loss-of-coolant accidents', *Journal of Nuclear Materials* **478**, 322–332.

Hanus, E., Malgouyres, P., Clement, S., Alloncle, R., Pontillon, M., Bernard, S., Gleizes, B., Masson, R., Pontillon, Y. & Noirot, J. (2016), MEXIICO a new equipment to study the pressure impact on the irradiated fuel behavior, *in* 'Top Fuel Meeting 2016'.

Hussain, A. & Nawaz, A. (2016), 'The investigation of nonavailability of passive safety systems effects on small break loca sequence in ap1000 using relap5 mod 4.0', *Science and Technology of Nuclear Installations* **2016**, 1–11.

J. A. Turnbull, S. K. Yagnik, M. H. D. M. S. & Walker, C. T. (2015), 'An assessment of the fuel pulverization threshold during loca-type temperature transients', *Nuclear Science and Engineering* **179**(4), 477–485.

Jean, M. (1999), 'The non-smooth contact dynamics method', *Computer Methods in Applied Mechanics and Engineering* **177**(3), 235–257.

Karlsson, J., Magnusson, P., Tejland, P., Puranen, A., König, M., Beccau, P. & Grandi, G. (2017), The studsvik cladding integrity project (scip) iii - overview, 12 International conference on WWER fuel performance, modelling and experimental support.

Khvostov, G., Wiesenack, W., Zimmermann, M. & Ledergerber, G. (2011), 'Some insights into the role of axial gas flow in fuel rod behaviour during the loca based on halden tests and calculations with the falcon-psi code', *Nuclear Engineering and Design - NUCL ENG DES* **241**, 1500–1507.

Kim, J., Yoon, J. W., Kim, H. & Lee, S.-U. (2021), 'Prediction of ballooning and burst for nuclear fuel cladding with anisotropic creep modeling during loss of coolant accident (loca)', *Nuclear Engineering and Technology* **53**(10), 3379–3397.

Lindholm, I. (2002), 'A review of dryout heat fluxes and coolability of particle beds'.

M. Flanagan, P. A. (2012), 'Observations of fuel fragmentation, mobility and release in integral, high-burnup, fueled loca tests'.

Man, T., Zhang, P., Ge, Z., Galindo Torres, S. A. & Hill, K. (2022), 'Friction-dependent rheology of dry granular systems'.

Montgomery, R. & Bevard, B. B. (2020), 'Sister rod destructive examinations (fy20)'.

Moreau, J. J. (1994), 'Some numerical methods in multibody dynamics: application to granular materials', *European journal of mechanics-A/Solids* pp. 13:93–114.

NEA (2010), 'Safety significance of the halden ifa-650 loca test results', *OECD Publishing, Paris* .

Polanía, O., Cabrera, M., Renouf, M. & Azéma, E. (2022), 'Collapse of dry and immersed polydisperse granular columns: A unified runout description', *Physical Review Fluids* **7**(8), 084304.

Qi, Z., Kuang, S., Rong, L., Dong, K. & Yu, A. (2022), General drag correlations for particle-fluid system, *in* V. R. Prasad, V. Silva & J. Cardoso, eds, 'Boundary Layer Flows', IntechOpen, Rijeka, chapter 4.

Radjai, F. & Richefeu, V. (2009), 'Contact dynamics as a nonsmooth discrete element method', *Mechanics of Materials* **41**(6), 715–728. Advances in the Dynamics of Granular Materials.

Raynaud, P. (2012), 'Fuel fragmentation, relocation, and dispersal during the loss-of-coolant accident'.

Raynaud, P. & Porter, I. (2014), Predictions of fuel dispersal during a loca.

Rui Li, G. D. & Sakai, M. (2024), 'Dem simulations in nuclear engineering: a review of recent progress', *Journal of Nuclear Science and Technology* **61**(3), 285–306.

Rycroft, C. H., Grest, G. S., Landry, J. W. & Bazant, M. Z. (2006), 'Analysis of granular flow in a pebble-bed nuclear reactor', *Phys. Rev. E* **74**, 021306.

Scott, G. D. (1960), 'Packing of spheres: Packing of equal spheres', *Nature* **188**, 908–909.

Shchavelin, V., Kostochka, A., Kuznetsov, A., Golovnin, I. & Bibilashvili, Y. (1986), 'In-reactor study of the friction characteristics of reactor materials', *Atomic Energy - AT ENERGY-ENGL TR* **61**, 686–690.

Taboada, A., Chang, K.-J., Radjai, F. & Bouchette, F. (2005), 'Rheology, force transmission, and shear instabilities in frictional granular media from biaxial numerical tests using the contact dynamics method', *Journal of Geophysical Research : Solid Earth* **110**(B9), B09202.

Trégourès, N. (2013), 'L'accident par perte de réfrigérant primaire : phénoménologie, critères de sûreté, simulation', *Revue Générale Nucléaire* **6**, pages 67–74.

Voivret, C., Radjaï, F., Delenne, J.-Y. & El Youssoufi, M. S. (2007), 'Space-filling properties of polydisperse granular media', *Phys. Rev. E* **76**, 021301.

Wiesenack, W., Karlsson, J., Noirot, J. & Sonnenburg, H. (2016), 'Report on fuel fragmentation, relocation and dispersal - chapter 2'.

Zhong, W., Yu, A., Liu, X., Tong, Z. & Zhang, H. (2016), 'Dem/cfd-dem modelling of non-spherical particulate systems: Theoretical developments and applications', *Powder Technology* **302**, 108–152.

UNIVERSITÉ CATHOLIQUE DE LOUVAIN
École polytechnique de Louvain
Rue Archimède, 1 bte L6.11.01, 1348 Louvain-la-Neuve, Belgique | **www.uclouvain.be/epl**